

DESIGN AND FINITE ELEMENT MODELING OF A HIGH ENERGY  
DENSITY STRAIN ENERGY ACCUMULATOR

By

Alexander Vadimovich Pedchenko

Thesis

Submitted to the Faculty of the  
Graduate School of Vanderbilt University  
in partial fulfillment of the requirements  
for the degree of

MASTER OF SCIENCE

in

Mechanical Engineering

May, 2014

Nashville, Tennessee

Approved:

Date:

Eric J. Barth \_\_\_\_\_

\_\_\_\_\_

Michael Goldfarb \_\_\_\_\_

\_\_\_\_\_

Thomas J. Withrow \_\_\_\_\_

\_\_\_\_\_

To my parents and grandparents,  
who have always provided invaluable guidance, support and love

## ACKNOWLEDGEMENTS

The work presented in this manuscript is funded by the Center for Compact and Efficient Fluid Power. The author would like to extend his thanks not only to the Center, but to its dedicated members who provided direct assistance on the project. Specifically, the author would like to thank Lance Miller, Joel Edwards and Brian Orapello of Gates Corporation for graciously providing consulting, as well as material data and samples. The author would also like to express his gratitude for the technical assistance and financial aid involved in patent submission provided by Simon Baseley and the Bosch Rexroth Corporation; he hopes that future project development will involve further collaboration. Michael Volovets and Larry Fern of the Parker Hannifin Corporation's Oildyne Division were kind enough to provide a miniature axial piston pump used for testing the polyurethane cord prototype.

In addition to the Center's members, a number of Vanderbilt University students, employees and faculty have put in a considerable amount of their time and effort into helping the author obtain the results documented within this work. The author would like to extend his thanks to the members of the undergraduate senior design team - Abdullah Abidin, Karl Brandt, Danielle Patellis, Hafizah Sinin and Oliver Tan. During their short time at Vanderbilt, Ricardo Reina, Stephanie Carusillo, Eric Bowen and George Mast provided a great amount of assistance on both of the low-pressure prototypes. The author would like to thank two of his colleagues, Chao Yong, for providing his expertise on state-flow implementation in Simulink, and Mark Hofacker, for aid in the early stages of instrumentation. Professor Armutur Anilkumar's knowledge of dimensionless analysis

was greatly appreciated in attempting to employ nondimensionalization before switching to using Abaqus. The author's gratitude is also extended to Dr. Thomas Withrow and Dr. Michael Goldfarb for agreeing to serve on his thesis committee and providing invaluable feedback and support. Lastly, the author would like to extend utmost gratitude to his advisor, Dr. Eric Barth. Without his knowledge, guidance, and encouragement, the work presented herein would not have been possible.

# TABLE OF CONTENTS

	Page
DEDICATION .....	ii
ACKNOWLEDGEMENTS .....	iii
LIST OF FIGURES .....	v
LIST OF TABLES .....	xi
Chapter	
<b>I. Introduction .....</b>	<b>1</b>
1. RESEARCH MOTIVATION AND BACKGROUND.....	1
2. THEORY .....	2
2.1 <i>Current Technology</i> .....	2
2.2 <i>Proposed Technology</i> .....	10
<b>II. Low Pressure Prototype.....</b>	<b>21</b>
1. EXPERIMENTAL SETUP AND TESTING PROCEDURE .....	21
2. $\alpha$ -PROTOTYPE DESIGN .....	24
2.1 <i>Custom Molding Design</i> .....	24
2.2 <i>Choosing an Existing Elastomeric Product as <math>\alpha</math>-prototype</i> ..	31
2.3 <i>Low Pressure Results and Findings</i> .....	33
2.4 <i>Polyurethane Cord Prototype</i> .....	44
<b>III. Modeling the Full Scale Prototype .....</b>	<b>50</b>
1. MODELING THE ESEHA USING BUCKINGHAM'S II THEOREM.....	50

2.	MODELING THE ESEHA USING ABAQUS FEA SOFTWARE .....	55
2.1	<i>Introduction</i> .....	55
2.2	<i>Material Definition</i> .....	55
2.3	<i>Procedure Definition</i> .....	57
2.4	<i>Modeling Results</i> .....	61
2.5	<i>Series Accumulator Configuration</i> .....	65
3.	CONCLUSIONS .....	68
IV.	<b>Manuscript: Design and Validation of a High-energy Density Elastic Accumulator Using Polyurethane .....</b>	<b>70</b>
1.	ABSTRACT.....	71
2.	INTRODUCTION.....	71
3.	PREScribed TARGET METRICS .....	75
4.	JUSTIFICATION FOR USING POLYURETHANE AS ACCUMULATOR MATERIAL.....	77
4.1	<i>Material Selection</i> .....	77
4.2	<i>Working Fluid Volume and Mass Projections</i> .....	78
5.	PROSPECTIVE VALIDATION .....	82
6.	ALPHA PROTOTYPE ACCUMULATOR DESIGN AND FABRICATION .....	83
6.1	<i>Design</i> .....	83
6.2	<i>Material Selection</i> .....	84
7.	EXPERIMENTAL SETUP.....	86
8.	SYSTEM PARAMETERS PROJECTION.....	90

9. CONCLUSIONS .....	91
Appendix	
A. Materials' Strain Energy Density Chart .....	93
B. Materials' Elongation vs. Fatigue Life Chart.....	94
C. Simulink Diagram: Low Pressure Test Setup Opeartion .....	95
D. Simulink Diagram: Subsystem of Low Pressure Test Setup Operation .....	96
E. Simulink Diagram: Stateflow Chart of Low Pressure Test Setup Operation.....	97
F. Granzow Solenoid Valve Datasheet .....	98
G. GF Signet Flowmeter Datasheet .....	99
H. Noshok Pressure Transducer Datasheet .....	105
I. Andur RT 9002 AP Curable Polyurethane Datasheet.....	107
J. Material Data of Tubing Tested but Not Used as $\alpha$ -prototype .....	110
K. Material Data of Latex Tubing Used as $\alpha$ -prototype .....	113
L. Material Data of Polyurethane Cord Used for $\beta$ -prototype .....	114
M. Bladder (Left) and Shroud (Right) Dimensions in Abaqus Model.....	115
N. Conceptual Schematicl of Bosch-Rexroth Full-scale Experimental Setup.....	116
REFERENCES.....	117

## LIST OF FIGURES

Figure	Page
1	Depiction of the operation of a gas pre-charged accumulator.....3
2	Conceptual PV diagram for PGHA operation .....4
3	Inverse relationship between energy density and efficiency in conventional gas pre-charged bladder accumulators .....8
4	Comparison between experimentally obtained and theoretically determined thermal losses in a conventional gas pre-charged accumulator.....9
5	Pressure-volume relationship for ideal energy transfer in a hydraulic accumulator (note: volume refers to volume of hydraulic fluid in accumulator)... 17
6	Pressure-volume relationship for energy transfer in a conventional gas pre-charged hydraulic accumulator ..... 17
7	Volumetric expansion of latex tubing occurring at constant pressure ..... 18
8	Pressure-volume behavior of an elastomeric vessel ..... 19
9	Low pressure test set-up.....21
10	Uniaxial stress-strain behavior of Andur RT 9002 AP .....25
11	Geometry and dimensions of the $\alpha$ -prototype .....26
12	Ideal volumetric expansion of the bladder within the shroud .....27
13	Pro Engineer Wildfire 4.0 rendition of the disassembled two-part ABS mold for creating $\alpha$ -prototype bladder and photograph of rapid prototyped two-part mold assembled .....27
14	Assembled mold with PU $\alpha$ inside, photograph was taken after vacuum pump was used and the curing process was finished.....28
15	Photograph of PU $\alpha$ bladder .....28
16	Pro Engineer Wildfire 4.0 rendition of the rapid prototyped ABS parts used to create the outer candle wax mold and the insert candle wax mold.....30



17	$\alpha$ -prototype created using a curable silicon cast in an expendable wax mold.....	31
18	Bubble formation occurring at the bottom, with subsequent accumulator expansion occurring through the bladder rolling up the protective shroud.....	34
19	Pre-straining method for designating the location for bubble formation.....	35
20	Pressure-volume behavior of LX $\alpha$ $\alpha$ -prototype.....	36
21	Gravimetric energy density (working fluid included) history, calculated at the completion of the charging phases, of a 3/2" OD, 1" ID LX $\alpha$ tube over $\approx$ 1000 cycles.....	38
22	Roundtrip efficiency history for a 3/2" OD, 1" ID LX $\alpha$ tube for $\approx$ 1000 charge/discharge cycles.....	38
23	1" ID 3/2" OD LX $\alpha$ tube expanding without touching the 6" ID PC shroud .....	41
24	1" ID 3/2" OD LX $\alpha$ tube expanding such that the 3.75" ID PC shroud limits its radial expansion .....	41
25	Average gravimetric retrieved energy density fatigue history for free-expanding and constrained tubes .....	42
26	Average efficiency fatigue history for free-expanding and constrained tubes.....	42
27	Experimental setup for elastic cord strain energy accumulator (front view) .....	44
28	Experimental setup for elastic cord strain energy accumulator (back view) .....	45
29	Conceptual representation of the elastic cord experimental setup.....	46
30	Roundtrip PV behavior of the elastic cord accumulator.....	47
31	Relationship between the dimensionless variable $\Psi$ and peak pressure for different LX $\alpha$ tubes.....	52
32	Relationship between the dimensionless variable $\Psi$ and hold pressure for different LX $\alpha$ tubes.....	52
33	Bladder comprised of three stacked tubes in which the innermost tube is ruptured .....	54
34	Uniaxial tension stress-strain curve of NBR 6212.....	56

35	NBR 6212 data fitted with a 2 <sup>nd</sup> order polynomial curve .....	57
36	Difference between quasi-static and dynamic fill with relation to bladder pressure response .....	58
37	Geometry definition of the bladder and shroud of the accumulator .....	59
38	Time history of the flow rate of hydraulic oil into the accumulator .....	60
39	Progressive contours of bladder expansion taken during the charging process ....	61
40	Model-predicted accumulator PV behavior for the charging process.....	62
41	Strain distribution difference within bladders of different thicknesses .....	64
42	Series accumulator configuration and bladder inflation within a fluid-filled shroud.....	66
43	PV behavior of the $\alpha$ -S-prototype (2 bladders, top curve) as compared to the $\alpha$ -prototype (1 bladder, bottom curve) normalized with respect to change in system volume and holding pressure .....	68
44	Initial rise in pressure just prior to bubble formation .....	79
45	Bubble formation accompanied by drop in pressure .....	79
46	Subsequent deformation under constant pressure.....	80
47	Conceptual pressure-volume expansion behavior .....	81
48	Dimensions of the hydraulic PU accumulator .....	84
49	Stress-strain curve of Andur RT .....	86
50	Schematic of experimental setup .....	87
51	Individual test run procedure.....	88

## LIST OF TABLES

Table		Page
1	Order of operations for charging and discharging the $\alpha$ -prototype .....	22
2	Effect of wall thickness on bladder response .....	65
3	Volume and mass estimates for working fluid (excluding amount of fluid inside bladder prior to loading).....	81
4	Mechanical properties of Andur RT .....	85
5	Estimated system energy density (system defined as elastomer material and portion of hydraulic fluid used for energy storage) .....	91

## CHAPTER 1

### **Introduction**

#### 1. Research Motivation and Background

In 2006, approximately 75 billion gallons of gasoline were consumed by passenger cars in the United States [1]. This astounding figure motivates increasing fuel economy of mass-produced consumer vehicles. The push to reduce gas consumption has resulted in the proposal of a number of different solutions such as the use of hydrogen fuel cells, solar power, and regenerative braking.

A number of the proposed remedies have already made an improvement in fuel economy. For example, regenerative braking (RB) has been effectively implemented on several vehicles such as the Toyota Prius. The purpose of RB is to recover a portion of the energy that is usually lost in slowing down a vehicle with conventional brake pads, allowing to salvage as much as half of the energy used for acceleration [2]. Currently, RB on passenger vehicles is almost universally electrical. However, noting the possibility of achieving significant gains in power capture rate when switching to a hydraulic system from an electrical one, research has been conducted on exploring a new form of RB which will take advantage of the superior power density of hydraulics over electrical systems.

In fact, hydraulic regenerative braking (HRB) has already been successful integrated onto heavy vehicles, such as garbage trucks and buses, resulting in fuel saving

on the scale of 25-30% in city driving [3]. If the fuel efficiency of light passenger vehicles was increased by the same amount in the U.S. in 2006, a total of 18.8 – 26.3 billion gallons of gasoline, costing \$35.6 – \$49.9 billion, would have been saved. Savings on such a large scale led the Center for Compact and Efficient Fluid Power (CCEFP), an engineering research center supported by the NSF, and a number of universities and industrial partners, to fund the work described within this manuscript. The objective of this research is to assess the feasibility of changing to a different energy storage method in order to allow the migration of HRB to the light passenger vehicle sector.

## 2. Theory

### 2.1 *Current Technology*

Before going into the specifics of the proposed solution, it is important to discuss in greater detail some of the drawbacks in current RB technology.

As was previously mentioned, the majority of regenerative braking used today is implemented in the electrical domain. However, there are two fundamental disadvantages of electric regeneration as compared to its hydraulic counterpart. First, electric motors and generators are quite heavy; their power density relative to hydraulic pumps and motors is approximately an order of magnitude lower [4]. Additionally, the charge rate limitation inherent to electrical batteries prevent rapid energy capture required during vehicle deceleration.

Conventional hydraulic regeneration, on the other hand, is also not without its weaknesses. Traditional gas pre-charged bladder hydraulic accumulators (GBHAs) have

an undesirable tradeoff between energy density and efficiency, while also necessitating regular maintenance. The latter issue is due to gas diffusion through the bladder into the hydraulic fluid. This causes undesirable system behavior and requires periodic bleeding of the liquid side of the accumulator. The tradeoff problem occurs due to energy being stored by means of compressing a gas in an elastomeric bladder. Figure 1 is a diagram showing what happens conceptually during the charge and discharge of a GBHA.

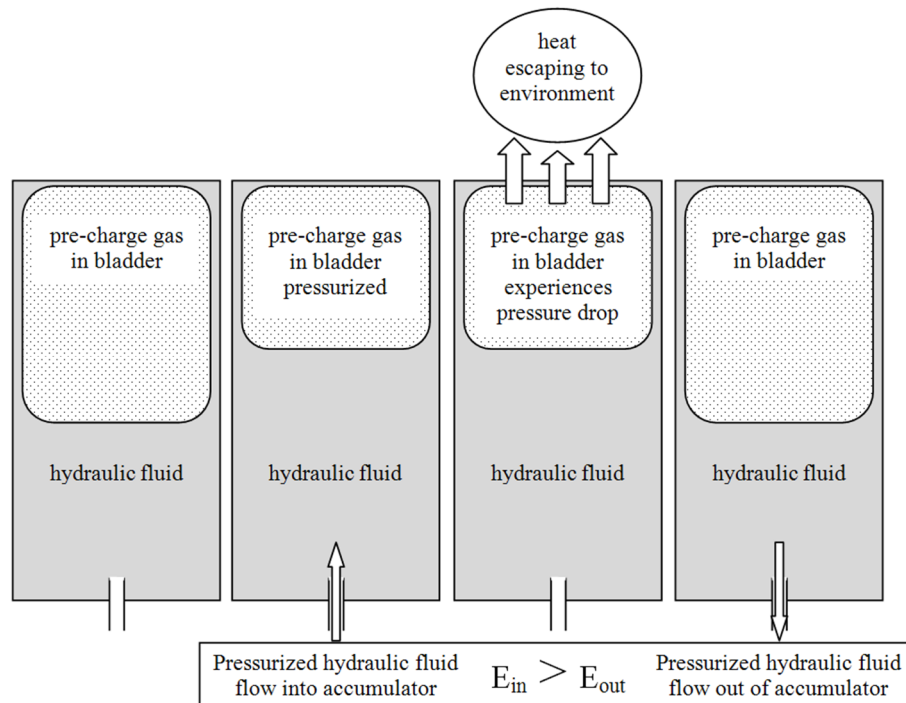


Figure 1: Depiction of the operation of a gas pre-charged accumulator

To store and retrieve energy, a GBHA accepts high pressure flow which compresses the gas in the bladder, holds stored energy after the flow stops, and then returns the stored energy when the flow is allowed to reverse. If a GBHA is used in a RB application, the charging and discharging phases can occur on time scales at least an

order of magnitude faster than the holding times. In such instances, which easily arise when stopping at traffic lights, the heat transfer during the charging/discharging phases is at least an order of magnitude lower than the heat transfer which occurs during the holding phases. In the extreme this can be captured by modeling the charging and discharging phases as adiabatic. The corresponding holding phase is then treated as occurring over a sufficiently long enough time for thermal equilibrium to be established between the accumulator and its environment. These assumptions are illustrated in Figure 2.

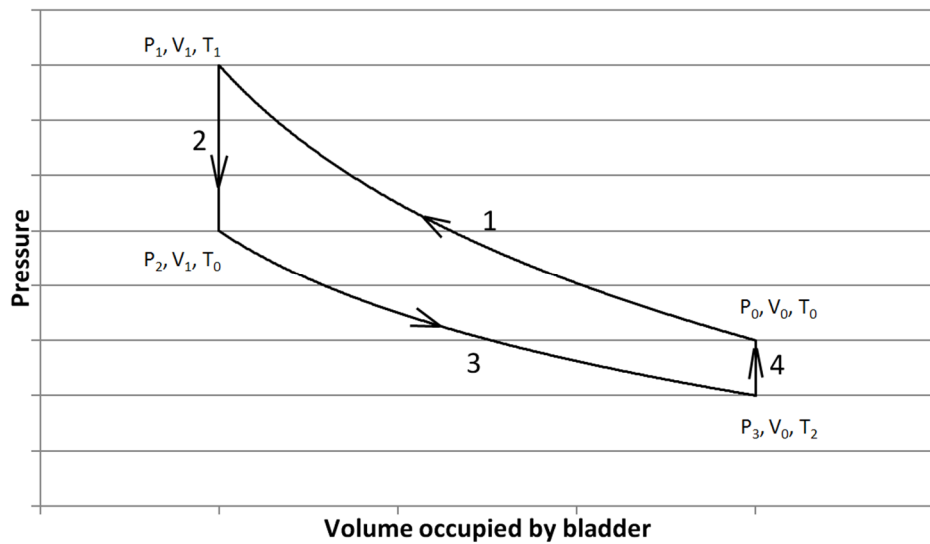


Figure 2: Conceptual PV diagram for PGHA operation

State transitions 1 and 3 represent adiabatic charging and discharging of the accumulator, respectively. During these state changes, the bladder behaves under the constraints described by Equations 1 and 2.

$$PV^k = \text{constant} \quad (1)$$

$$\frac{PV}{T} = \text{constant} \quad (2)$$

In the above equations,  $P$  is the pressure of the gas in the bladder,  $V$  is the volume in which the gas is contained,  $T$  is the gas temperature, and  $k$  is the ratio of specific heats of the gas, which is 1.4 for nitrogen. State transition 2 represents the holding time during which the accumulator remains in its charged state, allowing its temperature to come into equilibrium with the temperature of its environment and for its pressure to undergo a corresponding decrease as dictated by Equation 2. Finally, state transition 4 occurs at a slow enough scale to allow the accumulator's temperature and pressure to increase back to their original values after the accumulator has been discharged.

In automotive applications, minimizing vehicle components' mass and volume are always of high priority; this increases fuel efficiency, and benefits numerous other performance characteristics. The vehicle's RB system is not an exception, the more energy it is capable of storing for a given mass and volume, the better. From Figure 2, it can be deduced that to store larger amounts of energy, the traditional GBHA needs to be charged to higher pressures during state transition 1. Explicitly, the energy stored in the accumulator during state transition 1, is described by Equation 3,

$$W_{in} = \int_{V_0}^{V_1} P dV \quad (3)$$



where  $W_{in}$  is the work input into the accumulator (i.e., energy delivered by additional fluid flowing into the liquid side and compressing the bladder),  $V_0$  is the volume occupied by the bladder in the accumulator's discharged state,  $V_1$  is the volume occupied by the bladder at the end of the charging process, and  $P$  is the pressure of the gas inside the bladder. Solving Equation 3 and using Equations 1 and 2 to rewrite the resulting expression in terms of the gas pre-charge pressure  $P_0$ , the initial bladder volume before it's charged  $V_0$ , the adiabatic constant of the gas  $k$ , and the pressure to which the accumulator is charged  $P_1$ , we obtain Equation 4.

$$\frac{W_{in}}{V_0} = \frac{P_0}{1-k} \left[ \left( \frac{P_0}{P_1} \right)^{\frac{1-k}{k}} - 1 \right] \quad (4)$$

Equation 4 is the negative volumetric energy density of the accumulator's bladder immediately after energy storage. The expression is negative for  $P_1 > P_0$  because energy is being absorbed during the charging process. Not surprisingly Equation 4 shows that energy density increases when the accumulator is charged to higher  $P_1$ . Higher charge pressure in turn causes the gas inside of the bladder to heat up more, which creates a larger temperature gradient between the bladder/accumulator and the environment. This can be shown mathematically by substituting state sets  $P_0, V_0, T_0$  and  $P_1, V_1, T_1$  from Figure 2 into Equations 1 and 2, and solving for  $T_1$ . This yields the result shown in Equation 5.

$$T_1 = \left(\frac{P_0}{P_1}\right)^{\frac{1-k}{k}} T_0 \quad (5)$$

As mentioned before, when  $T_1$  decreases to  $T_0$  (i.e., the accumulator temperature decreases to that of its environment), the pressure inside of the gas bladder drops as well. Consequently, when the flow is allowed to reverse and the accumulator returns the stored energy, the gas expansion inside of the bladder initiates from a lower pressure than that which it was originally compressed to, resulting in lower efficiency. Using the same approach as that which was used to arrive at Equation 4, the expression shown in Equation 6 is derived to solve for the volumetric energy density of the accumulator's bladder after all of the heat generated in the charging process is dissipated to the surroundings.

$$\frac{W_{out}}{V_0} = \frac{P_0^{(2k-1)/k} P_1^{(1-k)/k}}{1-k} \left[ 1 - \left(\frac{P_0}{P_1}\right)^{(1-k)/k} \right] \quad (6)$$

Finally, Equations 4 and 6 are used to create Figure 3 and clearly depict the tradeoff between energy density and efficiency in a GBHA. The figure is created using several key assumptions, the first of which is that the working gas is nitrogen pre-charged to 2000 psi. Second, it is assumed that the accumulator's operation is as shown in Figure 2, it is adiabatic during charging and discharging, and holding and resting times (state transitions 2 and 4) are on a long enough scale for the accumulator temperature to equalize with ambient.

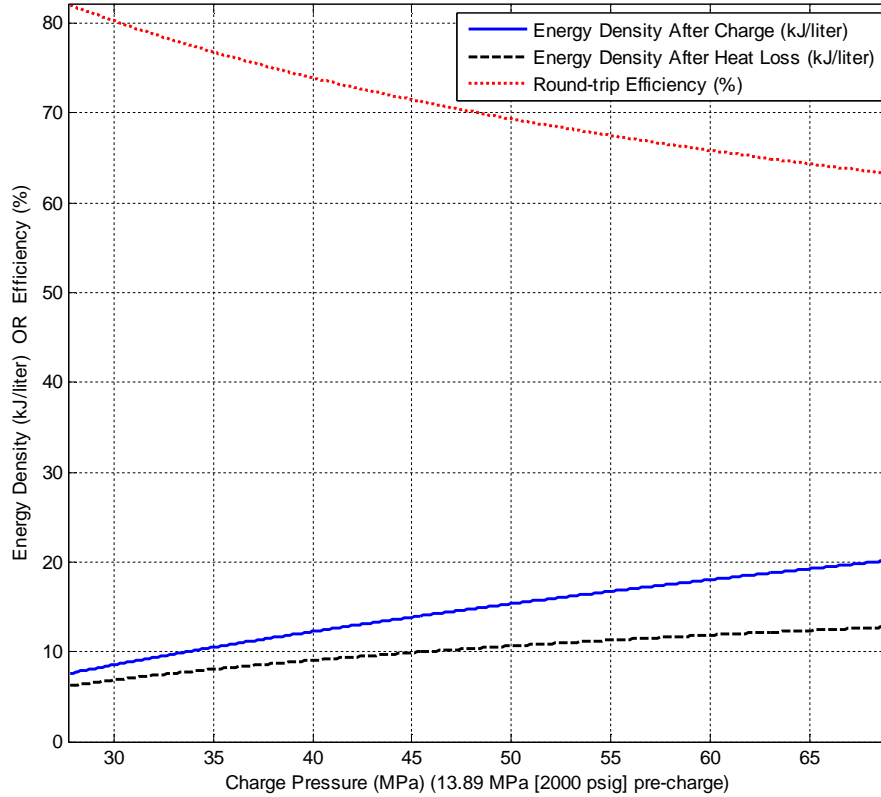


Figure 3: Inverse relationship between energy density and efficiency in conventional gas pre-charged bladder accumulators

Figure 4 was constructed under the same assumptions about accumulator operation, but with a lower nitrogen pre-charge of 500 psig. Its purpose is to graphically compare an experimental efficiency quoted by Pourmovahed et al. The empirical data point was obtained from charging a 500 psig nitrogen gas pre-charged piston accumulator (piston instead of a bladder separates the working fluid from the gas) to  $\approx 3165$  psig, and holding it in the charged state for 100 seconds [5]. Its roundtrip efficiency (neglecting frictional loss and only taking thermal loss into account) was calculated to be 60.1 %, as shown with an “x” on Figure 4. For the same pre-charge and charging pressures, the theoretical efficiency calculated from Equations 4 and 6 is 59.4 %.

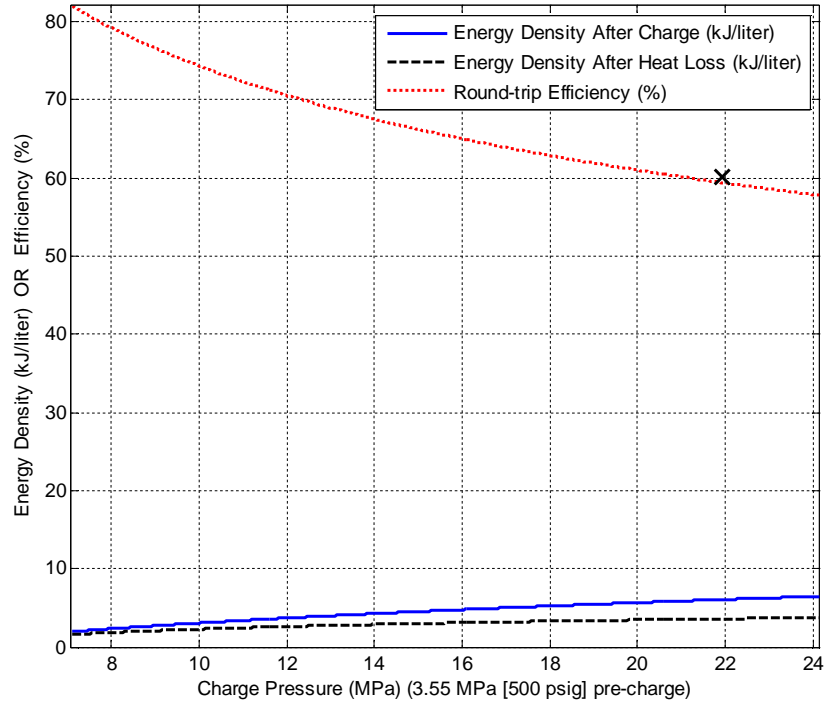


Figure 4: Comparison between experimentally obtained and theoretically determined thermal losses in a conventional gas pre-charged accumulator

The close agreement between the theoretical and experimentally derived efficiencies serves to confirm the susceptibility of conventional gas pre-charged accumulators (both piston and bladder types) to efficiency losses due to heat transfer during extended holding times. Furthermore, the implication of the close match is that the accumulator loses nearly all of the heat generated during the charging process in under one and a half minutes. Holding times on this time scale can be easily encountered at traffic lights, making the conventional GBHA a poor choice for HRB.

## 2.2 *Proposed Technology*

In order to retain the higher volumetric energy density achieved through higher compression of the gas in GBHAs without sacrificing efficiency, several methods to mitigate heat loss have been proposed. One such method that was shown to be successful involves placing elastomeric foam into the gas enclosure to absorb and return the heat generated during gas compression that would otherwise escape into the environment. The foam was shown to be capable of collecting a large amount of the generated heat and returning it to the gas when the latter expands during accumulator discharge. According to Pourmovahed, “the insertion of an appropriate amount of elastomeric foam into the gas enclosure...[can] virtually eliminate thermal loss” [6].

Whereas the approach proposed by Pourmovahed is aimed at allowing the use of hydraulic power in regenerative braking by modifying existing technology, the research discussed in this manuscript is a proposal to achieve the same goal by incorporating a new technology altogether. The advocated technique is to switch from gas compression to material strain as the mechanism for energy storage, as in the case of spring piston accumulators. The suggested method is unique in the fact that whereas conventional spring piston accumulators use metal as the working material, the method proposes to construct a hydraulic accumulator where energy will be stored in an elastomer. Specifically, the proposed hydraulic accumulator can be thought of as an elastomeric bag which stores and returns energy by stretching in response to a quantity of hydraulic fluid being pumped in and out of it.

The accumulator’s unique mode of operation addresses several issues facing existing energy regeneration technology. First, by relying on hydraulic motors/pumps for

charging and discharging, the accumulator takes advantage of the power density and charge rate superiority of these devices over electromagnetic motors/generators. Additionally, the accumulator relies on strain energy as an energy storage mechanism, and is therefore fundamentally different from the storage of energy in a compressed gas. Strain energy storage is achieved through the stretching and rotation of covalent bonds in a material. While some heat is generated in the process of storing and releasing energy by using material strain, the majority of energy is not stored in the thermal domain, as is the case in gas compression and expansion. This allows the accumulator to avoid the thermal losses described in Ch. 1, Section 2.1. Furthermore, not relying on gas for operation has the additional benefit of obviating the need for regular system maintenance due to gas diffusion.

It is of interest to note that spring-piston type hydraulic accumulators (SPHAs) function by capturing energy from the flow of a hydraulic fluid and store it by compressing a heavy spring(s). Since they also use strain in a material as opposed to gas compression, they too avoid the problems inherent to gas pre-charged accumulators. Unfortunately, the masses of SPHAs are prohibitively large to allow their use in a HRB application. This is due to the low gravimetric (or mass specific) strain energy density of their constituent materials.

The volumetric strain energy density  $u_{vol}$  of a material is defined as the total mechanical energy per unit volume absorbed by the material when it is strained to a certain strain value  $\epsilon_f$ . From the expanded form of Equation 7, it can be seen that  $u_{vol}$  is simply the area under the uniaxial loading stress-strain curve of the material starting from zero strain and ending at  $\epsilon_f$  [7].

$$u_{\text{vol}} = \frac{1}{V} \int F dL = \int_{L_0}^L \frac{F}{A_0} \frac{dL}{L_0} = \int_0^{\varepsilon_f} \sigma d\varepsilon \quad (7)$$

In Equation 7,  $V$  is the total volume of material in the uniaxial sample,  $F$  is the uniaxial force exerted on the sample,  $L$  is the length of the sample,  $A_0$  is the original cross-sectional area of the sample,  $L_0$  is the original sample length,  $\sigma$  is the stress acting on the sample, and  $\varepsilon$  is the sample strain. As can be seen from Equation 7,  $u_{\text{vol}}$  is dependent on the extent to which the material is strained. For an application where it is desirable to store and retrieve as much strain energy as possible,  $u_{\text{vol}}$  is taken to be the largest effective value of volumetric strain energy density, evaluated at the largest possible  $\varepsilon_f$  without exceeding the material's elastic limit. Although it is possible to store additional strain energy in the plastic range, it is undesirable; plastic deformation prevents full energy recovery due to hysteresis and damages the material, reducing its service life. Therefore, the maximum practical volumetric strain energy density of a given material,  $E_{\text{vol}}$ , can be calculated using Equation 8 below,

$$E_{\text{vol}} = \int_0^{\varepsilon_{\text{yield}}} \sigma d\varepsilon \quad (8)$$

where  $\varepsilon_{\text{yield}}$  is the yield strain of the material.

Comparing true  $E_{\text{vol}}$  values for a large number of materials requires the uniaxial stress-strain behavior of each material. The costs and time required to collect so much data are prohibitively high. However, assuming linear elasticity, it is possible to obtain

approximations for materials'  $E_{vol}$  values using properties commonly listed in material databases as shown in Equation 9,

$$E_{vol} = \int_0^{\epsilon_{yield}} \bar{E} \epsilon \, d\epsilon = \frac{1}{2} \bar{E} \epsilon_{yield}^2 = \frac{1}{2} \bar{E} \left( \frac{\sigma_{yield}}{\bar{E}} \right)^2 = \frac{\sigma_{yield}^2}{2\bar{E}} \quad (9)$$

where  $\bar{E}$  is the Young's modulus of the material and  $\sigma_{yield}$  is the material's yield stress. Since Equation 9 gives an estimate for the material's strain energy storage capacity per unit volume, multiplying it by the material's density  $\rho$ , as shown in Equation 10, yields the estimate for the storage capacity per unit mass, or the material's gravimetric energy density,  $E_{grav}$ .

$$E_{grav} = \rho E_{vol} \quad (10)$$

Using Equations 9 and 10 with material properties obtained from the CES Material Selector ver. 4.8.0 database, a plot of  $E_{vol}$  versus  $E_{grav}$  ranges was created for a large number of different materials and is shown in Appendix A [8]. Looking at the plot, it can be seen that from the extensive list of ferrous and non-ferrous metals and alloys (represented by teal and purple respectively), molybdenum high speed tool steels have the largest  $E_{vol}$  and  $E_{grav}$  values of  $\approx 17$  kJ/l (17 MJ/m<sup>3</sup> on the plot) and 2 kJ/kg respectively.

In the herein contained research, one metric chosen as a requirement for a hydraulic accumulator suitable for HRB application is the capability of capturing the



kinetic energy stored in a mid-sized 3500 lb ( $\approx 1590$  kg) passenger vehicle traveling at 35 mph ( $\approx 56$  km/hr). Making the simplifying assumption that the kinetic energy stored in the vehicle is approximately equal to that stored in a body of the same mass and undergoing translational motion with the same magnitude as the speed of the vehicle, allows the use of Equation 11.

$$KE = \frac{1}{2}mv^2 \quad (11)$$

Equation 11 is the elementary equation for kinetic energy from classical mechanics, KE is kinetic energy, m is mass, and v is translational velocity. Substituting in  $m = 1590$  kg and  $v = 15.65$  m/sec (35 mph) yields  $KE \approx 200$  kJ. Hence, a hydraulic accumulator needs to be capable of storing approximately 200 kJ of energy if it is required to absorb the total amount of kinetic energy possessed by a 3500 lb vehicle traveling at 35 mph. Dividing this amount of energy by the  $E_{vol}$  and  $E_{grav}$  values of molybdenum high speed tool steels yields 11.8 L and 100 kg. These values are the lower bounds on volume and mass of material that would be required to create the spring(s) in a SPHA suitable for HRB. It is important to note that 100 kg is the smallest theoretically possible mass for only the spring(s) of the SPHA, and does not include the hydraulic fluid, hydraulic lines, reservoir chamber and other accumulator components. The large projected mass of a SPHA based HRB system is the reason why current strain energy type accumulators are not considered as a feasible alternative to electromagnetic regenerative braking.

However, from looking at the  $E_{\text{vol}}$  versus  $E_{\text{grav}}$  plot in Appendix A, it is easy to see that metals and alloys are not the best material candidates for storing large amounts of strain energy. Elastomers such as polyurethane, natural rubber, and polyisoprene have  $E_{\text{vol}}$  and  $E_{\text{grav}}$  values that range from 40 to 400 kJ/l and 30 – 300 kJ/kg respectively. Having up to an order of magnitude higher gravimetric and up to two order of magnitude higher volumetric energy density, elastomers are much better candidates for a constituent material for strain energy accumulator fabrication. In fact, the smallest theoretically achievable dimensions for the working material of a strain energy accumulator using these high energy densities are somewhere between 0.5 and 5 L for volume and between 0.7 and 6.7 kg for mass. This promising lower bound estimate on the mass of an elastomer working material allows strain energy type accumulators to be considered for HRB application.

Using elastomers, such as rubber and polyurethane, is favorable not only due to the high values of the intrinsic properties of these materials, but also because of the design options these properties enable. Configurations, geometries, and operating methods previously not feasible due to the rigidity of metals become available because of the large elongations these materials are capable of. To illustrate, consider ideal hydraulic accumulator behavior is. Hydraulic energy is transferred via a pressurized flow of a nearly incompressible fluid. Mathematically, this statement can be expressed as Equation 12,

$$E_{\text{hyd}} = \int_{t_0}^{t_f} PQ \, dt \quad (12)$$

where  $E_{\text{hyd}}$  is energy in the hydraulic domain,  $P$  is pressure,  $Q$  is flow rate, and  $t_0$  and  $t_f$  are the times when the flow rate initiates and terminates respectively. By noting that flow rate is just the derivative of volume, Equations 12 can be rewritten into a form which uses more intuitive variables to express the energy stored in a hydraulic accumulator. This form is shown in Equation 13,

$$E_{\text{hyd}} = \int_{V_0}^{V_f} PV \, dV \quad (13)$$

where  $V$  is the instantaneous volume of hydraulic fluid in the accumulator,  $V_0$  is the volume in the accumulator prior to energy transfer and  $V_f$  is the volume in the accumulator after the energy transfer is complete. Equation 13 implies that assuming a given hydraulic accumulator is rated for some maximum operating pressure  $P_{\text{max}}$ , it would be ideal for all of its energy storage and energy return to occur at  $P_{\text{max}}$  (i.e., fluid enters and exits at the accumulators maximum operating pressure). Graphically, this is illustrated with a pressure-volume (PV) graph in Figure 5. In the figure, the shaded area represents energy stored and  $P_0$  is the initial pressure inside of the accumulator. In order for the accumulator to store the largest possible amount of energy,  $P_0$  should be atmospheric pressure.

For a conventional gas pre-charged accumulator, the PV behavior differs substantially. Assuming adiabatic compression, using Equation 1, and solving for  $P$  yields

$$P = \text{constant} \cdot V^{-k} \quad (14)$$

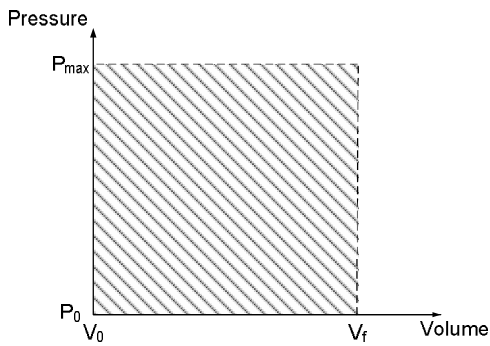


Figure 5: Pressure-volume relationship for ideal energy transfer in a hydraulic accumulator (note: volume refers to volume of hydraulic fluid in accumulator)

The  $V$  in Equation 14 refers to the volume occupied by the gas, and is therefore inversely proportional to the volume of the nearly incompressible hydraulic fluid used on the liquid side of the accumulator. From Equation 14 we can expect the PV and energy storage behavior for a conventional gas pre-charged accumulator to resemble that which is shown in Figure 6.

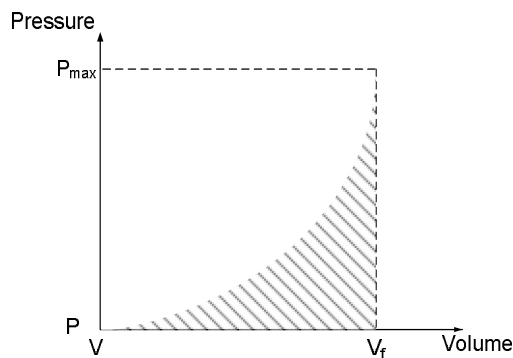


Figure 6: Pressure-volume relationship for energy transfer in a conventional gas pre-charged hydraulic accumulator (note: volume refers to volume of hydraulic fluid in accumulator)

A quick qualitative comparison between Figure 6 and Figure 5 shows that energy storage in a conventional gas pre-charged hydraulic accumulator is significantly inferior in terms of the amount of energy stored for the amount of hydraulic fluid used.

The use of an elastomeric material in a hydraulic accumulator offers a unique alternative configuration the behavior of which more closely approximates ideal energy storage. Figure 7 illustrates this configuration and the associated behavior. The figure shows latex (an elastomer used often to manufacture surgical tubing and rubber bands [8]) tubing tied off at one end and attached to the outlet of a low pressure pump with a pressure gauge at the other. As air is forced into the elastomeric vessel, its initial response is shown in the top frame. A small volumetric expansion accompanied with a pressure increase to  $\approx 25$  psig. As more air is pumped, the vessel experiences an abrupt increase in volume accompanied by a pressure drop to  $\approx 20$  psig, as shown in the middle frame. The bottom frame of the figure shows that as more and more air is pumped into the vessel, volume increases while pressure remains at the  $\approx 20$  psig value.

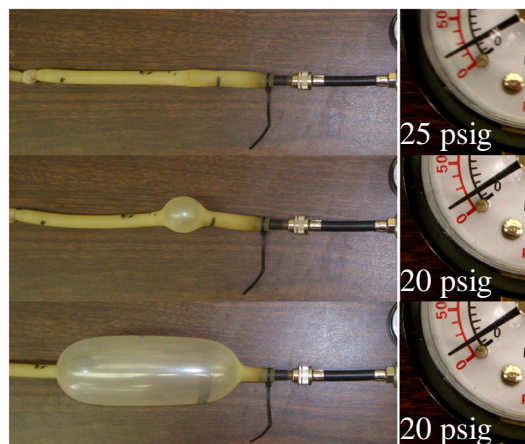


Figure 7: Volumetric expansion of latex tubing occurring at constant pressure

This PV behavior is desirable because of its closer resemblance to ideal hydraulic energy storage when compared to conventional gas pre-charged accumulators, as shown graphically in Figure 8.

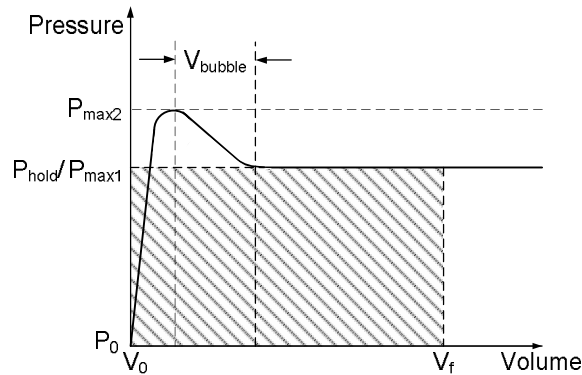


Figure 8: Pressure-volume behavior of an elastomeric vessel

In the above figure,  $V_{\text{bubble}}$  is the change in volume associated with the sudden appearance of the bubble,  $P_{\text{hold}}$  is the pressure at which volumetric expansion occurs after the bubble forms, and the shaded area represents an approximation of the energy stored (note: it is not exactly the area under the PV curve). The reason that Figure 8 contains two differently designated maximum pressures,  $P_{\text{max}1}$  and  $P_{\text{max}2}$ , is to illustrate two possible scenarios. In the ideal case, the accumulator would be able to handle a certain pressure  $P_{\text{max}2}$  for a short period of time that is higher than its rated maximum operating pressure,  $P_{\text{max}1}$ . This would allow for an accumulator to be designed such that  $P_{\text{hold}}$ , the pressure at which energy is stored, is equal to  $P_{\text{max}1}$ . A less favorable scenario is one in which  $P_{\text{max}2}$  is the maximum rated accumulator pressure (i.e.,  $P_{\text{max}2}$  cannot be exceeded even for a short time). If this is the case, energy would have to be stored at a lower pressure,  $P_{\text{hold}}$ , and would therefore not allow the accumulator to store the maximum

amount of energy per volume of hydraulic fluid that it theoretically could. However, for both scenarios, the PV curve assumes a more advantageous shape than the curve shape characteristic of conventional gas pre-charged accumulators shown in Figure 6.

High gravimetric and volumetric strain energy densities, much lower susceptibility to heat losses during operation, elimination of maintenance due to gas diffusion, and unique design options, one of which allows closer mimicking of ideal hydraulic energy storage, are convincing theoretical advantages of an elastomeric strain energy hydraulic accumulator (ESEHA). The following chapters present calculations, observations, modeling and empirical test results which provide further insight into the benefits and difficulties in designing such a device for operation in a HRB system on a light passenger vehicle.

## CHAPTER 2

### Low Pressure Prototype

#### 1. Experimental Setup and Testing Procedure

In order to empirically test the validity of the theory-based claims discussed in Chapter 1, a low-pressure experimental setup was constructed and instrumented as shown schematically in Figure 9. The actual full-sized ESEHA is intended to store 200 kJ and is expected to have a maximum operating pressure of around 5000 psi. Because substantial recourses are required for the fabrication, instrumentation, implementation of necessary safety precautions and testing of an accumulator on such scale, it was decided that preliminary testing should be conducted on a low pressure prototype ( $\alpha$ -prototype) first.

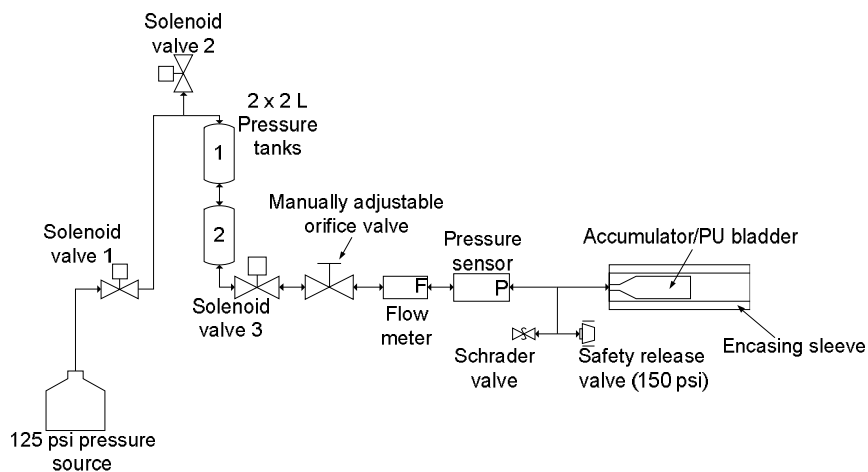


Figure 9: Low pressure test set-up (note: schematic is conceptual, actual orientation of individual components may have been different from what is shown)



The setup depicted in Figure 9 was designed such that three normally closed Granzow series 21EN solenoid valves (PN: 21EN2K0V105, Appendix F) could be used to automatically charge and discharge the  $\alpha$ -prototype (designated as “Accumulator/PU bladder” in the figure). Table 1 shows the necessary operations and the order in which they were carried out for charging the accumulator (bladder inflation), and the operations and their order for discharging it (bladder deflation).

Table 1: Order of operations for charging and discharging the  $\alpha$ -prototype

<b>Order of Operations</b>	<b>Bladder Inflation</b>	<b>Bladder Deflation</b>
1	Set manually adjustable orifice valve	Close Solenoid valve 1
2	Open Solenoid valve 1	Open Solenoid valve 2
3	Open Solenoid valve 3	Open Solenoid valve 3
4	Close Solenoid valve 3	Close Solenoid valves 2 and 3

Prior to testing, the adjustable orifice valve was opened all the way and the setup was filled with working fluid (tap water) by disconnecting the line from the top of 2-liter Pressure tank 1 and pouring water into the system through the freed opening. Working fluid was poured such that it would completely fill the system from the top of Pressure tank 1 to the closed off end of the  $\alpha$ -prototype. A hand vacuum pump was then attached at the Schrader valve and used to remove air bubbles from the working fluid. More tap water was poured into the system to ensure the system was filled with fluid up to the top of Pressure tank 1. The line leading from the pressure source was then reconnected to its original location and the setup was set for testing.

As described in Table 1, it was first necessary to set the manually adjustable orifice valve to control the fluid flow rate (i.e., charge/discharge rates) in and out of the accumulator. With the orifice size set, Solenoid valve 1 could be opened, allowing the 125 psi source to pressurize the working fluid in the 2-liter pressure tanks. Finally, when Solenoid valve 3 was opened, the pressurized working fluid was allowed to flow into the accumulator, at the inlet of which the working fluid's flow rate and pressure were measured using a GF Signet 515 flow meter (PN: P51530-P0, Appendix G) and a NOSHOK 200 series voltage output pressure transducer (PN: 200-200-1-5-2-2-ORF, Appendix H) respectively. The accumulator, the design, geometry and physical dimensions of which are covered in Ch. 2, Section 2, was placed within a protective clear plastic sleeve. The sleeve's originally intended purpose was to serve as a protective shroud in case of accumulator failure. Test results later revealed additional benefits to its use, which are covered later in Ch. 2, Section 2.3.

In the original setup, the plastic sleeve was made from a weak clear material, and hence a 150 psi safety valve was included as a safety precaution to prevent sleeve rupture in case of accidental over pressurization of the system. When the elastomeric accumulator reached intended volumetric expansion/charge level, the charging process was halted by closing Solenoid valve 3.

After the accumulator charge was held for a prescribed amount of time, the system was isolated from the pressure source by closing Solenoid valve 1. The pressure tanks side of the setup was then depressurized by opening Solenoid valve 2. This, in turn, allowed to discharge the elastomeric accumulator by allowing it to contract to its original shape by opening Solenoid valve 3. During discharge, the expelled fluid once again

traveled through the accumulator's inlet, where the discharge flow rate and pressure data was collected.

Solenoid valve control/timing and collection of data from the flow meter and pressure sensor were realized using Simulink ver. 7.1 (R2008a), from Matlab ver. 7.6.0.324 (R2008a) interfaced with a National Instruments PCI-MIO-16XE-10 data acquisition card. The block diagrams and state flow chart used to interface with the experimental setup described above are shown in Appendices C - E.

## 2. $\alpha$ -prototype Design

### 2.1 *Custom Molding Design*

The creation of the first low-pressure ESEHA was driven largely by the volumetric and gravimetric strain energy densities plot displayed in Appendix A. Noting that the plot shows the polyurethane rubber group to contain materials with the highest values for both of these metrics, the constituent material for the  $\alpha$ -prototype was chosen to be a polyurethane (PU). Additionally, in order to have more direct/immediate control on the design and manufacturing processes, as well as to avoid turnaround times, a material which could be worked with using in-lab facilities was sought.

The initial material chosen to be used in the fabrication of the  $\alpha$ -prototype was Andur RT 9002 AP (PU $\alpha$ ), a curable PU from Anderson Development Company. Its properties, the full list of which can be found in Appendix I, such as an elongation of 600%, a tensile strength of 2100 psi, and the capability of being cured at room temperature made it a good candidate for the  $\alpha$ -prototype's constituent material. In

addition to the specifications sheet shown in Appendix I, Anderson Development Company also provided uniaxial stress-strain data of the material, the plot of which is shown in Figure 10.

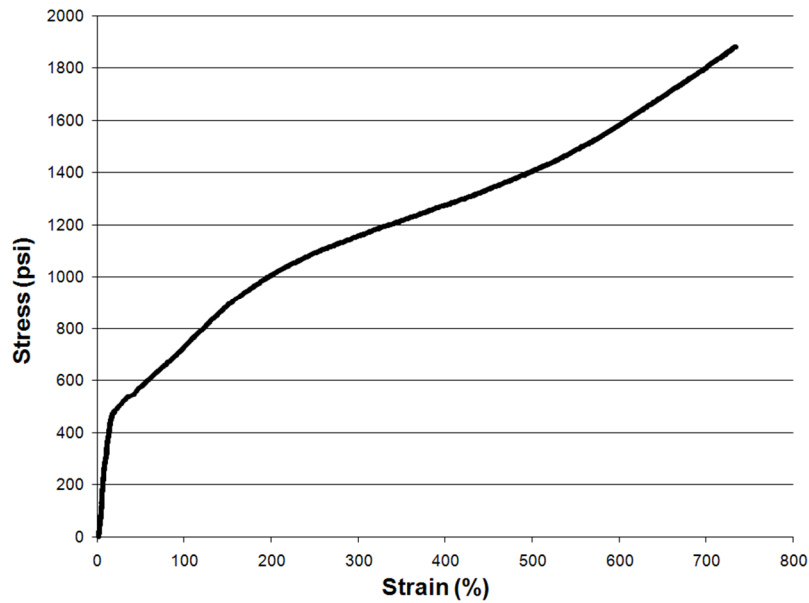


Figure 10: Uniaxial stress-strain behavior of Andur RT 9002 AP

Equation 8 was used on the provided stress-strain data, with  $\sigma$  values expressed in MPa,  $\epsilon$  values expressed as unitless ratios, and strain limit set to  $\epsilon_{\text{yield}} = 6$ , to see how the real volumetric strain energy densities of the material compares to the plot in Appendix A. It's important to note that the actual  $\epsilon_{\text{yield}}$  of the PU $\alpha$  was not in the specifications. However, an elongation of 600% was listed under elastomer service properties and was assumed to be a good conservative estimate of  $\epsilon_{\text{yield}}$  for calculation purposes. Under this assumption, Equation 8 predicts PU $\alpha$ 's volumetric strain energy density to be 45.0 MJ/m<sup>3</sup>, which falls within the PU region for  $E_{\text{vol}}$  shown in the CES Selector plot.

Whereas the  $E_{vol}$  vs.  $E_{grav}$  plot dictated material selection of the  $\alpha$ -prototype, its geometry was heavily influenced by trying to reciprocate the behavior of the latex tubing shown in Figure 7. The  $\alpha$ -prototype was designed in the shape of a closed off elastomeric tube (i.e., a bladder). Since in the experimental setup, this bladder would be charging and discharging inside of a protective shroud, discussed in Ch. 2, Section 1, it included a reduction in its wall thickness at the inlet. The reduction's purpose was to induce initial radial extension at its location, and by doing so, ensure volumetric expansion occurred by the rolling of the bladder along the inside of the shroud. The geometry and dimensions of the  $\alpha$ -prototype are shown in Figure 11 and a conceptual depiction of the desirable bladder expansion within the shroud is shown in Figure 12,

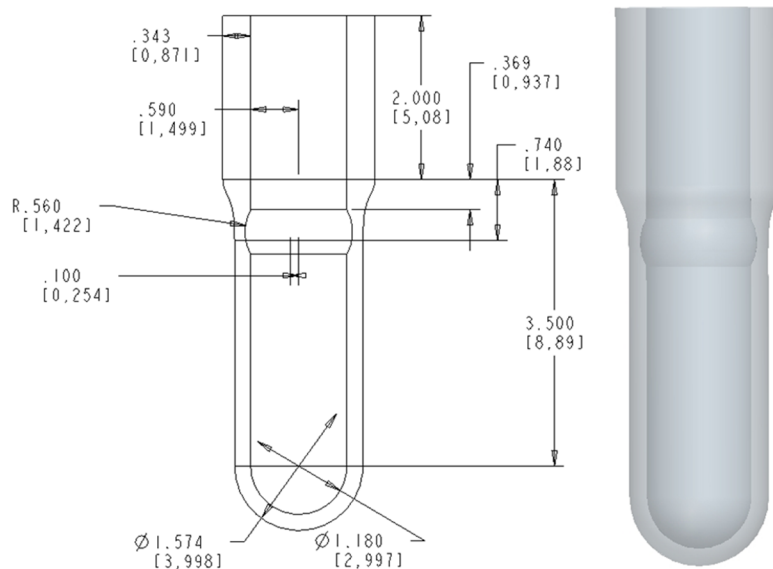


Figure 11: Geometry and dimensions of the  $\alpha$ -prototype

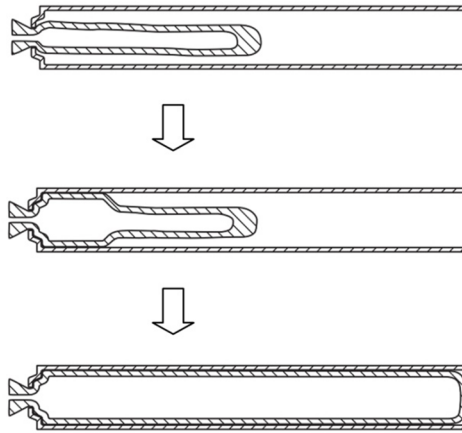


Figure 12: Ideal volumetric expansion of the bladder within the shroud (note: conceptual depiction only, actual shroud and bladder sizes/geometries may differ)

The fabrication of the  $\alpha$ -prototype bladder was achieved using a two-part ABS mold created using rapid prototyping. The outer mold, shown on the right in Figure 13, was sprayed with a chemically non-reactive mold release and filled with PU $\alpha$ . The amount of curable PU $\alpha$  was used such that when the inner mold, pictured on the left and also sprayed with mold release, was inserted, the displaced liquid rose up into the holes at the top of the inner mold, as shown in Figure 14.

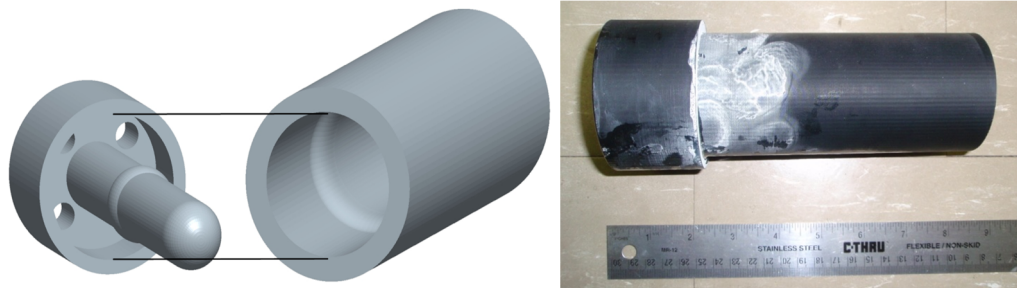


Figure 13 A & B: (A, on left) Pro Engineer Wildfire 4.0 rendition of the disassembled two-part ABS mold for creating  $\alpha$ -prototype bladder (B, on right) Photograph of rapid prototyped two-part mold assembled



Figure 14: Assembled mold with PU $\alpha$  inside, photograph was taken after vacuum pump was used and the curing process was finished

The mold assembly was then placed into an airtight chamber connected to a vacuum pump capable of providing  $\approx 26$  in Hg vac. The pump was operated for approximately five minutes to remove air bubbles. After a 24 hour curing period, all attempts to separate the PU $\alpha$  part from the mold parts without damaging the latter were unsuccessful. Therefore, care was taken not to damage the part as the outside and inside mold pieces were carefully broken using a vice and pliers. A photograph of the bladder, as it looked after its separation from the rapid prototyped mold, is shown in Figure 15



Figure 15: Photograph of PU $\alpha$  bladder

The small cylindrical attachments on the left side of the mold shown in Figure 15 were due to the curable PU $\alpha$  filling the holes of the inner mold insert. Not being part of the design, and serving no functional purpose, they were removed using an X-acto knife. The thin white coat unevenly covering the  $\alpha$ -prototype's surface is the mold release agent; it was rinsed off using tap water before testing.

Unfortunately, the molded  $\alpha$ -prototype failed to perform as intended. During the first charging process, instead of a bubble forming along the entire circumference of the bladder, a small section on the side of the  $\alpha$ -prototype yielded, resulting in a cyst-like growth. Discharging the bladder and charging it again led to yield occurring in the exact same position. When more fluid was forced into the  $\alpha$ -prototype, instead of expansion of the entire bladder, the cyst-like growth grew and burst, rupturing the molded prototype. The failure was attributed to not achieving a sufficiently uniform mold. Small air bubbles were still trapped in the PU $\alpha$  part due to the combination of the low viscosity of the Andur RT 9002 AP and the relatively small size of the four openings in the top of the ABS mold insert (see Figure 14) through which the vacuum pump had to suck the air out.

Another custom molding attempt was made using an expendable mold and curable silicon. Although the silicon elastomers group has a lower range for  $E_{vol}$  and  $E_{grav}$  values than PUs, the much higher viscosity of the chosen material in its uncured state justified its use for low pressure testing. In addition to choosing a material the high viscosity of which would prevent air bubbles from being trapped within the part, a new mold was designed in order to avoid the separating process which was required for the PU $\alpha$  case. The new mold design required two molding stages to create the silicon



bladder. The first stage was to use the rapid prototype machine to create the parts shown in Figure 16.

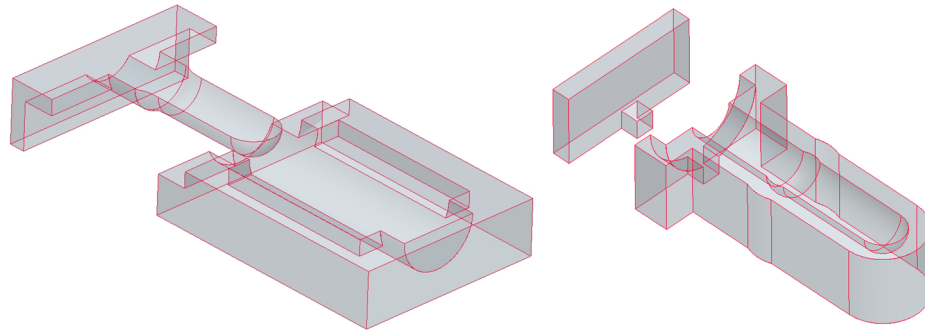


Figure 16: Pro Engineer Wildfire 4.0 rendition of the rapid prototyped ABS parts used to create the outer candle wax mold (left) and the insert candle wax mold (right)

These parts were made with cavities shaped explicitly to cast molds almost identical in shape to those shown in Figure 13 A. Specifically, the molds shown in Figure 16 were filled with candle wax to create two halves of the outer mold necessary to fabricate an  $\alpha$ -prototype bladder and two halves of the inner mold. Candle wax was used so that after the silicon was cured, the mold could be melted away using a hot water bath. This obviated the use of forceful separation of the cured  $\alpha$ -prototype from its mold, avoiding the possibility of damaging the bladder. The produced silicon bladder, shown in Figure 17, failed in the same fashion as the PU $\alpha$  bladder on its first inflation. John Dick states in his text, *Rubber Technology: Compounding and Testing for Performance*, “Most rubber products are cured under pressure...to avoid gas formation and porosity.” [15] Lacking the recourse to perform compressive molding or other methods used for fabricating uniform and bubble-free elastomeric parts (e.g., polymer extrusion), the custom mold

design of the  $\alpha$ -prototype was abandoned in favor of using existing commercially available elastomeric parts.



Figure 17:  $\alpha$ -prototype created using a curable silicon cast in an expendable wax mold

## 2.2 *Choosing an Existing Elastomeric Product as $\alpha$ -prototype*

Forced to abandon the custom molded  $\alpha$ -prototype design, in choosing an existing elastomeric part, it was important to ensure that the constituent material and geometry of the part were as similar to those of the originally intended design as possible.

In respect to geometry, since the ESEHA is conceptually a bladder, existing bladders seemed to be the obvious choice for the group of products to consider. In commercial use, bladders are used to store fluids, gas or liquid, in many different applications and fields. Gas pre-charged bladders are even used in conventional hydraulic accumulators, as previously mentioned in Ch. 1, Section 2.1. However, their primary function in hydraulic accumulators is to act as a membrane separating the gas and liquid

sides, not strain energy storage within their material. Furthermore, these, as well as other bladders, usually exhibit spherical expansion as opposed to that shown in Figure 12.

Since the desired constant pressure volumetric expansion was first observed in a tied off latex tube, elastomeric tubes and hoses were considered next. The obvious issue with geometry (i.e., two openings) was not a major concern, as it could be addressed with a plug capable of handling pressure magnitudes expected in the low-pressure setup. The difficulty was finding a tube made from a suitable material. It needed to be made such that the bubble (see middle frame of Figure 7) would appear at a high enough pressure while also exhibiting highly elastic behavior (i.e., capable of achieving large strain values and returning to its original shape).

Most materials typically exhibit an inverse relationship between their maximum elongation and their ultimate stress. Usually, the stronger the material, the less it can deform before plastically yielding or failing. As discussed in detail in Ch. 2, Section 2.2, the reason elastomeric materials are the prime candidates for manufacturing the strain energy accumulator is their unique ability to reach high levels of deformation before plastically yielding, while simultaneously responding with relatively high magnitudes of stress. In the industry, elastomers are often used for their ability to return to their original shape after deformation. However, usually this deformation is either small, with relatively high accompanying stress on the material, as is the case with shoe soles and rubber engine mounts, or it is large, with relatively low accompanying stress, as in the case of rubber bands. For the  $\alpha$ -prototype, it was desirable to find a tube made from a material that required stress of relatively large magnitude to cause non-permanent large deformation.

Testing conducted on several types of tubes made from a number of PU, neoprene rubber (NEOR), and nitrile rubber (NBR) formulations (material data shown in Appendix J) caused these materials to deform plastically during their first inflation. Ultimately, it was decided to choose tubing of the material in which the desirable PV behavior was originally observed in – latex rubber. Although the latex rubber chosen for testing (LX $\alpha$ ) (material data shown in Appendix K) was weaker than the PU, NEOR, and NBR that were tested (i.e., the bubble formed at much lower charging pressure), it was capable of much larger recoverable strain. This characteristic promoted the use of LX $\alpha$  tubing as the  $\alpha$ -prototype for low pressure testing. Additionally, it was noted that other natural rubbers could possibly be used for the full scale prototype, since the energy densities chart shown in Appendix A shows this group to have  $E_{vol}$  and  $E_{grav}$  values comparable to those of PU.

### *2.3 Low Pressure Results and Findings*

Testing conducted on the LX $\alpha$  low pressure prototype provided valuable insight regarding accumulator expansion behavior, its long-term performance metrics, and the role and importance of the protective shroud; additionally, running low pressure experiments helped determine what should be the next steps in developing the full scale ESEHA.

In Ch. 2, Section 2.1, wherein the design of the custom molded bladder was discussed, it was mentioned that the accumulator's wall was intentionally thinned to induce bubble formation close to the inlet. This design feature was included to cause the rolling expansion behavior depicted in Figure 12, which attempts to minimize the friction between the outer wall of the bladder and the inner wall of its protective shroud. After

switching from the custom molded  $\alpha$ -prototype to existing tubing, there was a concern that the absence of the reduction in the wall thickness meant that there was no control over the location of initial bubble formation. When the bubble growth originated towards the bottom of the plugged tube, as shown in Figure 18, the rolling of the accumulator could occur up the shroud towards the inlet instead of down the shroud away from the inlet. This expansion behavior is similar to that pictured in Figure 12 in that it also does not cause significant friction since the bubble grows by rolling along the inside of the shroud.

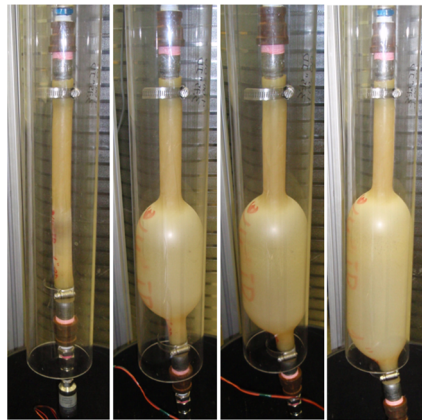


Figure 18: Bubble formation occurring at the bottom, with subsequent accumulator expansion occurring through the bladder rolling up the protective shroud

However, if the development of the bubble occurred in a different location along the accumulator (once observed to happen around the midpoint of a tube), it would cause greater friction with the shroud (compared to bubble rolling expansion) or cause the accumulator to lock up by pinching off fluid flow during the ensuing expansion. This, in

turn could induce premature failure or lead to accumulator efficiency losses and unexpected charge/discharge behavior.

Instead of attempting to reduce the accumulator's wall thickness, which would be difficult to do uniformly without compromising the radial symmetry and strength of the tube, the location of bubble formation was induced using pre-straining. This method is illustrated in Figure 19.

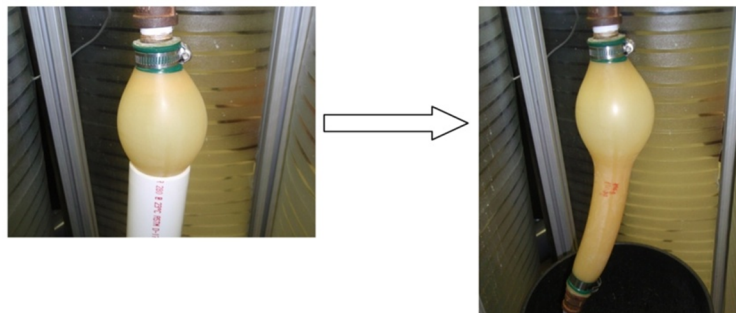


Figure 19: Pre-straining method for designating the location for bubble formation

By placing most of the tube in a hard and narrow ABS pipe, only the portion close to the inlet was left free to expand. The  $\alpha$ -prototype was then partially charged and discharged 10-15 times using a relatively small amount of water, which caused the constrained bladder to undergo partial inflation shown on the left in Figure 19. After the pre-straining cycles, the ABS pipe was removed, and when the accumulator was charged, the bubble first appeared close to the inlet at the desired location as shown on the right in Figure 19. In designing and testing the full-scale ESEHA, this method for affecting the location of initial accumulator expansion will be assessed as to whether it can be used as an alternative to the reduced wall thickness design.

After the pre-straining process, the tubes were tested using the setup and procedure described in Ch. 2, Section 1. The test results yielded several noteworthy findings. First, PV plots constructed from the data collected by the pressure sensor and flow meter were similar in shape to the ideal behavior shown in Figure 8. PV data for several inflations of a 3/2" outer diameter (OD), 1" inner diameter (ID) LX $\alpha$  tube is shown in Figure 20.

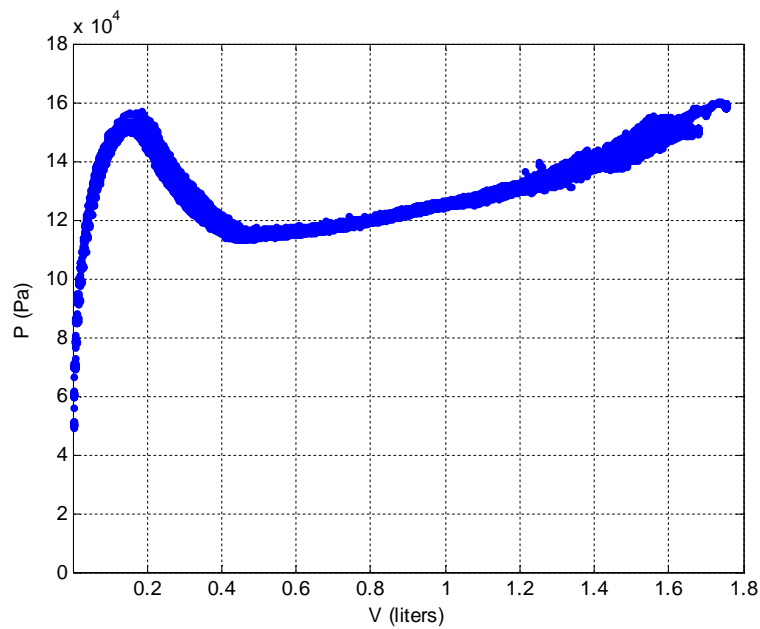


Figure 20: Pressure-volume behavior of LX $\alpha$   $\alpha$ -prototype (multiple inflations)

Although the pressure does not stay exactly constant during volumetric expansion, the PV shape of Figure 20 is indicative of a much more volumetrically efficient method for storing energy than the PV shape characteristic of conventional gas pre-charged accumulators shown in Figure 6.

Due to concession made in material selection and geometry definition (which in turn necessitated the use of lower pressure levels during testing than was originally intended), quantitatively speaking, the  $\alpha$ -prototype's energy storage capacity was quite low (results given later in this section). The approach to improving energy density, as well as its associated challenges, is discussed in Ch. 3, Section 2.4. Despite achieving only low energy storage values the  $\alpha$ -prototype proved useful due to the insight it provided in regard to fatigue behavior and the role of the shroud.

Fatigue has been a concern since the conception of the ESEHA. Appendix B shows an inverse trend between maximum material elongation and its fatigue strength at  $10^7$  cycles (defined as the stress amplitude of a sinusoidally varying stress load about zero mean stress, below which fracture does not occur, or occurs only after a very large number ( $>10^7$ ) cycles) [8]. The plot implies that highly deformable materials such as elastomers should not be subjected to high stresses in order to prevent premature failure due to fatigue. Since higher stresses signify higher strains, and since the ESEHA relies on high magnitude strain levels to perform its function, considerations regarding fatigue life will be weighed heavily during the full scale bladder design process.

As a study of the effect of low volume fatigue, preliminary testing on the  $\alpha$ -prototype was performed to evaluate the rate of performance degradation. Gravimetric energy density (of the system, i.e., taking material and fluid into account) and efficiency data for about 1000 charge/discharge cycles prior to failure (rupture of the bladder) is shown in Figure 21 and Figure 22, respectively. The plots show mean and standard deviation values for groups of 93 charge/hold/discharge (0.6 sec charge, 5 sec hold, 5 sec discharge) cycles of a 1" ID, 3/2" OD LX $\alpha$  tube.



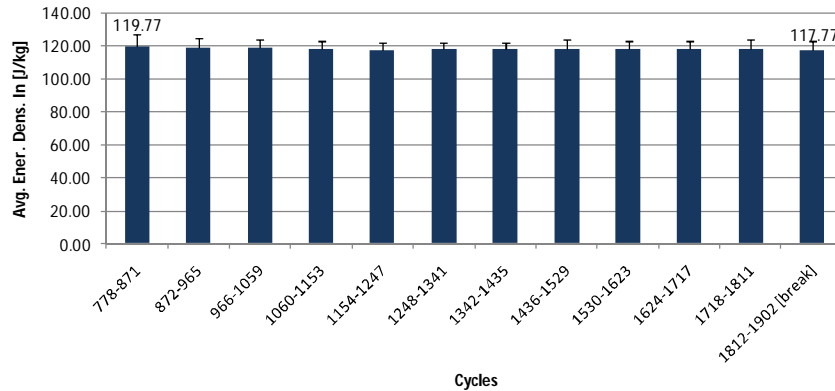


Figure 21: Gravimetric energy density (working fluid included) history, calculated at the completion of the charging phases, of a 3/2" OD, 1" ID LX $\alpha$  tube over  $\approx$  1000 cycles

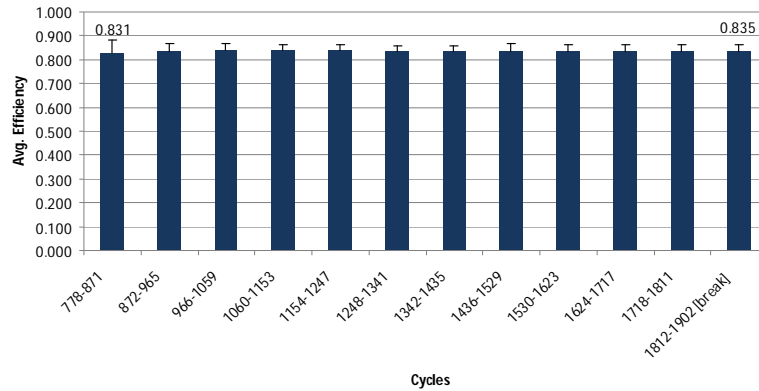


Figure 22: Roundtrip efficiency history for a 3/2" OD, 1" ID LX $\alpha$  tube for  $\approx$  1000 charge/discharge cycles

From the figures, it can be seen that the mean value for  $E_{\text{grav}}$  decreased by  $\approx$  2 J/kg and the mean value for efficiency increased by  $\approx$  0.4 % over the course of 1000 cycles. However, since the standard deviations for the  $E_{\text{grav}}$  groups vary from 4.2 J/kg to 7.1 J/kg, and the standard deviations for the efficiency groups vary from 2.5% to 5%, it can be concluded that the mean value changes in both performance metrics are not

statistically significant. To elaborate, the data provides sufficient evidence to conclude that low volume fatigue testing performed on the  $\alpha$ -prototype did not produce a statistically significant adverse effect on the accumulator's performance metrics prior to failure. Given the conditions under which the data was collected (low pressure, non-optimized geometry and material selection for accumulator, etc.) additional, higher volume fatigue tests (using expected HRB operating conditions) will be carried out on the full scale prototype to confirm consistent and adequate accumulator performance up to failure.

Although energetic performance of the accumulator might not be adversely affected by fatigue, the latter still causes failure. The number of operating cycles an elastomeric bladder can accommodate before rupturing depends on numerous factors such as, but not limited to, the volume of fluid forced into it during charge, the bladder's constituent material, and the bladder geometry. During  $\alpha$ -prototype testing, it was discovered that the safety shroud, which was originally intended to act mainly as a shield to contain water in case of rupture, also significantly affects the tubes' fatigue lives.

In discussing the interaction between the shroud and the bladder, Figure 12 was used to conceptually depict the rolling process. In the figure, it is shown that the bladder expands radially until it comes into contact with the inner wall of the shroud. The subsequent expansion then occurs along the length of the accumulator. The desired PV behavior for an ESEHA, on the other hand, was originally observed in a latex tube not constrained by a shroud (see Figure 7). Therefore, as previously mentioned, the shroud's main intended purpose was to provide shielding after bladder failure, while the rolling expansion behavior was desired only in the case where the bladder's radial expansion

was large enough to bring it into contact with the shroud. When contact between the two components occurred, it was preferred that the bladder would roll along the shroud's inner wall to minimize friction.

During  $\alpha$ -prototype testing, since tubes and shrouds of different sizes were used, there were cases where accumulator expansion occurred with and without contact with the shroud. Throughout the testing, the bladders which made contact seemed to last longer in terms of the number of charging and discharging cycles they went through before failure. This observation led to testing in order to assess the effect of the shroud-bladder interaction on accumulator service life.

In the study, four 1" ID, 3/2" OD, LX $\alpha$  tubes were tested until failure using a 2.95 s fill, 8 s hold, and 9 s discharge operating schedule. The 2.95 s charge time resulted in the tubes being filled with  $\approx 1.7$  L of water during each cycle. While the amount of working fluid each tube was inflated with was kept constant, the volumetric expansion behavior was varied. Two of the tubes were allowed to expand freely (i.e., their expansion was governed solely by the reaction of the rubber to the fluid forced into the tube, as shown in Figure 23), while the other two tubes were placed within a shroud small enough to limit their radial growth (as shown in Figure 24). The tubes which were not constrained by the shroud reached a maximum circumference of  $\approx 18.7$ " in the end of the 1.7 L fill. The shroud used for testing these two accumulators was a rigid polycarbonate (PC) pipe with an ID of 6". As previously mentioned this PC pipe never came into contact with either of the two accumulators it enclosed during testing. The other two tubes were tested inside of a PC pipe with an ID of 3.75". This smaller diameter limited the maximum achievable circumference for the enshrouded bladder to  $\approx 11.8$ ", or  $\approx 63$  %

of the maximum circumference achieved by the unconstrained samples. The results of the fatigue testing are displayed in Figure 25 and Figure 26.



Figure 23: 1" ID 3/2" OD LX $\alpha$  tube expanding without coming into contact with the 6" ID PC shroud



Figure 24: 1" ID 3/2" OD LX $\alpha$  tube expanding such that the 3.75" ID PC shroud limits its radial expansion

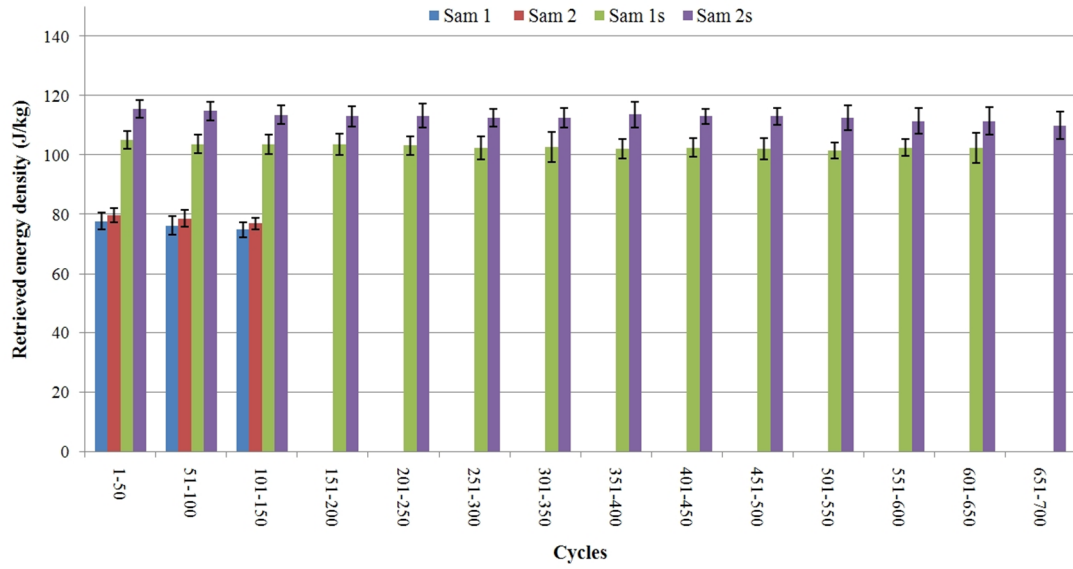


Figure 25: Average gravimetric retrieved energy density fatigue history for free-expanding and constrained tubes

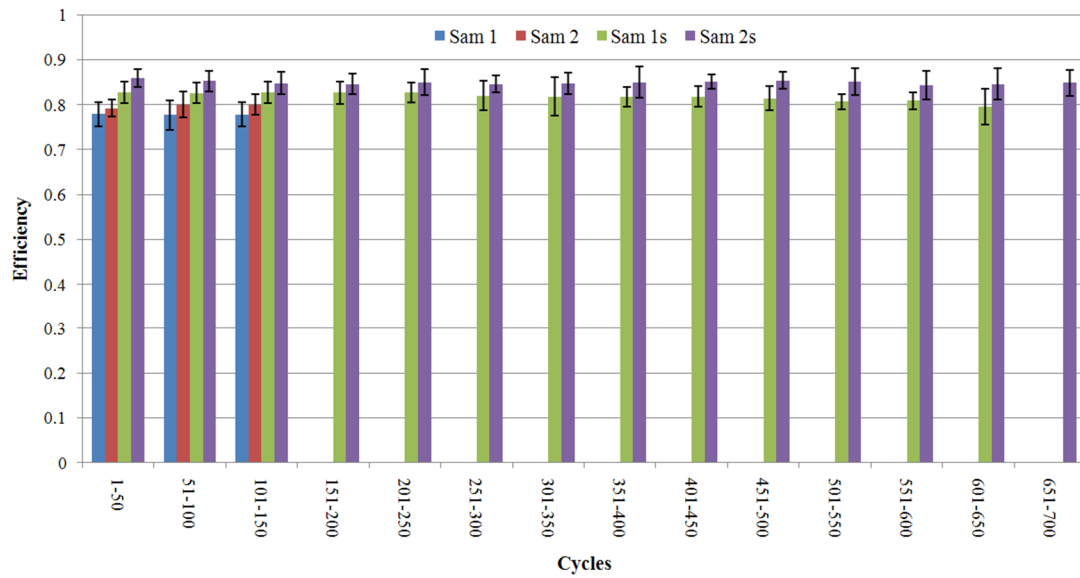


Figure 26: Average efficiency fatigue history for free-expanding and constrained tubes

In the figures above, Sam 1 and Sam 2 represent the two LX $\alpha$  tubes which were allowed to expand freely, while Sam 1s and Sam 2s represent the two samples which came in contact with the 3.75" ID PC tube during expansion. The plots display the average gravimetric retrieved energy density and average roundtrip efficiency (both shown with 1 standard deviation two-sided error bars) for 50-cycle groups over the lifetimes of each accumulator. The presented data shows several differences between shroud-guided and free volumetric expansion; the most evident disparity is the drastic difference in service life. One of the two samples tested inside of the smaller PC shroud underwent 639 service cycles (charge/hold/discharge) before failure, while the other survived 689 cycles. In comparison, the samples that expanded without touching the surrounding 6" ID PC tube succumbed to fatigue-induced failure much sooner; one sample lasted for 153 cycles, while the other ruptured after 140 cycles. In addition to effectively quadrupling service life, the bladders that were limited in their radial expansion also boasted significantly higher average retrieved energy density values for each group of 50 cycles. The roundtrip efficiency values seem to be slightly higher for the constrained bladders as well, however, more data needs to be collected before this difference can be confirmed to be statistically significant. Even if roundtrip efficiency is not increased, the aforementioned fatigue life and energy density benefits warrant the incorporation of a radial expansion limiting shroud in the design of the full scale ESEHA.

Low pressure testing, in addition to providing the results and insights mentioned above, influenced further project development in regards to the modeling approach of the full scale prototype.

## 2.4 Polyurethane Cord Prototype

Before modeling of the full scale ESEHA is discussed in detail, there should be a brief mention of another experimental setup used to assess the effectiveness of a different form of strain energy accumulation.

As previously mentioned, the CCEFP is responsible for funding the ESEHA project. During the project's development, several members from the industry and academia inquired as to why the strain energy accumulator needs to be bladder-shaped and whether simple elastic cords would be able to perform as well, if not better, in a RB application. The experimental setup used to test this hypothesis is shown in Figure 27 and in Figure 28.

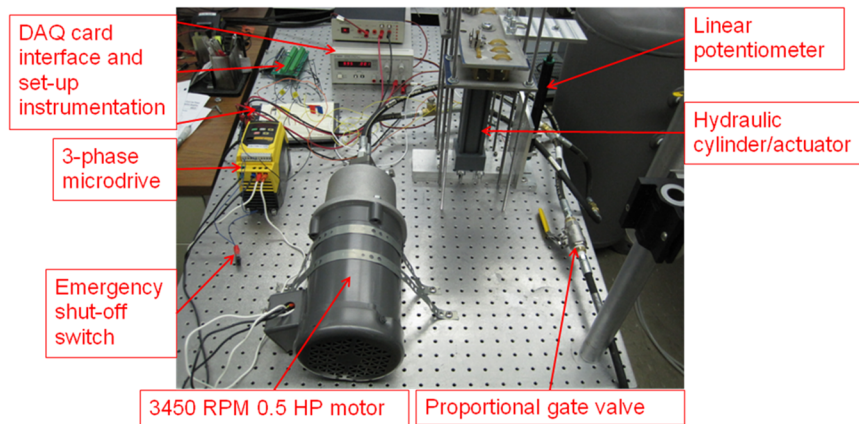


Figure 27: Experimental setup for elastic cord strain energy accumulator (front view)

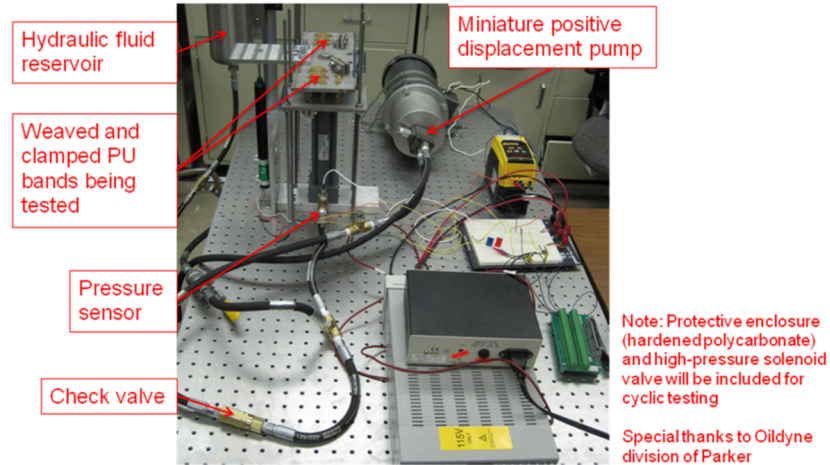


Figure 28: Experimental setup for elastic cord strain energy accumulator (back view)

Since experimentation using the above-depicted setup ultimately showed that an elastic cord accumulator is not a practical substitute for the bladder configuration, the equipment, testing procedure and results will not be discussed in great detail. Instead, the following passages provide a short summary on the testing procedure, some representative data, and the conclusions drawn from experimentation.

The setup shown in the two figures above is represented conceptually in Figure 29. PU cord (material data and dimensions shown in Appendix L) played the role of the elastic strain energy accumulator. Two 4ft long cords were woven through a set of steel plates such that they formed 18 short 1” elastic “springs”. The bottom set of the steel plates was attached to a stationary ground, while the top set was fixed to the piston of a hydraulic actuator. When the accumulator was prepared to be charged, the proportional gate valve was closed and an electric motor was used to power a pump, which forced hydraulic fluid into the actuator. As the piston of the actuator displaced upwards, the 18



lengths of PU cord would stretch, providing an opposing force, while simultaneously storing strain energy.

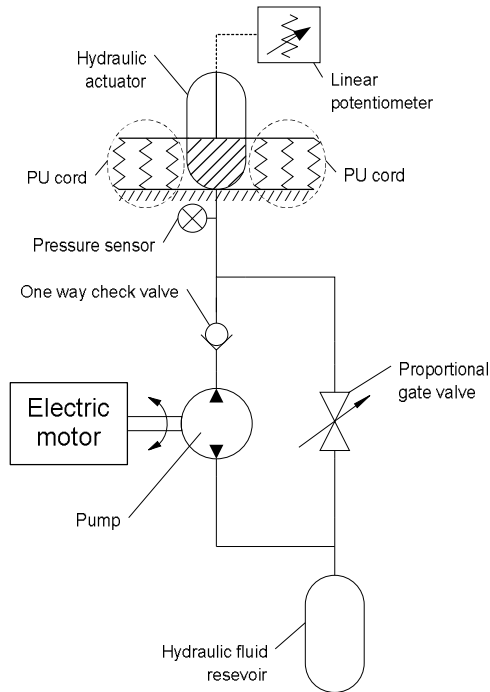


Figure 29: Conceptual representation of the elastic cord experimental setup

The amount of strain energy stored was calculated from the time history of the pressure of the hydraulic fluid, collected using a pressure sensor at the inlet of the hydraulic actuator, and the time history of the volume of fluid inside of the actuator, calculated using the actuator's piston area and the signal from the linear potentiometer which provided the piston's position within the accumulator. After the accumulator was charged, the pump was shut off, and the proportional gate valve was opened. The stretched segments of PU cord would then contract back to their original lengths, while simultaneously pulling down the accumulator's piston and thereby ejecting hydraulic

fluid out of the actuator and into a separate reservoir (at atmospheric pressure). The released energy was measured in a manner analogous to that of the stored energy. A PV diagram for a representative charge/discharge cycle is shown in Figure 30.

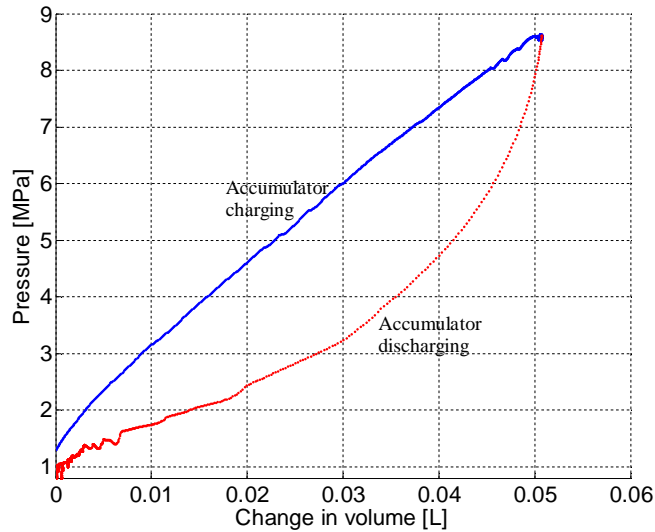


Figure 30: Roundtrip PV behavior of the elastic cord accumulator

Since the elastic cord accumulator required the use of multiple non-optimized components to perform its function (heavy hydraulic actuator, steel plates, etc.), it was not meant to be used in a quantitative comparison of energy density values with the original accumulator concept. Instead, the PU cord setup lends insight into the behavior of an accumulator which relies on the elongation of elastic “springs” as opposed to the volumetric expansion of a bladder. Figure 30 depicts two undesirable behaviors exhibited by the elastic cord accumulator.

The first is the linear increase in pressure during the charging of the accumulator. Comparing this PV behavior to that of the elastomeric bladder depicted in Figure 20, it

can be easily seen that the bladder's ability to keep pressure at a relatively constant level during volumetric expansion makes it a better device from a volumetric energy density standpoint. It's true that the operating pressure level was much lower in the bladder accumulator than it was in the PU cord setup, but modeling presented in Ch. 3, Section 2.4 shows that the desirable PV behavior is retained at higher pressures.

Figure 30 shows another disadvantage of the elastic cord accumulator. The portion of the PV curve which represents the discharging of the accumulator is located significantly lower than the charging section. Since the loop enclosed by the charging and discharging portions of the curve represents lost energy, its relative size in the figure denotes poor roundtrip efficiency. In fact, an efficiency of  $\approx 63\%$  was calculated using the data shown in Figure 30. Additional test runs yielded similarly low efficiency values. Energy loss may be attributed to factors such as valve flow resistance, hydraulic actuator piston friction, and friction between the PU cord and the steel plates it was woven through. In comparison, the efficiency of the  $\alpha$ -prototype is about 20% higher, as it was measured during fatigue testing (see Figure 22). This can be attributed to the relative simplicity of the bladder when compared to the woven cord design. Implementing a method for transforming the flow of hydraulic power into the strain of elastic bands involves more complexity than simply using the same hydraulic power directly by inflating a bladder. More complexity, in turn, results in greater energy loss. Thus, to preserve the advantages inherent to hydraulics mentioned in Ch. 1, Section 1, using a bladder is amongst the best options for preserving high efficiency.

The data gathered from the PU cord setup provided sufficient evidence to reinforce the superiority of the originally proposed bladder design for the ESEHA. The

next step in the development process was to establish an accurate modeling method to allow the scaling of the bladder to meet the originally targeted metrics.

## CHAPTER 3

### **Modeling the Full Scale Prototype**

#### 1. Modeling the ESEHA Using the Buckingham's II Theorem

As mentioned in Ch. 2, Section 2.3, the  $\alpha$ -prototype testing influenced the direction of full-scale prototype modeling. After LX $\alpha$  was selected as the desirable constituent material for use in low-pressure testing, a number of different sizes of LX $\alpha$  tubing were tested in order to examine the effect of geometrical scaling on energy storage. The original intention was to use dimensionless analysis in accordance to Buckingham's II theorem on the performance data of different tube sizes. This approach would enable the formulation of laws to estimate full-scale prototype performance from model data [9].

In trying to predict the operating behavior of an ESEHA accumulator of certain size, two quantities of importance are the hold pressure and the peak pressure ( $P_{\text{hold}}$  and  $P_{\text{max2}}$ , respectively, from Figure 8). The peak pressure is important because it imposes a pressure requirement on the hydraulic system; if the system is incapable of providing  $P_{\text{max2}}$  amount of pressure, the bubble will not form, and subsequent volumetric expansion (i.e., energy storage) will not occur. The significance of  $P_{\text{hold}}$  is that it is the pressure level at which energy storage occurs. Although it was empirically shown that energy storage does not occur exactly at a constant pressure (see Figure 20), the amount of energy stored

by a bladder-type elastomeric accumulator can be approximated by the shaded area in Figure 8, and is hence directly proportional to  $P_{\text{hold}}$ .

Using the data collected during  $\alpha$ -prototype testing and Buckingham's  $\Pi$  theorem-based procedure for arriving at dimensionless variables, the dimensionless quantity  $\Psi$  was selected for modeling purposes.

$$\Psi = \frac{TH}{ID} \quad (15)$$

In the above equation, TH is LX $\alpha$  tube thickness and ID is the inside diameter of said tube. It was hypothesized that there are certain mathematical relationships that exist between  $\Psi$  and peak pressure, and  $\Psi$  and hold pressure.

It is important to note that other physical variables affect hold and peak pressures. These are yield stress, working fluid density, fluid flow rate into the bladder, and possibly the working fluid's viscosity. However, the purpose of the dimensionless modeling discussed in the current section was to determine the effects of geometric scaling alone. Thus material and fluid properties, as well as experimental conditions, were held constant.

To evaluate the effect of  $\Psi$ , LX $\alpha$  tubes 12" in length and with different TH-to-ID ratios were inflated using the low-pressure setup. Their peak and hold pressures were recorded and are shown plotted against different  $\Psi$  values in Figure 31 and Figure 32 respectively.

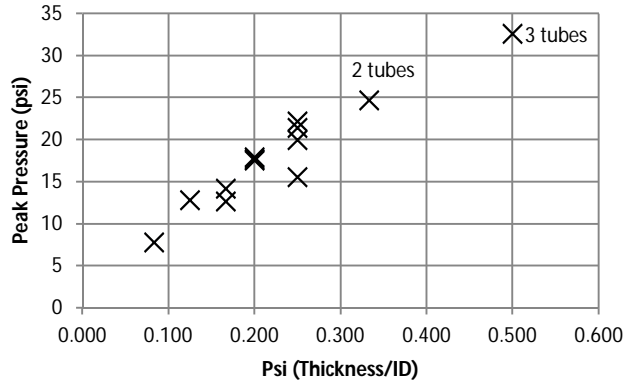


Figure 31: Relationship between the dimensionless variable  $\Psi$  and peak pressure

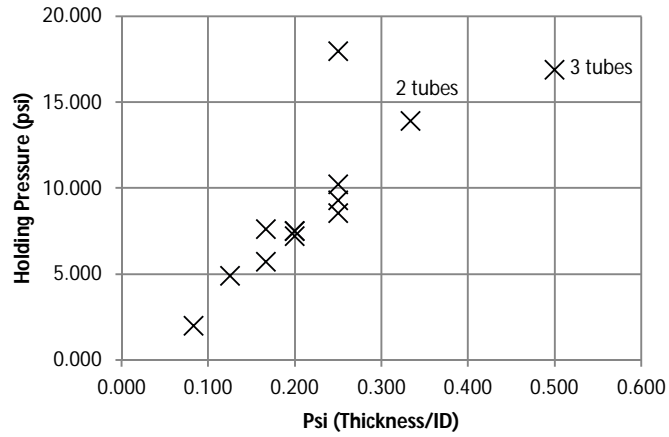


Figure 32: Relationship between the dimensionless variable  $\Psi$  and hold pressure

Both plots show a noticeable positive correlation between  $\Psi$  and the respective designated pressures. For peak pressure, fitting the data with linear and several low order polynomial trend lines yielded coefficients of correlations around  $R^2 \approx 0.9$ ; for holding pressure, using the same fits yielded lower  $R^2$  values in the range of  $\approx 0.7$  to  $0.75$ , due to what is probably an outlier at  $\Psi = 0.25$ .

Although the coefficients of correlation are not quite as large as desirable, the mathematical fits could still have been used to provide some insight into accumulator scaling if it wasn't for the issue encountered with the method used to obtain data for the higher  $\Psi$  values.

The two data points labeled as “2 tubes” and “3 tubes” appearing on both plots were obtained by stacking tubes. To clarify, the largest available  $\Psi$  value for commercially available LX $\alpha$  tubing was 0.25 (ID = 1/2", TH = 1/4"). To increase the dimensionless variable beyond this value, smaller tubes had to be inserted into larger tubes, such that  $OD_{\text{smaller tube}} = ID_{\text{larger tube}}$ . This was intended to simulate the behavior of a bladder which had an ID equal to that of the inner tube, and an OD equal to that of the outermost tube (up to three tubes were stacked in such a way). Unfortunately, during experimentation it was found that a bladder thusly made of stacked tubes could not be relied on to provide accurate results. Since its wall thickness was not homogeneous/continuous, the tubes it was comprised of interacted with each other. Not only did this interaction bring into question the accuracy of how well it represented a homogenous bladder with the same  $\Psi$  value, it also enabled a method of failure which occurred without any visual indication. During a series of test runs, one such bladder made up of three stacked tubes experienced a slight and unexpected performance drop. The initial degradation in performance was not noticed immediately. Luckily, the bladder was undergoing short-term fatigue testing and its peak and hold pressure histories exhibited a continuous decline, reaching an uncharacteristically low level. Since the bladder's appearance did not provide any insight as to the reason for this behavior, it was disconnected from the setup for further inspection. The cause of the drop was eventually



discovered to be the failure/rupture of the innermost tube, a mode of failure which is very difficult to spot without very close scrutiny.

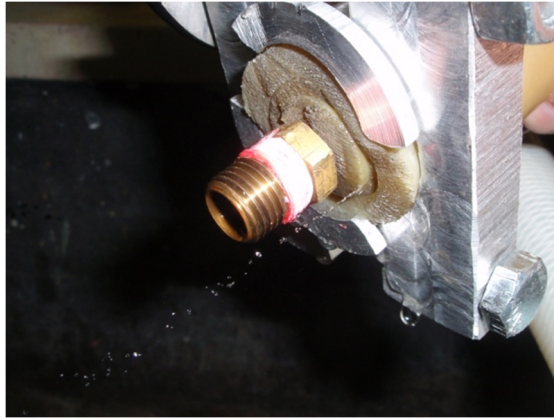


Figure 33: Bladder comprised of three stacked tubes in which the innermost tube is ruptured

Consequently, since friction between stacked bladders can cause artifacts within collected data due to failure which is not only very difficult to spot, but also could not occur in the full-scale prototype, stacking tubes to attain higher values of  $\Psi$  was abandoned.

Finding commercially available hose or tubing with higher thickness to inner diameter aspect ratios is difficult even if elasticity of material is not a consideration. Tubing thickness is usually increased when it is necessary to accommodate slightly higher pressures, but when applications call for much greater pressure ratings, reinforcement such as braiding is chosen over increases in thickness. Due to the commercial availability of hose/tube being as it is, a rather low upper-bound severely limited  $\Psi$  values. This, in turn, made using the Buckingham's  $\Pi$  approach for modeling

the full-scale prototype limit the tubes (made of the material selected for prototype fabrication) to relatively low  $\Psi$  values (of 0.3 or less). Consequently, predicting prototype behavior would require an unacceptably high level of extrapolation. Therefore, this approach was ultimately abandoned in favor of numerical modeling using finite element analysis (FEA) software.

## 2. Modeling the ESEHA Using Abaqus FEA Software

### 2.1 *Introduction*

Abaqus was chosen as the FEA package to model the ESEHA because of its ability to handle hyperelastic material models (where material strains are on the order of 300% - 500%) and the extensive documentation available online [10]. A good model in Abaqus requires accurate and well-defined input for material definition and the type of procedure (conditions, timescale, etc.,) that is to be simulated.

### 2.2 *Material Definition*

In order to accurately model an incompressible elastomer, data for three strain states is required. These strain states are simple tension, biaxial tension and pure shear [11, 12]. Unfortunately, biaxial and pure shear data are quite difficult to acquire not only because these tests require special grips/equipment, and not just a simple uniaxial tension machine, but also because when these tests are carried out, companies tend to keep the data private [13]. Therefore, the initial modeling results presented within this chapter were obtained using available uniaxial simple tension data.

Specifically, the constituent material chosen for modeling the full-scale prototype was a nitrile butadiene rubber formulation from Gates Corporation designated NBR 6212. A plot of the uniaxial tensile stress-strain behavior was provided by Gates and is shown in Figure 34. As can be seen from the curve, the material was chosen due to its capacity to achieve considerably high strain and stress values.

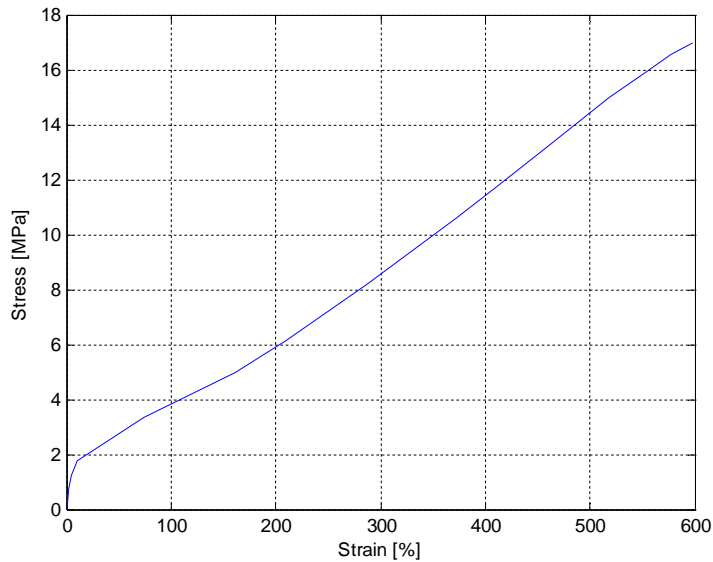


Figure 34: Uniaxial tension stress-strain curve of NBR 6212

The data used for obtaining the curve in the above figure was entered into Abaqus and fitted with a 2<sup>nd</sup> order polynomial curve, as shown in Figure 35. The equation for the curve, having good agreement with the data, was used by the FEA package to predict material behavior in future simulations.

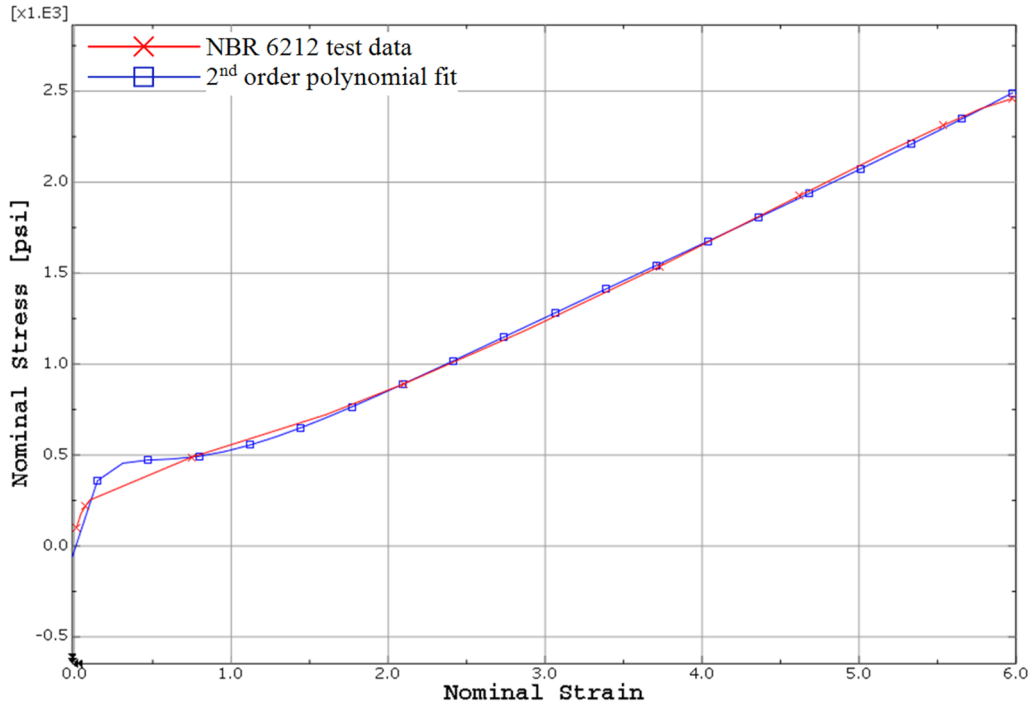


Figure 35: NBR 6212 data fitted with a 2<sup>nd</sup> order polynomial curve

### 2.3 Procedure Definition

With the material behavior defined, it was necessary to decide what sort of an analysis needed to be conducted, static or dynamic. In Ch. 3, Section 1, during the discussion of dimensionless analysis, it was mentioned that bladder response is significantly affected by volumetric flow rate. A simple experiment was conducted to evaluate the extent to which bladder expansion is influenced by volumetric flow rate. An LX $\alpha$  tube (ID = 1", OD = 3/2") was filled at different rates and its response (inside pressure) was observed. A slow quasi-static fill was conducted over the course of approximately 30 seconds, while a fast dynamic fill pumped the same volume of fluid into the tube in about 0.3 seconds. The pressure response to each flow rate is shown in Figure 36.

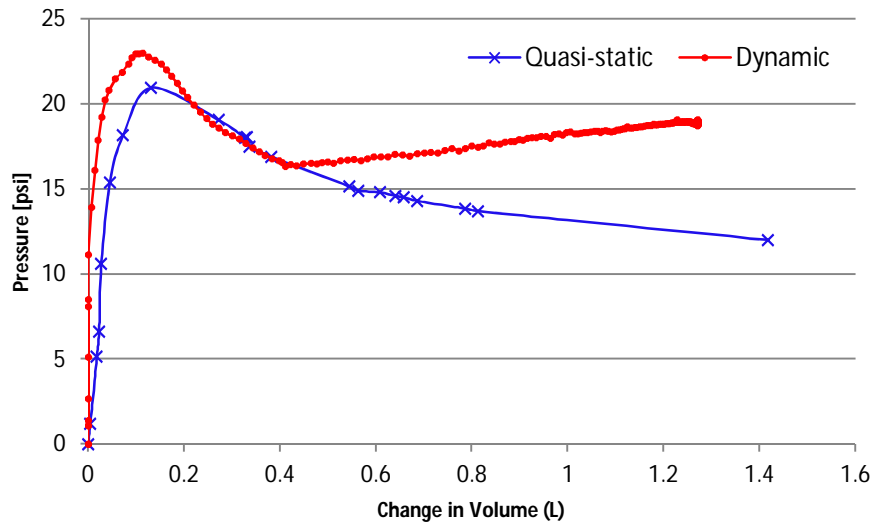


Figure 36: Difference between quasi-static and dynamic fill in terms of bladder pressure response

Since the two curves in Figure 36 are significantly dissimilar, and since the intended application of the elastomeric accumulator requires relatively fast charge, it was deemed necessary to model accumulator function dynamically. The accumulator model was ultimately created using Abaqus/Explicit, which is well-suited for simulating transient, dynamic events and for modeling contact, a feature which was necessary for predicting bladder/shroud interaction.

Using Abaqus/Explicit, an axisymmetric model of the ESEHA was created. The geometry of the axisymmetric bladder and shroud are depicted in Figure 37 (the specific dimensions can be found in Appendix M). As shown in the figure, the bladder was created such that a smaller portion of the geometry simulates a boundary condition clamping effect, while the rest simulates the actual accumulator. The bladder's material

was defined using the data-based 2<sup>nd</sup> order polynomial fit and the density value of 0.045 lb/in<sup>3</sup>. The bladder mesh was comprised of 320 elements biased towards the curvature, where a stress concentration was expected. The shroud was defined as a rigid body, a reasonable assumption to make for a ¼” thick, high-strength steel alloy enclosure under the effect of stress of magnitudes seen in the simulation results. The coefficient of friction between the bladder and the shroud was assumed to be  $\mu_k = 0.1$ , or that of lubricated rubber on steel. It is anticipated that the full-scale design of the ESEHA will include some sort of lubricant/coating to reduce the bladder on shroud friction as much as possible.

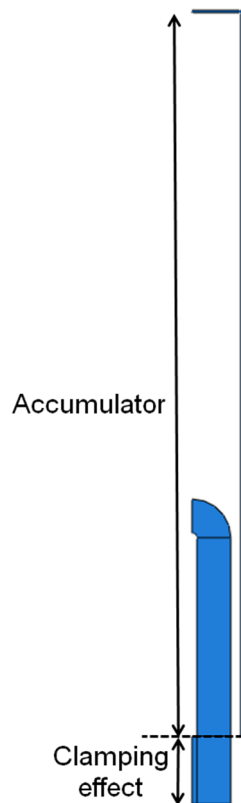


Figure 37: Geometry definition of the bladder and shroud of the accumulator

In the simulation, the accumulator was charged and discharged by prescribing the flow rate of hydraulic fluid (oil density = 0.0343 lb/in<sup>3</sup>, oil bulk modulus = 250,000 psi) into of the bladder's cavity according to the time history shown in Figure 38. This fill magnitude was chosen to elicit a desired bladder response that is discussed in the following section and is not indicative of the amount of anticipated fluid which the full-scale prototype will be charged with. The fill time was chosen based on a series of vehicle braking tests, where the mean time required to stop an average size sedan from 35 mph using non-aggressive braking was found to be  $\approx 4.58 \pm 0.52$  sec (time measured from application of brakes to complete stop).

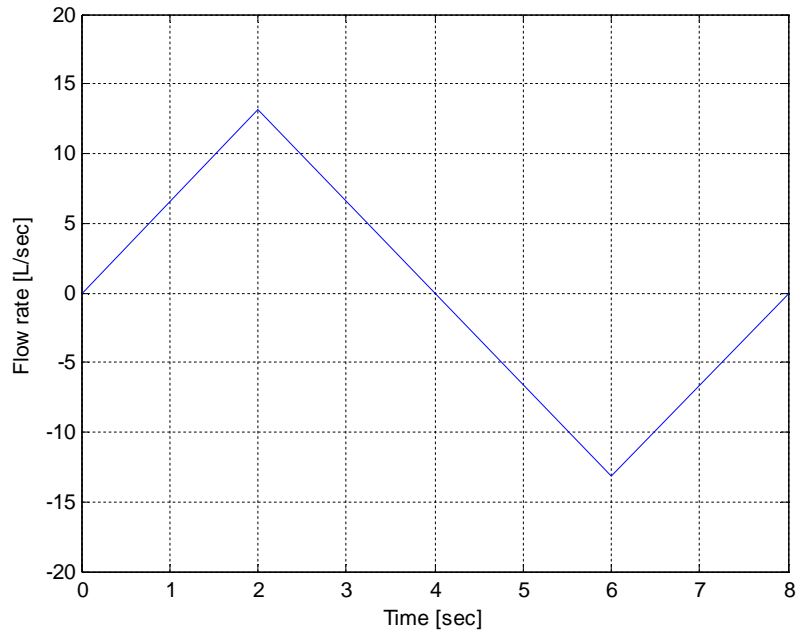


Figure 38: Time history of the flow rate of hydraulic oil into the accumulator

## 2.4 Modeling Results

Four simulation frames showing the bladder's reaction to the flow of fluid into its cavity during the charging process are shown in Figure 39. The contours provide a qualitative check against the type of behavior observed during experimentation. The second frame from the left shows bubble formation and the frames to its right show progressive bubble propagation along the shroud. Figure 39 serves to support the model fidelity as it shows the model to have the same qualitative behavior as was physically observed.

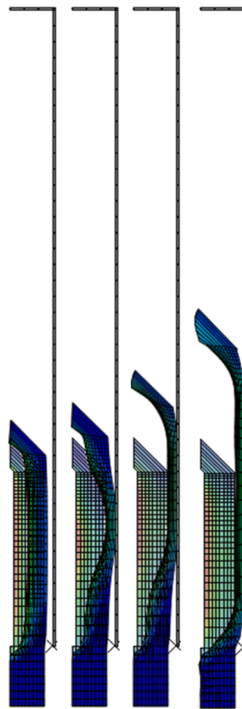


Figure 39: Progressive contours of bladder expansion depicting the charging process (time/volume of fluid inside the accumulator increases from left to right)



Furthermore, as can be seen from Figure 40, the accumulator's cavity's pressure and fill volume correlation is in good agreement with behavior observed during low pressure prototype testing in terms of the PV curve shape. The pressure increase seen during the later stages of inflation is due to additional working fluid being forced into the accumulator after the bubble has propagated all the way through the bladder.

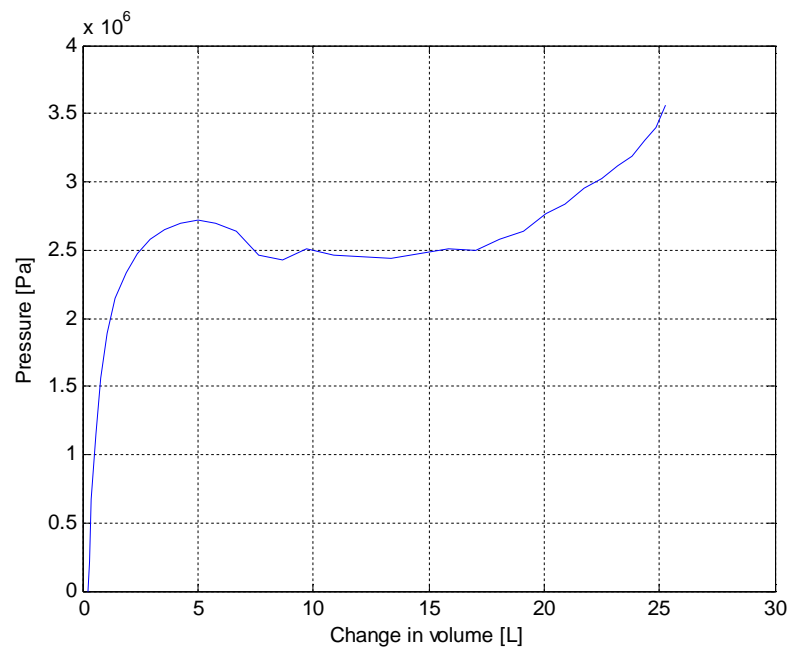


Figure 40: Model-predicted accumulator PV behavior for the charging process

Unfortunately, even with the unexpected pressure increase achieved by the accumulator towards the end of the inflation process, the operating pressure level of the accumulator resulted in unsatisfactory performance.

The desired performance was based off of the uniaxial stress-strain curve of NBR 6212, shown in Figure 34. From the plot, it can be seen that if the material is strained to  $\approx$

475 % (about 125 % short of its limit), it would respond with  $\approx 13.7$  MPa. Its volumetric strain energy density (area under the curve of Figure 34) given those conditions could then be estimated using the following expression -

$$\frac{1}{2} \cdot 4.75 \cdot 13.7 \text{ MPa} \approx 33 \text{ MJ/m}^3 \quad (16)$$

Using this as the material's  $E_{\text{vol}}$ , to store the targeted 200 kJ of energy it would require  $\approx 6.1$  L of material. To compare, the model results show that  $\approx 18.8$  L of NBR 6212 (represented by accumulator portion of bladder as shown in Figure 37) stored  $\approx 74.2$  kJ, resulting in an effective  $E_{\text{vol}}$  of  $4 \text{ MJ/m}^3$ . Using this volumetric energy density,  $\approx 50$  L of material would be required to store 200 kJ.

The poor performance of the modeled accumulator is due to a tradeoff between holding pressure and the strain distribution within the bladder ESEHA design. Figure 41 illustrated this tradeoff. When a thin-walled accumulator is charged, its constituent material is strained relatively uniformly throughout the thickness of the bladder. Conversely, when a bladder with a much larger wall thickness is filled, it exhibits a non-uniform strain distribution along its thickness. Since the accumulator is essentially an elastomeric pressure vessel, the equation for the hoop stress in a thick-walled cylindrical pressure vessel can be used to lend some insight:

$$\sigma_{\text{hoop}} = \frac{r_i^2 p}{r_o^2 - r_i^2} \left( \frac{r_o^2}{R^2} + 1 \right) \quad (17)$$

where  $r_i$  is the inside radius of the pressure vessel,  $r_o$  is the outside radius,  $p$  is the pressure inside, and  $R$  is the radius of interest within the pressure vessel wall. From Equation 17 it can be seen that as  $R$  varies from  $r_i$  to  $r_o$ , so does the hoop stress, and therefore, strain. The larger the range of  $R$  (i.e., thickness of pressure vessel), the more the strain can vary. This is the reason for the inverse relationship between bladder thickness and consistency of strain in the radial direction that is shown in Figure 41.

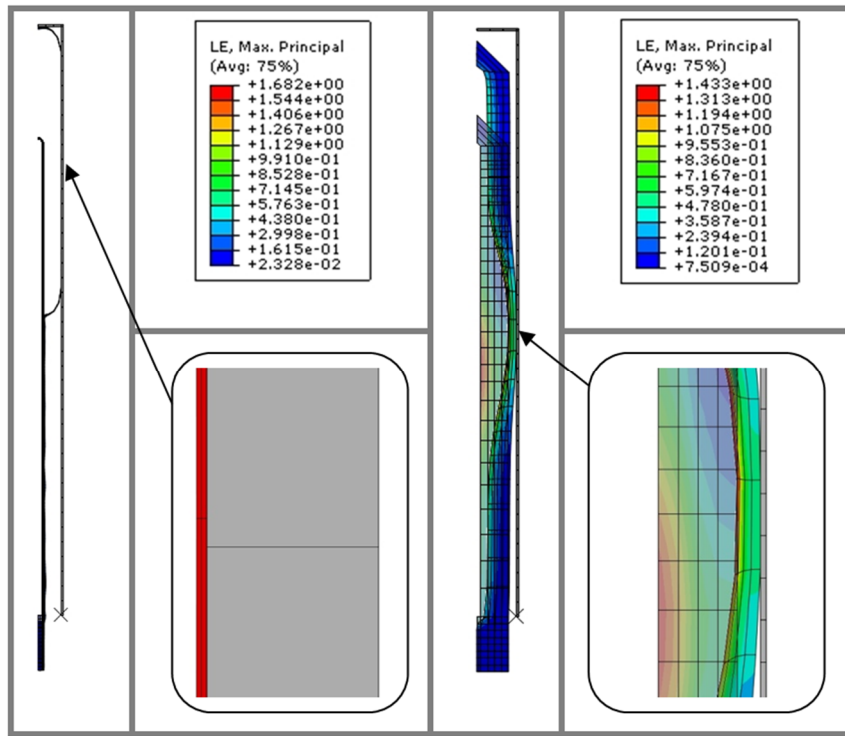


Figure 41: Strain distribution difference within bladders of different thicknesses

However, simply reducing the wall thickness of the accumulator is not a feasible solution to the energy density problem. Although the reduction results in a more uniform strain distribution, it also severely compromises the extent to which the bladder is capable

of pressurizing the working fluid contained within. Table 2 shows some key behavior response parameters for the thin and thick-walled bladders shown in Figure 41.

Table 2: Effect of wall thickness on bladder response

	Hydraulic fluid pressure [psi]	Maximum stress in bladder material [psi]	Maximum strain in bladder material [%]
Thin-walled bladder	≈ 40	≈ 4100	≈ 170
Thick-walled bladder	≈ 350	≈ 3100	≈ 140

The pressure exerted on the fluid by the thicker of the two accumulators is almost an order of magnitude higher than that exerted by its thin-walled counterpart, while the latter actually experiences greater stress values within the material.

## 2.5 Series Accumulator Configuration

One method for addressing the undesirable tradeoff between the distribution of strain and bladder hold pressure is to connect bladders in series. The top frame of Figure 42 shows a low-pressure series accumulator configuration ( $\alpha$ -S-prototype). The setup functions on the same principle as the single bladder accumulator. Working fluid is forced into an elastomeric bladder, which resists expansion, thereby pressurizing the fluid being transferred into it. However, whereas in the  $\alpha$ -prototype, the single bladder provided the resistance to the volumetric expansion, in the  $\alpha$ -S-prototype two bladders are providing the resistance. This is achieved by taking advantage of the fact that bladder expansion occurs based on differential pressure (i.e., the driving mechanism is based on

the difference between the pressure inside of the bladder and the pressure surrounding the bladder).



Figure 42: Series accumulator configuration (top); Bladder inflation within a fluid-filled shroud (bottom)

As fluid enters the  $\alpha$ -S-prototype, it flows into the first sealed tube. In order for bubble formation and energy storage to occur, the pressure inside of the tube needs to be greater by some amount  $P_{\text{expan}}$  than the pressure outside of the tube. The outside of the first tube in the  $\alpha$ -S-prototype is surrounded by working fluid (see bottom frame of Figure 42), which is in direct contact with the inside of a second tube, which is geometrically identical to the first. Since the working fluid and the bladders are incompressible, for the first bladder to expand, it needs to force the working fluid into the second bladder, the outside of which is subjected to working fluid at atmospheric pressure. The second bladder, in turn, also needs to be subjected to a pressure difference of  $P_{\text{expan}}$  for bubble formation and subsequent energy storage to occur. Thus, the inside of the second bladder in the  $\alpha$ -S-prototype, will need to reach a pressure of

$$P_{2nd\_bubble} = P_{expan} + P_{atm} \quad (18)$$

to initiate energy storage through bubble propagation. In turn, for the first bladder in the configuration to do the same, its inside pressure will need to reach

$$P_{1st\_bubble} = P_{expan} + P_{2nd\_bubble} = 2 \cdot P_{expan} + P_{atm}$$

or almost double the pressure inside of the second bladder.

This multiplicative effect of joining elastomeric accumulators in series does not only affect bubble formation pressure, but multiplies the pressure of a single bladder for all levels of volumetric expansion (see Figure 43). Furthermore, provided the compressive strength of the constituent material is sufficient for the first bladder to not fail due to compressive load, more accumulators can be joined in series to proportionally increase the multiplicative effect on pressure.

Although the  $\alpha$ -S-prototype shows that joining accumulators in series allows the use of more uniformly strained bladders without reducing the pressurization of the working fluid, it requires for the system's initial working fluid volume to also be multiplied by approximately the number of accumulators to be used. Therefore, this method requires more investigation before it can be considered for implementation in the HRB application.

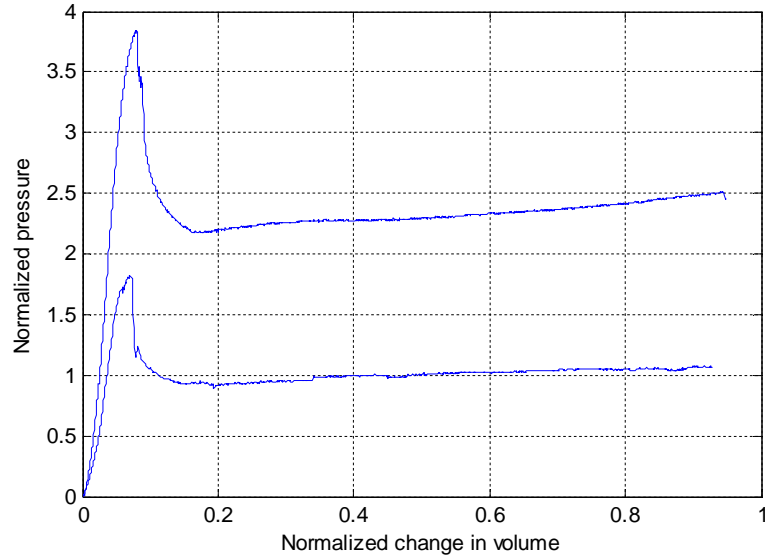


Figure 43: PV behavior of the  $\alpha$ -S-prototype (2 bladders, top curve) as compared to the  $\alpha$ -prototype (1 bladder, bottom curve) normalized with respect to change in system volume and holding pressure

### 3. Conclusions

It has been empirically shown that the PV behavior of an accumulator which stores hydraulic energy by straining a bladder made from an elastomeric material approximates ideal hydraulic energy storage closer than conventional hydraulic accumulators. Low-pressure experimentation ( $\approx 20$  psi) on said type of accumulator has shown how the addition of an appropriately selected protective shroud has the capacity to boost accumulator performance in terms of energy density and fatigue lifetime. Testing performed on an enshrouded accumulator showed that energetic performance does not degrade significantly during low-volume fatigue testing ( $\approx 2000$  cycles).

Using Abaqus/Explicit finite element analysis (FEA) software, a model was created to predict the behavior of larger elastic strain energy hydraulic accumulators

(ESEHAs). The model enabled to calculate expected stress and strain levels within the accumulator material, as well as predict energy storage behavior as calculated from the pressure-volume relationship in the accumulator's working fluid.

Simulations run with the model have shown that fabricating a simple bladder from NBR 6212 (a specific nitrile butadiene rubber) would not provide an ESEHA capable of meeting target metrics for use in hydraulic regenerative braking on a light passenger vehicle. In order to enable the use of hydraulic power in this application, energy density (gravimetric [ $E_{\text{grav}}$ ] and volumetric [ $E_{\text{vol}}$ ]) needs to be increased by either searching for a material with higher  $E_{\text{grav}}$  and  $E_{\text{vol}}$  values than those of NBR 6212, or by altering the simple bladder geometry to allow better use of the chosen elastomeric material.

The work presented within this manuscript is all part of an ongoing project funded by the Center for Compact and Efficient Fluid Power, which is scheduled to run until May 2012. Future work involves plans for additional material research, part of which is obtaining biaxial data to incorporate into FEA in order to improve model fidelity. The series accumulator configuration design is to be further evaluated as to the possibility of decreasing the amount of working fluid necessary for its function (thereby decreasing  $E_{\text{grav}}$  and  $E_{\text{vol}}$ ). Lastly, an agreement is currently being finalized with the Engineering Development Hydraulics department of Bosch Rexroth to enable the testing of full-scale prototype with a desired operating pressure of  $\approx 5000$  psi. A preliminary conceptual schematic of the full-scale experimental setup which will enable cyclical testing of two accumulators can be found in Appendix N.



CHAPTER 4

**Manuscript: Design and Validation of a High-energy Density Elastic Accumulator  
Using Polyurethane**

Alexander Pedchenko, Eric J. Barth  
Department of Mechanical Engineering  
Vanderbilt University  
Nashville, TN 37212

Accepted as a Technical Paper to the  
*2010 ASME Dynamic Systems and Control Conference*

## 1. Abstract

Hydraulic accumulators (HAs) have been used successfully in regenerative braking systems by companies such as Ford and Eaton Corp. to increase fuel efficiency of heavy vehicles by as much as 25-35%. However, the relatively low gravimetric and volumetric energy densities of conventional HAs prohibit their use in average-sized passenger vehicles. In an attempt to address this problem, an elastomer will be used to construct a HA that will use strain as the primary energy storing mechanism. By using strain in the composition material, as opposed to compression of a pre-charged gas, this accumulator should virtually eliminate heat losses due to extended holding times. Because its gravimetric and volumetric elastic energy storage density values are among the highest of any material, polyurethane was the elastomer chosen as the constituent material. Using a curable type of polyurethane, an  $\alpha$ -prototype is currently being manufactured to provide empirical data for validation.

## 2. Introduction

Hydraulic accumulators are energy storage devices commonly used to provide supplementary fluid power and absorb shock. One particularly interesting recent application of these devices is regenerative braking.

A conventional braking system uses friction between brake pads and a brake disk to slow a vehicle down. This method results in energy being wasted as heat. In contrast,

regenerative braking harnesses the kinetic energy of a vehicle during braking, instead of letting it dissipate in the form of heat. This collected energy can then be used in vehicle acceleration, thereby increasing the fuel efficiency. Hydraulic regenerative braking (HRB), specifically, decelerates wheel rotation by having the wheels pump a fluid into a device which resists this fluid's flow and uses its power to harness energy. Although a theoretically appealing concept, hydraulic regenerative braking is difficult to implement due to some major inherent weaknesses of conventional accumulators.

For example, spring piston accumulators use a spring attached to a piston to partition off a certain amount of volume in a container. As working fluid enters the container, it pushes on the piston, forcing the attached spring to contract. The contracting spring stores energy and provides a resistance to the entering fluid. The stored energy is retrieved when the pressure acting on the piston is reduced, allowing the spring to expand and push the piston towards its original position, thereby pushing the fluid back out of the container. The flow returns energy through fluid power.

The primary weakness of these types of accumulators that prohibits them from being used in HRB is their low gravimetric energy density. Using linear analysis, spring steels and titanium alloys have a gravimetric energy density of around 1-1.5 kJ/kg [14]. Consequently, in order to store enough energy to bring a mid-sized 4-door sedan (mass  $\approx$  3500 lbs = 1590 kg) to rest from 35 mph (15.65 m/s), the accumulator spring would have to weigh somewhere from 130 kg to 195 kg. In automotive manufacturing, where minimizing vehicle weight is vital, including such a heavy component would be largely impractical.

Gas bladder accumulators and piston accumulators with a gas pre-charge (PAGPs) use gas for energy storage and, therefore, are much lighter than their spring piston counterparts. In these accumulators, a gas, separated by a bladder or a piston, occupies a certain volume of a container which is otherwise filled with an incompressible fluid. As fluid is forced into this container, the gas inside the separated volume is compressed. In compression, the gas serves a twofold purpose. First, it exerts a pressure which opposes and slows additional entry of fluid into the container. Additionally, the compressed gas stores energy from incoming fluid. Energy stored in this manner can be retrieved when the pressure exerted on the volume of gas in the container is lowered. When this occurs, the gas expands displacing some of the working fluid in the process, thereby returning energy through fluid power.

There are several reasons that these two forms of accumulators are not suitable for use in HRB. Gas bladder accumulators suffer the problem of gas diffusion across the bladder. This introduces gas bubbles into the working fluid which must be periodically removed.

Additionally, both PAGPs and gas bladder accumulators are susceptible to large heat losses. When the gases in these accumulators are compressed, they heat up considerably. If the energy stored in the compressed gas of such an accumulator is not retrieved soon, the heat flow from the gas to its immediate surrounding results in much less energy being retrieved (i.e., much lower efficiency). Pourmovahed et al. showed that with as little as 50 seconds passing between gas compression and expansion, a piston-type gas accumulator's efficiency can fall to about 60% [5]. Since it's quite likely that a

vehicle may remain immobile for around one minute, this makes gas bladder and piston accumulators with a gas pre-charge impractical for HRB applications.

Several methods to mitigate these heat losses have been proposed. For PAGP, one promising method involves placing an elastomeric foam into the gas enclosure. This foam serves the purpose of absorbing the heat generated during gas compression that would otherwise be transferred to the walls of the gas enclosure, and ultimately lost. The foam is capable of collecting a large amount of this generated heat and returning it to the gas when the latter expands. According to Pourmovahed, “the insertion of an appropriate amount of elastomeric foam into the gas enclosure...[can] virtually eliminate thermal loss” [6].

Incorporation of elastomeric foam has shown how accumulator efficiency can be vastly improved through slight modification, making this technology a prominent candidate for use in HRB. The purpose of this work is to propose another method of hydraulic accumulation suited for use in HRB. Unlike the use of foam, however, the proposed approach departs from existing methods as opposed to modifying conventional technology. The advocated technique involves using strain as the mechanism for energy storage, as in the case of spring piston actuators. The difference from spring piston accumulators comes from the fact that an elastomer is chosen as the working material as opposed to a metal. An elastomeric bladder will be tested on its capacity to store and return energy by stretching in response to a hydraulic fluid being pumped in and out of it.

This approach presents a new and unconventional method which aims to avoid the susceptibility to heat losses inherent to gas pre-charged accumulators without foam, while

attaining a higher gravimetric energy density than that of metallic springs. Additionally, the proposed design will be advantageous due to low cost, relative simplicity and good manufacturability.

### 3. Prescribed Target Metrics

In order to ensure that the new accumulator design will be suitable for implementation in HRB, rough performance criteria were developed. The following target metrics were calculated to serve as guidelines during the design process:

1. Capable of storing 195 kJ of energy at a peak power of 195 kW
2. Volumetric energy density of 5 MJ/m<sup>3</sup> or above
3. Gravimetric energy density of 5kJ/m<sup>3</sup> or above

The 195 kJ storage capacity requirement was arrived at by using the classical mechanics equation for kinetic energy, Equation 19, where  $E_k$  is kinetic energy in J,  $m$  is mass in kg and  $v$  is velocity in m/s.

$$E_k = \frac{1}{2}mv^2 \quad (19)$$

An average 4-door sedan weighs approximately  $m = 3500$  lbs (1590 kg). Working under the simplifying assumption that a vehicle of this weight is a point mass experiencing translational rigid body motion of  $v = 35$  mph without rotation (allowing the

use of Equation 19) (56.3 km/h),  $E_k = 194,713 \text{ J} \approx 195 \text{ kJ}$ . This number represents the amount of energy that would be dissipated as heat in traditional braking to stop the vehicle. In HRB, this is the amount of energy that the system should capture, assuming 100% efficiency.

The peak power,  $P$ , at which the energy is to be stored was determined by assuming that in the event of emergency braking, the aforementioned vehicle had to stop within 2 seconds while decelerating uniformly. Equation 19 was differentiated with respect to time in order to obtain the power equation, Equation 20, where  $a$  is acceleration in  $\text{m/s}^2$  and  $t$  is time in seconds.

$$P = \frac{dE_k}{dt} = mv \cdot \frac{dv}{dt} = mva \quad (20)$$

Using Equation 20, with  $a = -7.823 \text{ m/s}^2$ ,  $v = 15.65 - (15.65 \cdot t)/2$ , and  $m = 1590 \text{ kg}$ , the minimum value for  $P$  is  $-194,713 \text{ W} \approx -195 \text{ kW}$ , with the negative sign indicating that the accumulator is storing energy. The value occurring at  $t = 0 \text{ s}$  signifies that the accumulator will be supplied with energy at peak power at the start of the braking process.

The gravimetric energy density requirement was prescribed as  $5 \text{ kJ/kg}$  in order to ensure that the accumulator would not significantly augment the vehicle's weight. Under this constraint, an accumulator capable of storing  $195 \text{ kJ}$  of energy would weigh no more than  $40 \text{ kg}$ , barring the working fluid. The volumetric energy density restriction was

chosen to be similar to the volumetric energy density of titanium alloys. This limit guarantees that the accumulator will not take up more than 0.04 m<sup>3</sup> excluding the working fluid.

#### 4. Justification for Using Polyurethane as Accumulator Material

##### 4.1 *Material Selection*

To see which materials meet the energy density requirements, CES Material Selector ver. 4.8.0 was used. In the initial selection process all material groups were considered. Appendix A shows a graph of volumetric elastic energy storage density vs. gravimetric elastic energy storage density for major material families [8]. The material volumetric energy density values in the graph were calculated under the assumption of linear elasticity using Equation 21,

$$u = \frac{\sigma_y^2}{2E} \quad (21)$$

where  $u$  is volumetric energy density of the material in J/m<sup>3</sup>,  $\sigma_y$  is the material's yield stress in Pa and  $E$  is the material's elastic modulus in Pa. The material's gravimetric energy densities in J/kg, represented by  $w$ , were then calculated by simply dividing a given material's volumetric energy density in J/m<sup>3</sup> obtained from Equation 21,  $u$ , by its mass density in kg/m,  $\rho$ , as shown in Equation 22.



$$e = u / \rho \quad (23)$$

As can be seen from Appendix A, several elastomeric materials boast much higher values for both volumetric and gravimetric energy densities than those exhibited by other material families. Of these elastomeric materials, polyurethane (PU) and natural rubber not only greatly exceed the specified target metrics for energy densities, but also surpass all other materials in these categories. In fact, according to Appendix A, PU's gravimetric energy density is about two orders of magnitude higher than that of titanium alloys. Although both rubber and PU appear to be great candidates, due to the larger possible maximum values (as seen from Appendix A) and its commercial availability, PU was chosen as the material for the new hydraulic accumulator design.

It is important to note here that although Appendix A shows PU to have very impressive values for both energy densities, they should be viewed as rough estimates. The reason for this being that strain hardening makes the application of linear elasticity to elastomers a practice that should be used cautiously. In order to obtain a far more accurate estimate of energy storage capabilities, a stress-strain curve of the chosen PU is required.

#### 4.2 *Working Fluid Volume and Mass Projections*

Results obtained from preliminary testing allowed to make an initial prediction of the volume and weight of the full scale accumulator. Latex tubing was capped off at one end and pressurized at the other by using a pump with a pressure gauge. As air was

forced into this cylindrical elastomeric vessel, the increasing pressure caused a very slight increase in volume as shown Figure 44.

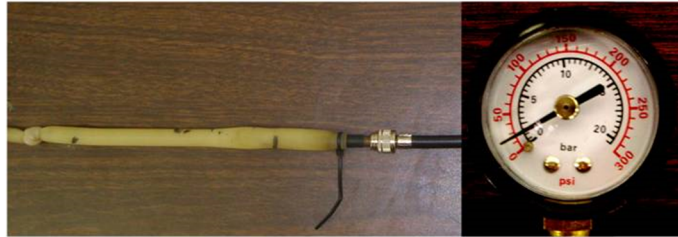


Figure 44: Initial rise in pressure just prior to bubble formation

However, when the pressure reached approximately 17 psig (218.6 kPa), a bubble abruptly formed in the tubing as shown in Figure 45.



Figure 45: Bubble formation accompanied by drop in pressure

Immediately after this bubble formed, the pressure dropped to roughly 13 psig (191.0 kPa). As more air was then forced into the latex cylinder, the pressure stayed at this new value while volume continued to increase as shown in Figure 46.



Figure 46: Subsequent deformation under constant pressure

This type of expansion behavior is shown conceptually in Figure 47. Here,  $V_{init}$  is the initial volume taken up by the accumulator,  $V_{bubble}$  is the abrupt volume increase due to bubble formation, and  $P_{hold}$  is the gauge pressure at which the bubble grows. If the full scale PU accumulator will follow this type of expansion behavior for the accumulator's working range, i.e. pressure will stay approximately at  $P_{hold}$  after the initial drop while volume is increased, its stored energy can be roughly estimated using Equation 24.

$$E_{est} = P_{hold}(V_f - V_i) \quad (24)$$

$E_{est}$  is an estimate of stored energy in J,  $P_{hold}$  is the constant gauge pressure at which the bubble propagates in Pa,  $V_{init}$  is the initial volume occupied by the accumulator containing the working fluid before it is loaded, and  $V_f$  is the maximum volume occupied by the accumulator containing the working fluid at the end of loading, both in  $m^3$ .  $E_{est}$  is represented graphically in Figure 47 with the hatched area.

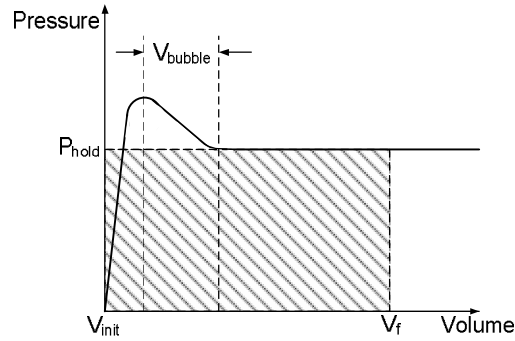


Figure 47: Conceptual pressure-volume expansion behavior

Using Equation 24 and letting  $E_{est}$  equal 195 kJ, estimates for  $(V_f - V_{init})$  were obtained for different  $P_{hold}$  values. Additionally, assuming a working fluid of a similar density to hydraulic fluid (taken to be  $\rho_{hyd} = 890 \text{ kg/m}^3$ ), the obtained  $(V_f - V_{init})$  estimates were in turn used to obtain change in system mass approximations in kg,  $M_f$ . Values for  $(V_f - V_{init})$  and  $M_f$  that would result in energy storage of 195 kJ for different values of  $P_{hold}$  are shown in Table 3.

Table 3: Volume and mass estimates for working fluid (excluding amount of fluid inside bladder prior to loading)

$P_{hold}$ , psig [kPa]	$(V_f - V_{init})$ , ft <sup>3</sup> [m <sup>3</sup> ]	$M_f$ , lb [kg]
3000 [20786]	0.333 [0.0094]	18.45 [8.37]
4000 [27680]	0.250 [0.0071]	13.93 [6.32]
5000 [34575]	0.200 [0.0057]	11.18 [5.07]

As can be seen from Table 3, for the accumulator system capable of functioning with  $P_{\text{hold}}$  values ranging between 3000 psig and 5000 psig, the working fluid outside of the bladder prior to loading is estimated to weigh between roughly 11 lbs and 19 lbs (5 kg and 9 kg) and occupy between  $0.2 \text{ ft}^3$  and  $0.33 \text{ ft}^3$  ( $0.006 \text{ m}^3$  and  $0.009 \text{ m}^3$ ). Although these mass and volume values do not account for the initial volume and mass of the bladder, their small magnitudes serve to indicate that an elastomeric hydraulic accumulator should theoretically be a viable option for HRB application.

## 5. Prospective Validation

In order to test the hypothesis that PU's high volumetric and gravimetric energy densities will allow the construction of a light, compact and energy efficient hydraulic accumulator, a collaborative effort between Vanderbilt University and the University of Minnesota was initiated. Vanderbilt University's Department of Mechanical Engineering is charged with the fabrication of the accumulator, while the University of Minnesota Department of Mechanical Engineering's task is to manufacture a small urban vehicle testbed for testing the accumulator.

At Vanderbilt, prior to investing the capital and time into constructing a full-scale accumulator capable of meeting the prescribed target metrics, a scaled down  $\alpha$ -prototype will be manufactured. The purpose of this  $\alpha$ -prototype is to yield preliminary results, which will help assess the overall feasibility of the project and help anticipate potential problems with the full scale model.

## 6. Alpha Prototype Accumulator Design and Fabrication

### 6.1 *Design*

The  $\alpha$ -prototype accumulator was designed to be a cylindrically-shaped PU bladder that will store and release energy by expanding and contracting in response to an incompressible fluid flowing into and out of it. The bladder's expansion will occur inside of a cylindrical sleeve. The sleeve is meant to serve two purposes. First, it will determine the accumulator's radial expansion limit, forcing the majority of the expansion to occur axially. This type of behavior is preferable to free expansion in a HRB application, where the accumulator expansion should subtract the least amount of volume from the vehicle's cabin. Additionally, the sleeve serves as a safety shield in the event of catastrophic failure, i.e., bladder rupture.

The physical dimensions of the PU accumulator are shown in Figure 48. As noted in the figure, the bladder does not have a uniform wall thickness throughout. Since the bladder is to deform inside of a cylindrical sleeve, it is highly desirable to minimize the amount of friction between this sleeve and the expanding accumulator. Doing so will allow for better axial expansion once these components come into contact.

To address this issue, the section with the smaller wall thickness was included to ensure that when the inside of the accumulator is pressurized, this section will be the first to balloon outward, due to its increased stress concentration (supported by finite element analysis performed using MD Patran/Nastan). Because the nozzle for delivering the fluid will be positioned inside the first 2 in (5.08 cm) of the bladder, this thinner wall section

will be located at the base of the part of the accumulator that will undergo expansion. Therefore, this should ensure that the base of the accumulator's expanding portion will be the first to come into contact with the surrounding sleeve. Following this first contact, the bladder will be able to propagate axially by rolling on the sleeve's inside walls. This type of axial expansion produces the desired effect of minimizing sliding friction between the accumulator and the sleeve.

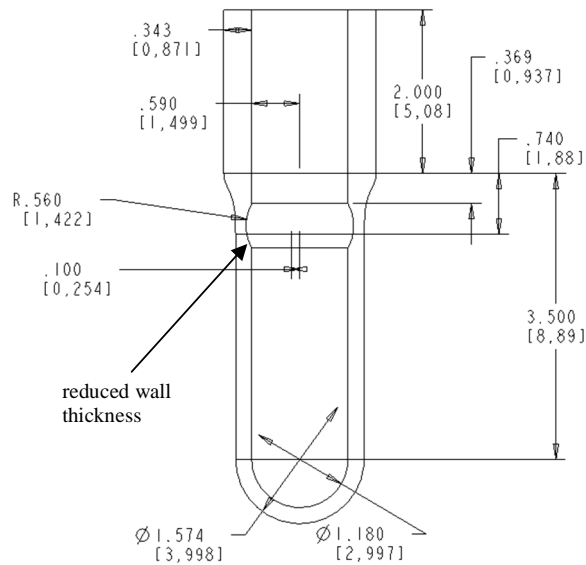


Figure 48: Dimensions of the hydraulic PU accumulator

## 6.2 Material Selection

The  $\alpha$ -prototype accumulator will be fabricated using Andur RT 9002 AP (referred to as PU $\alpha$  hereafter). Manufactured by Anderson Development Company (ADC), PU $\alpha$  is a room temperature curable PU which allows the bladder to be cast using

a disposable wax mold that will be subsequently melted away from the finished part. A few key mechanical properties of Andur RT, as specified by ADC are listed in Table 4.

As can be seen in the table, PU $\alpha$  possesses a high maximum elongation while also maintaining a relatively high elastic modulus, making it a viable material candidate for the accumulator.

Table 4: Mechanical properties of Andur RT

Physical property	Imperial Value	Metric Value
Tensile Strength	2100 psi	14.48 MPa
Elastic Modulus @ 100% elongation	790 psi	5.45 MPa
Elastic Modulus @ 300% elongation	1200 psi	8.27 MPa
Maximum elongation	600 %	

For reasons mentioned in *4.1 Material Selection*, to get a better estimate for the volumetric energy density of PU $\alpha$  a stress-strain curve of the material was obtained from ADC. This curve, shown in Figure 49, was fitted with a 3rd degree polynomial, yielding a correlation coefficient of 0.986 thereby indicating that the polynomial was a good fit for the data. Using the equation for energy stored per unit volume, Equation 25, in conjunction with the polynomial estimating the stress-strain curve allows theoretical volumetric energy density values to be obtained for different extension ratios of the material.

$$u = \int_0^{\epsilon_f} \sigma d\epsilon \quad (25)$$



In Equation 25,  $\sigma$  is the stress (Pa),  $\epsilon$  is the extension ratio, and  $\epsilon_f$  is the extension ratio at which the volumetric energy density is to be calculated. For extensions between 400% and 600% ( $\epsilon_f = 4$  and  $\epsilon_f = 6$ ), this equation predicts PU $\alpha$  to have a volumetric energy density between 25.6 MJ/m<sup>3</sup> and 45.0 MJ/m<sup>3</sup>. These values fall within the range of the volumetric energy density for PU predicted by CES Material Selector in Appendix A.

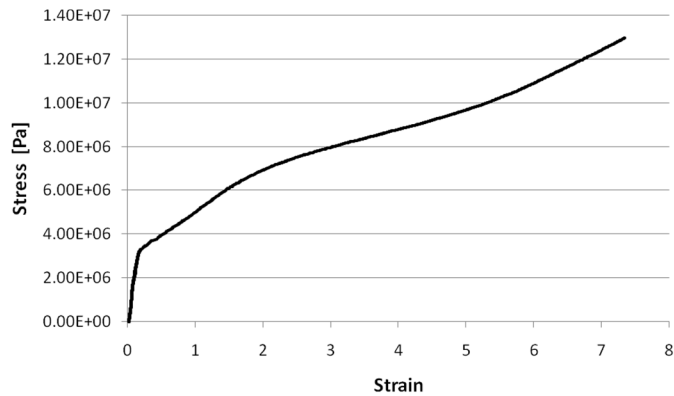


Figure 49: Stress-strain curve of Andur RT

## 7. Experimental Setup

Once the PU $\alpha$  RT accumulator is manufactured, its energy storing capability will be tested using the setup shown in Figure 50. In this setup, a 125 psig (963 kPa) driving pressure acts to force water into a PU bladder. Initially, the line leading from solenoid valve (SV) 1 to the two 2 L pressure tanks will be detached and the system, from the tanks to the bladder, will be filled with water. To ensure accurate results, the water-filled part of the system will be bled of air by using a handheld vacuum pump attached at the

Schrader valve. Additional water will be poured into the tanks to make up for any losses resulting from the bleeding process. All SV's will then be closed and the line leading from SV 1 will be reattached to the pressure tanks.

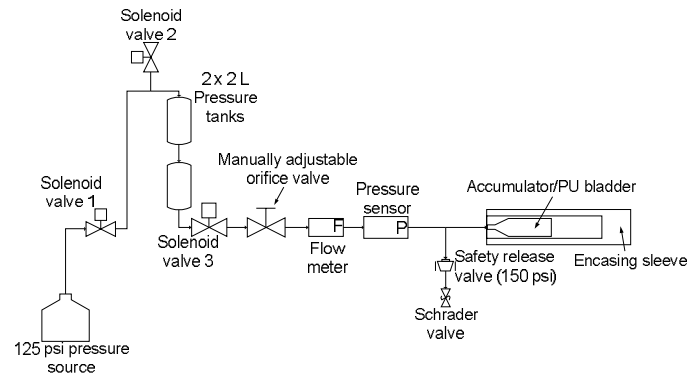


Figure 50: Schematic of experimental setup

All valve control and acquisition of sensor data will be done electronically. The manually adjustable orifice valve will be set to a specific position between separate test runs. Incrementally adjusting this valve will allow to determine the effect of different rates of loading/unloading on energy storage. Each individual test run will be conducted as shown in Figure 51:

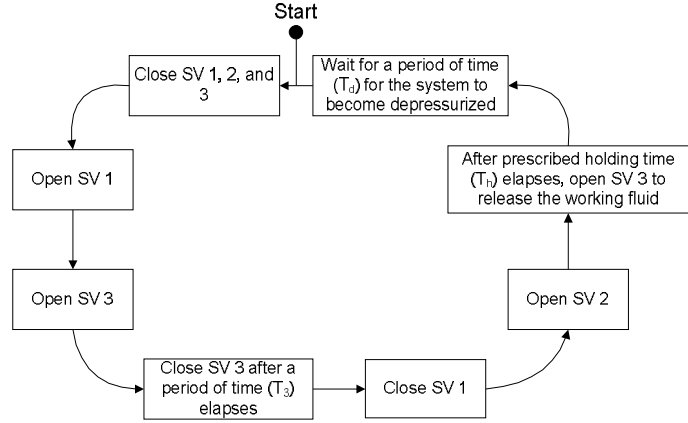


Figure 51: Individual test run procedure

The instantaneous readings from the flow meter ( $Q$ ) and pressure sensor ( $P$ ) will be integrated as shown in Equation 26 in order to obtain energy stored in, and retrieved from, the PU bladder,

$$E = \int_{t_0}^{t_f} PQdt \quad (26)$$

where  $t_0$  is time at which SV 3 is opened and  $t_f$  is time at which SV 3 is closed. When the water is flowing into the bladder,  $E$  in Equation 26 represents energy stored ( $E_{in}$ ) and  $t_f - t_0 = T_3$ . When the water is flowing out of the bladder,  $E$  in Equation 26 represents the energy retrieved ( $E_{out}$ ) and  $t_f - t_0 = T_d$ .

These values will also be used to calculate the volumetric accumulator energy density ( $E_{vp}$ ), gravimetric accumulator energy density ( $E_{gp}$ ) and energy efficiency ( $\eta$ ) of the system. It is important to draw the distinction between the energy density values of

the accumulator and those of the accumulator material. The difference is in that the energy densities of the accumulator include the weight and volume of the working fluid in their calculations, whereas the accumulator material energy densities do not.  $E_{vp}$  will be determined by using Equation 27,

$$E_{vp} = \frac{E_{in}}{V_0 + \int_{t_0}^{t_f} Q dt} \quad (27)$$

where  $V_0$  is the original volume of the bladder and the working fluid before the accumulator is pressurized.  $E_{g\rho}$  will be determined by Equation 28,

$$E_{g\rho} = \frac{E_{in}}{m_0 + \int_{t_0}^{t_f} Q dt \cdot \rho_w} \quad (28)$$

where  $m_0$  is the original mass of the accumulator including the working fluid, before it is pressurized, and  $\rho_w$  is the density of water. Lastly,  $\eta$  will be determined using Equation 29.

$$\eta = \frac{E_{out}}{E_{in}} \times 100\% \quad (29)$$

In order to determine whether a large number of loading/unloading cycles will have a significantly detrimental effect on the energy storage capacity and efficiency of the bladder,  $E_{v\rho}$ ,  $E_{m\rho}$  and  $\eta$  will be measured several times for each position of the manually adjustable orifice valve.

## 8. System Parameters Projection

Using the estimates for the volumetric energy density obtained for the previously mentioned extensions and the mass density of PU $\alpha$  ( $\rho_{\text{PU}\alpha} \approx 1039 \text{ kg/m}^3$ ), the volume and mass of a bladder capable of storing 195 kJ was approximated. The bladder was predicted to be manufactured from  $0.0043 \text{ m}^3$  to  $0.0076 \text{ m}^3$  of material and to weigh somewhere between 4.50 kg and 7.90 kg, depending on the extension ratio used. By adding these values to the corresponding working fluid projections discussed earlier rough estimates for the system energy density were made. Approximated parameters are shown in Table 5 and should be viewed as estimates since their derivation does not other system components such as the equipment necessary for controlling the flow of working fluid.

Table 5: Estimated system energy density (system defined as elastomer material and portion of hydraulic fluid used for energy storage)

	System Volume (liters)	System Mass (kg)	System Volumetric Energy Density (MJ/m <sup>3</sup> )	System Gravimetric Energy Density (kJ/kg)
Upper Bound	10.3	9.57	<b>18.93</b>	<b>20.38</b>
Lower Bound	16.6	16.27	<b>11.27</b>	<b>11.99</b>

## 9. Conclusions

Hydraulic regenerative braking has already seen successful implementation in large vehicles. The Ford Motor Company and the Eaton Corporation introduced the hydraulic launch assist (HLA) in 2002; designed to help accelerate large trucks, it increased fuel efficiency by 25-35%. In order to make HRB practical for smaller sized standard passenger vehicles, hydraulic accumulators need to see significant reductions in size and weight.

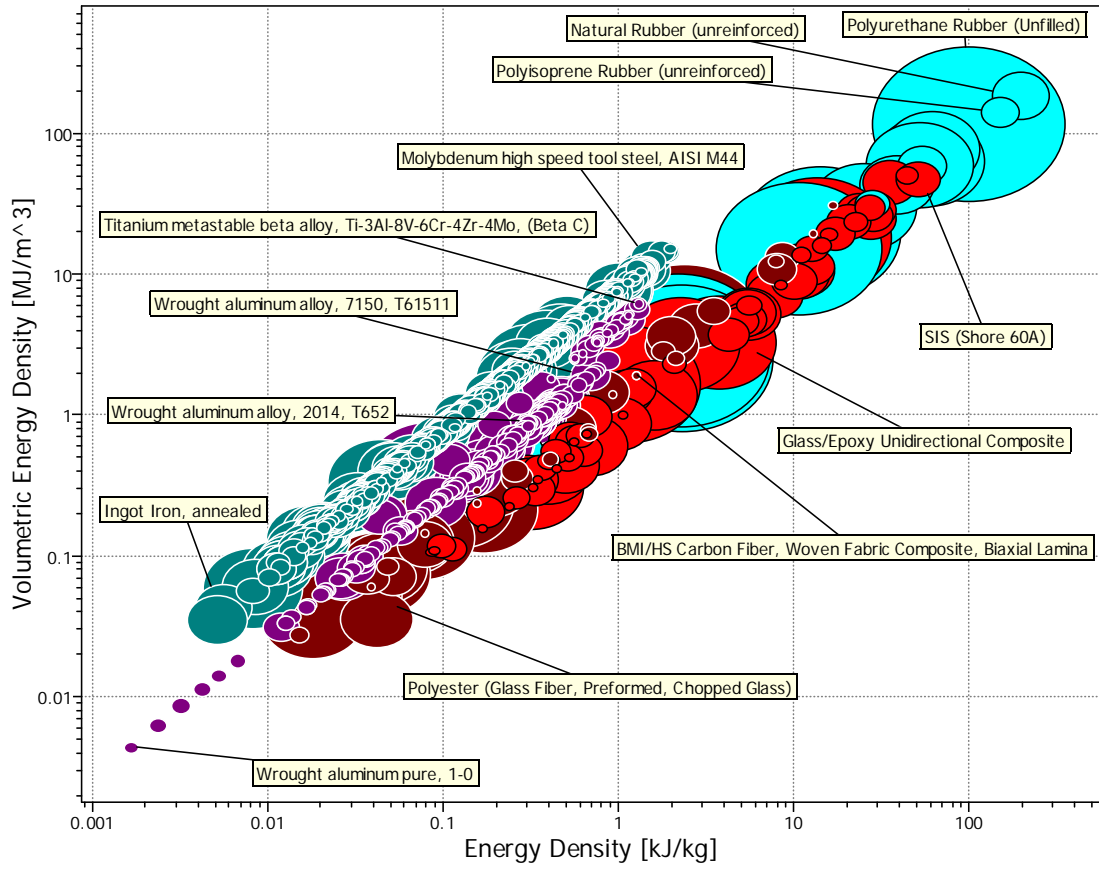
Preliminary calculations have shown that a hydraulic accumulator manufactured from polyurethane should allow for these reductions due to the material's high values for volumetric ( $u \approx 20\text{MJ/m}^3 - 300\text{MJ/m}^3$ ) and gravimetric ( $e \approx 11 - 300 \text{ kJ/kg}$ ) energy densities. Additionally, the design of the elastomeric accumulator allows for a pressure-volume expansion behavior that economizes the amount of hydraulic fluid used to store the energy. The material properties and the shape of the accumulator result in high system volumetric and gravimetric energy densities. Furthermore, since this type of

accumulator will use strain energy as the primary storage mechanism, it will not be susceptible to inefficiency due to heat losses seen in gas pre-charged accumulators (without elastomeric foam).

Currently, an  $\alpha$ -prototype of an accumulator composed of Andur RT curable polyurethane is being manufactured for testing. Empirical data gathered from these tests will be used to validate the initial calculations and will aid in anticipating future complications in the design and testing of the full scale prototype.

# APPENDIX A

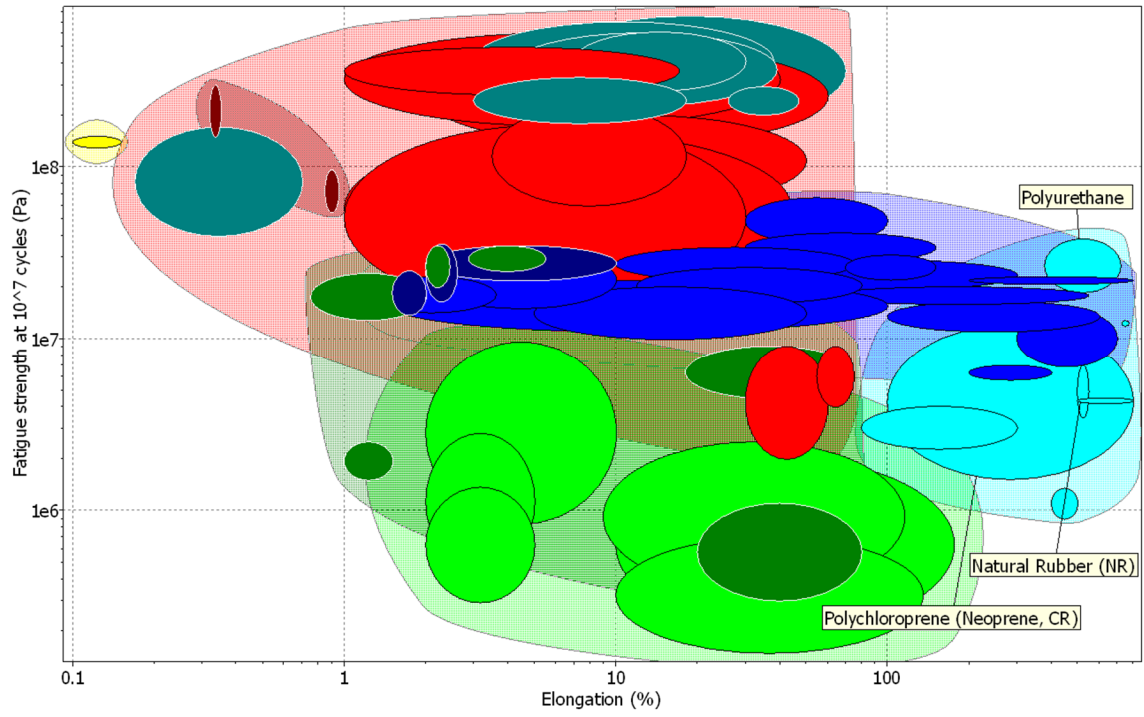
## Materials' Strain Energy Density Chart





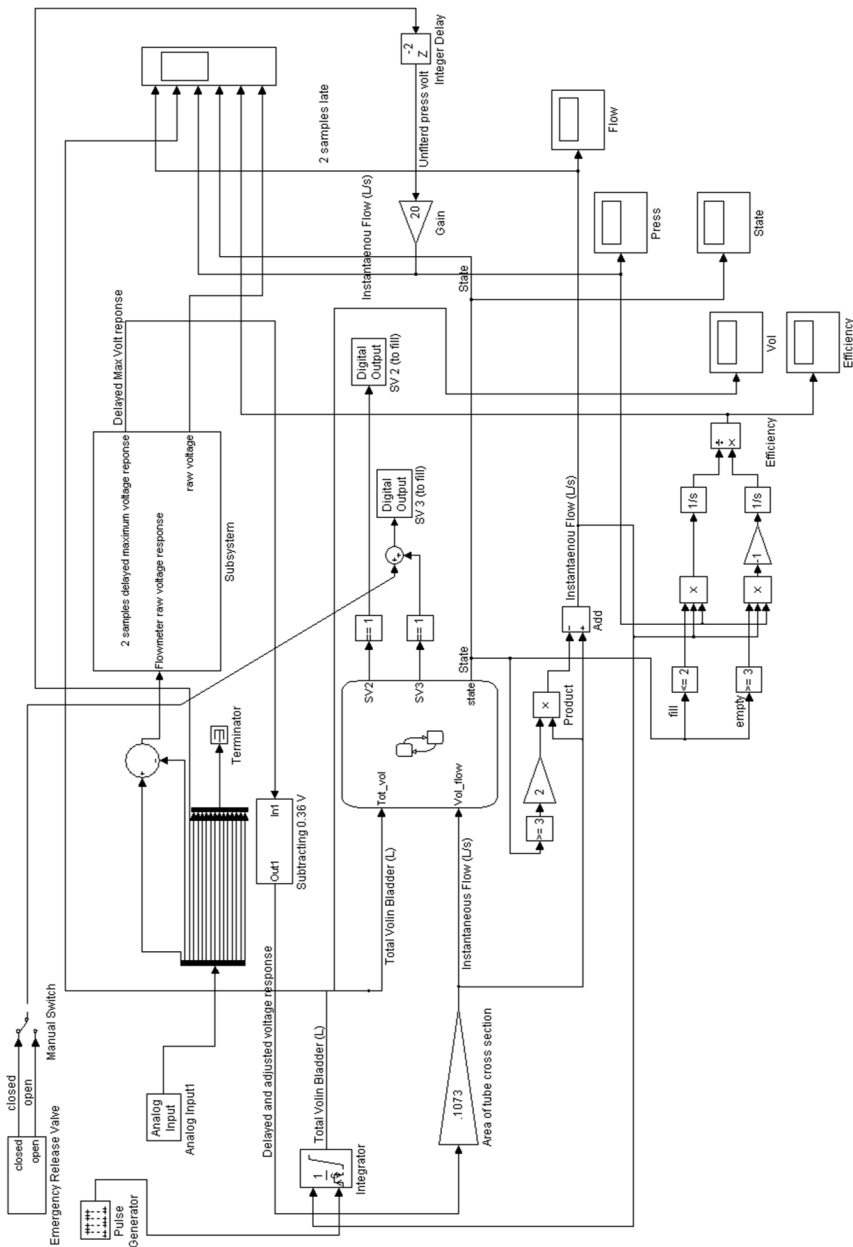
APPENDIX B

Materials' Elongation vs. Fatigue Life Chart



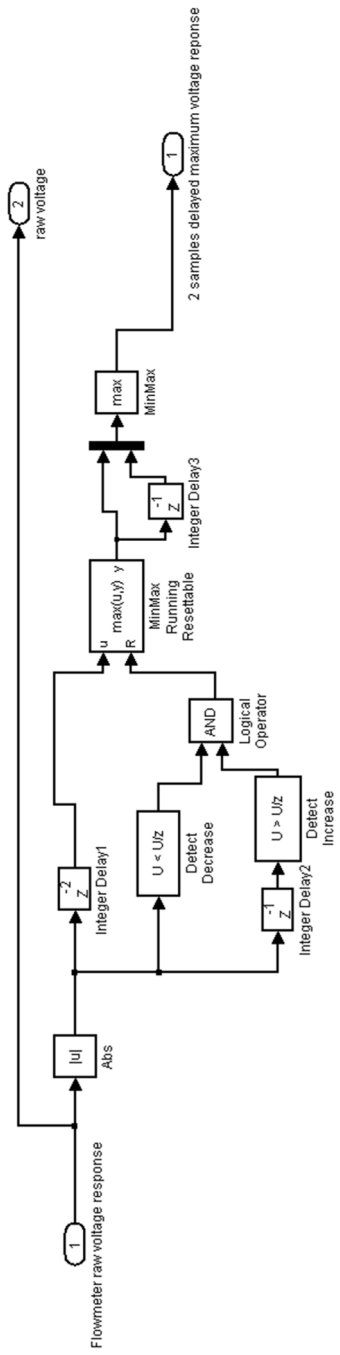
APPENDIX C

Simulink Diagram: Low Pressure Test Setup Operation



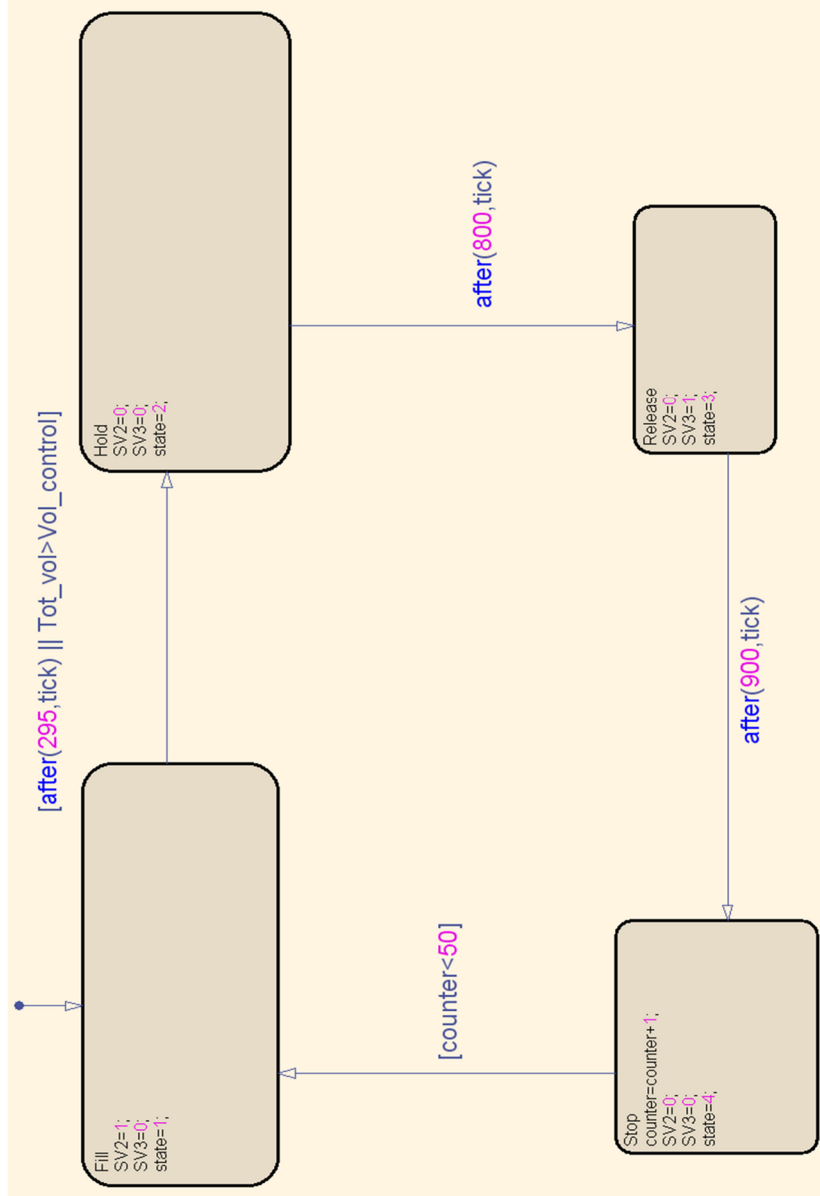
# APPENDIX D

## Simulink Diagram: Subsystem of Low Pressure Test Setup Operation



APPENDIX E

Simulink Diagram: Stateflow Chart of Low Pressure Test Setup Operation



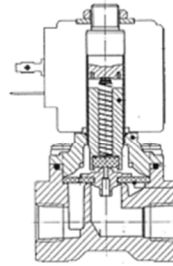
APPENDIX F

Granzow Solenoid Valve Datasheet

**GRANZOW**®  
INC.

Series 21EN  
SOLENOID VALVE

**Model #**  
**21EN2K0V105**  
2-way, internally piloted, normally  
closed solenoid valve



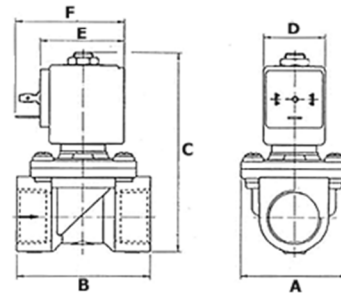
<b>1/4"</b> Pipe Size (Inch)	<b>7/16"</b> Orifice Size (Inch)	<b>1.50</b> Flow Factor (CV)	<b>8</b> Watt Rating (W)	<b>2</b> Min. Pressure (PSI)	<b>300/150</b> Max. Pressure (AC/DC)
<b>FKM</b> Sealing Material	<b>14°- 280° F</b> Temperature Range	<b>Air, Inert gas, Water, Synthetic oils</b> Medium Examples			

Materials of Construction	
Body:	<b>Brass</b>
Armature Tube:	<b>Stainless Steel 300</b>
Fixed Core:	<b>Stainless Steel 400</b>
Plunger:	<b>Stainless Steel 400</b>
Spring:	<b>Stainless Steel 300</b>
Shading Ring:	<b>Copper</b>
Orifice:	<b>Brass</b>

Valve Dimensions	
Valve Width(A):	<b>1 9/16"</b>
Valve Length(B):	<b>2"</b>
Valve Height(C):	<b>3 9/16"</b>
Coil Width(D):	<b>1 3/16"</b>
Coil Length(E):	<b>1 21/32"</b>
Coil Length(F):	<b>2 1/8"</b>

Electrical Connection	
Rating:	<b>NEMA 4</b>
Strain Relief Connector:	<b>Model 009</b>
1/2" Conduit Connector:	<b>Model 010</b>
6 ft. Power Cord:	<b>Model GRN100</b>
Inrush VA:	<b>25</b>
Holding VA:	<b>14.0</b>

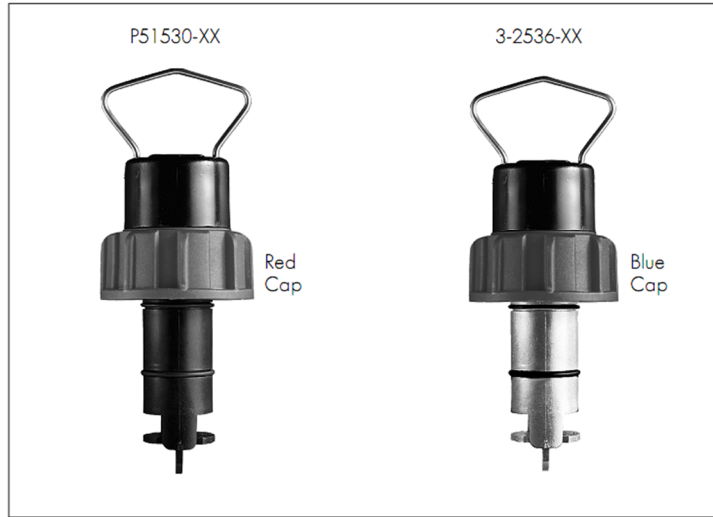
Spare Parts	
Kit:	<b>KTGEN2K0V10</b>



## APPENDIX G

### GF Signet Flowmeter Datasheet

#### +GF+ SIGNET 515/2536 Rotor-X Flow Sensors



#### Features

- PVDF or Polypropylene molded sensor body
- Simple insertion design
- Separate versions for remote and integral installations
- Wide Turndown Ratio of 66:1 for 2536, 20:1 for 515
- Use with comprehensive line of fittings from DN15 to DN1000 (0.5 to 36 in.)
- Process Ready Signal (3-2536-XX)
- Extended length for wet-tap installations available

#### Application

- Pure Water Production
- Filtration Systems
- Chemical Production
- Liquid Delivery Systems
- Pump Protection
- Scrubbers

#### Options

Rotor-X Sensors	Instrument Options									
	8500-1	8500-2	8500-3	8500-4P	5090	9075	5100	5500	5600	9010
515	●	●	●	●	●	●	●	●	●	●
8510	●	●	●	●	●	●	●	●	●	●
2536	●	●	●	●	●	●	●	●	●	●
8512	●	●	●	●	●	●	●	●	●	●

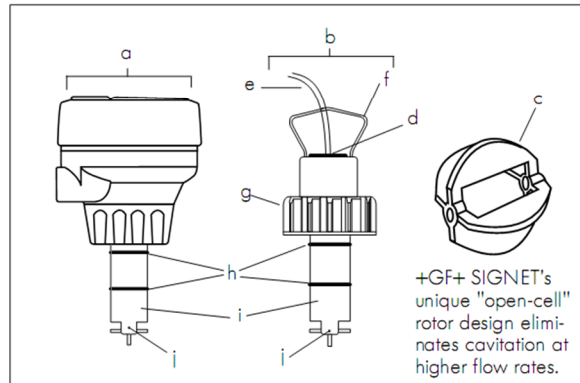
#### Description

Simple and reliable, Rotor-X paddlewheel flow sensors deliver time-honored performance. These highly repeatable, rugged sensors offer exceptional value with little or no maintenance required. Installation is simple with +GF+ SIGNET's comprehensive line of fittings for all pipe materi-

als in sizes from DN15 to DN1000 (0.5 to 36 in.). Output signal of the 515 is a sinusoidal frequency capable of driving a self-powered flowmeter (3-5090). The 3-2536 has a process-ready open-collector signal and can operate to flows as low as 0.1 m/s (0.3 ft/s).

#### Technical Features

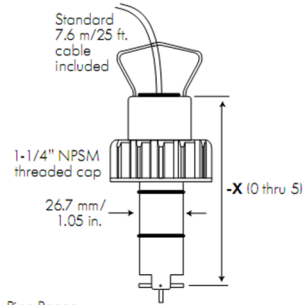
- Integral mount sensor (8510/8512) shown with field-mount transmitter (sold separately)
- Remote mount sensor (515/2536)
- Open cell rotor and rotor pins available in variety of material options (sleeved rotor available for abrasive solutions)
- 1/2 in. NPT conduit connection
- 7.6m/25 ft. cable standard, extendable up to 60m/200 ft. (515) or 305m/1,000 ft. (2536)
- Large bail for sensor removal
- Glass-filled PP ring nut with provision for lead seal installation
- Dual O-ring seal (FPM standard, EPR and Kalrez® available)
- One-piece injection molded (black glass-filled PP or natural PVDF) sensor body
- Rotor pin



+GF+ SIGNET's unique "open-cell" rotor design eliminates cavitation at higher flow rates.

## Dimensions

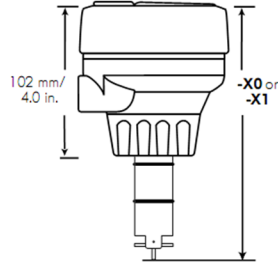
### 515/2536 Sensor



Pipe Range:

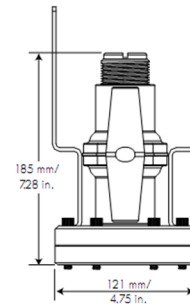
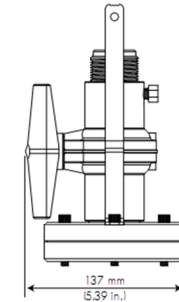
1/2 to 4 in.	-X0 = 104 mm/4.1 in.	} Wet-tap Lengths
5 to 8 in.	-X1 = 137 mm/5.4 in.	
10" and up	-X2 = 213 mm/8.4 in.	
1/2 to 4 in.	-X3 = 297 mm/11.7 in.	
5 to 8 in.	-X4 = 333 mm/13.1 in.	
10" and up	-X5 = 409 mm/16.1 in.	

### 8512 Integral Sensor with Transmitter (sold separately)








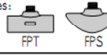




-X0 = 152 mm/6.0 in.
-X1 = 185 mm/7.3 in.

### 3519 Wet Tap Assembly (see catalog page for details)



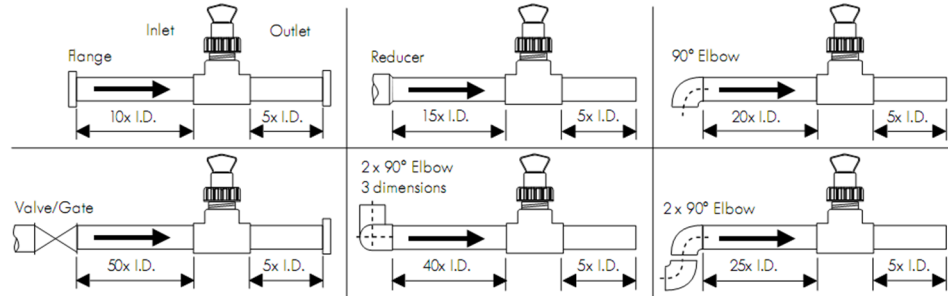
## Fitting Types

Refer to Fittings section of +GF+ SIGNET catalog for a complete listing of part numbers

Type	Description	Type	Description
Plastic tees 	<ul style="list-style-type: none"> <li>• 0.5 to 4 inch versions</li> <li>• PVC or CPVC</li> </ul>	Iron, Carbon Steel, 316 SS Threaded tees 	<ul style="list-style-type: none"> <li>• 0.5 to 2 in. versions</li> <li>• Mounts on threaded pipe ends</li> </ul>
PVC Glue-on Saddles 	<ul style="list-style-type: none"> <li>• Available in 10 and 12 inch sizes only</li> <li>• Cut 2-1/2 inch hole in pipe</li> <li>• Weld in place using solvent cement</li> </ul>	Carbon steel & stainless steel Weld-on Weldolets 	<ul style="list-style-type: none"> <li>• 2 to 4 inch, cut 1-7/16 inch hole in pipe</li> <li>• Over 4 inch, cut 2-1/4 inch hole in pipe</li> </ul>
PVC Saddles 	<ul style="list-style-type: none"> <li>• 2 to 4 inch, cut 1-7/16 inch hole in pipe</li> <li>• 6 to 8 inch, cut 2-1/4 inch hole in pipe</li> </ul>	Fiberglass tees & saddles: FPT FPS 	<ul style="list-style-type: none"> <li>• 1.5 in. to 8 in. PVDF insert</li> <li>• &gt; 8 in. PVC insert</li> <li>• Special order 12 in. to 36 in.</li> </ul>
PP Clamp-on Saddles 	<ul style="list-style-type: none"> <li>• Available in 10 and 12 inch sizes only</li> <li>• Cut 2-1/4 inch hole in pipe</li> </ul>	Metric Wafer Fitting 	<ul style="list-style-type: none"> <li>• For pipes DN 65 to 200 mm</li> <li>• PP or PVDF</li> </ul>
Iron Strap-on saddles 	<ul style="list-style-type: none"> <li>• 2 to 4 inch, cut 1-7/16 inch hole in pipe</li> <li>• Over 4 inch, cut 2-1/4 inch hole in pipe</li> <li>• Special order 12 in. to 36 in.</li> </ul>	Metric Union Fitting 	<ul style="list-style-type: none"> <li>• For pipes from DN 15 to 50 mm</li> <li>• PP or PVDF</li> </ul>

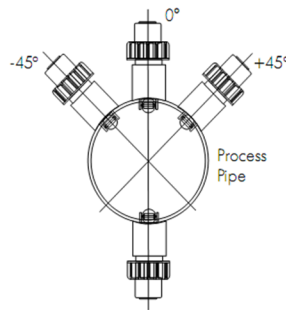
## Installation

- Six common installation configurations are shown here as guidelines to help you select the best location in your piping system for a paddlewheel flow sensor.
- Always maximize distance between sensors and pump sources.



## Sensor Mounting Position

- Horizontal pipe runs: Mount sensor in a vertical position for best performance, or at a maximum 45° angle to avoid air bubbles (pipe must be full). Do not mount the sensor on the bottom of the pipe if sedimentation is likely.
- Vertical pipe runs: Mount sensor in any orientation. Upward flow is preferred to ensure full pipe.



## Maximum Operating Pressure/Temperature

### 515 Sensor:

Glass-filled Polypropylene Body:

12.5 bar (180 psil) max. @ 20°C (68°F)

1.7 bar (25 psil) max. @ 90°C (194°F)

PVDF Body:

14 bar (200 psil) max. @ 20°C (68°F)

1.7 bar (25 psil) max. @ 100°C (212°F)

### 2536 Sensor:

Polypropylene Body:

12.5 bar (180 psil) max. @ 20°C (68°F)

1.7 bar (25 psil) max. @ 85°C (185°F)

PVDF Body:

14 bar (200 psil) max. @ 20°C (68°F)

1.7 bar (25 psil) max. @ 85°C (185°F)

### 3519 Wet-Tap:

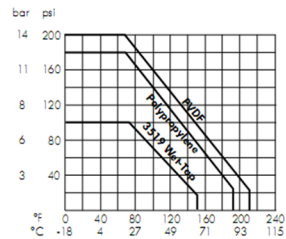
7 bar (100psil) max. @ -18° to 20°C (0° to 68°F)

1.4 bar (20 psil) max. @ 66°C (150°F)

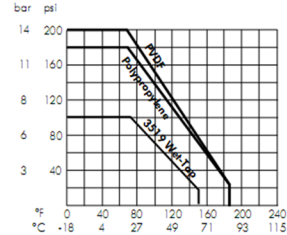
Note: Wet-tap max. installation/removal pressure:

1.7 bar (25 psil) @ 22°C (72°F).

515 Sensor



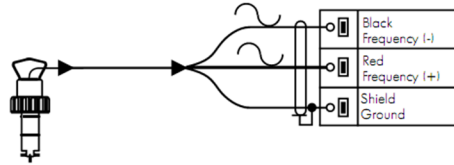
2536 Sensor



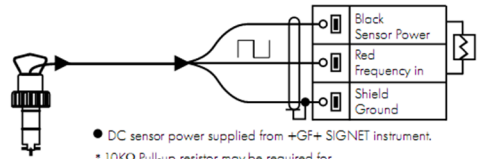


## Wiring

### 515 Sensor Connection to +GF+ SIGNET Instruments



### 2536 Sensor Connection to +GF+ SIGNET Instruments



## Technical Data

### General (for both 515 & 2536)

Pipe Size Range: 15 to 1000 mm (0.5 to 36 in.)  
 Linearity:  $\pm 1\%$  of full range  
 Repeatability:  $\pm 0.5\%$  of full range  
 Minimum Reynolds Number Required: 4500  
 Wetted Materials:

Sensor Body: Glass-filled Polypropylene (black) or PVDF (natural)  
 O-rings: FPM-Viton<sup>®</sup> (std) or EPDM or FPM-Kalrez<sup>®</sup>  
 Pin: Titanium or Hastelloy-C or PVDF; other material options available  
 Rotor: Black PVDF or Natural PVDF; optional Tefzel with or w/o Fluoroloy B<sup>®</sup> sleeve

Cable Type: 2-conductor twisted pair with shield (22 AWG)  
 Shipping Weight:

-X0	0.454 kg	1 lb.
-X1	0.476 kg	1.04 lbs.
-X2	0.680 kg	1.50 lbs.
-X3	0.794 kg	1.75 lbs.
-X4	0.850 kg	1.87 lbs.
-X5	1 kg	2.20 lbs.
3519	1.3 kg	2.86 lbs.

### Standards and Approvals (for both 515 & 2536):

- Manufactured under ISO 9001 and ISO 14001
- CE

### General (515 Only)

Flow Rate Range: 0.3 to 6 m/s (1 to 20 ft./s)  
 Pipe Size Range: DN15 to DN1000 (0.5 to 36 in.)  
 Cable Length: 76 m (25 ft.) standard/60 m (200 ft.) maximum  
 Signal:  
 Frequency: 19.7 Hz per m/s nominal (6 Hz per ft/s)  
 Amplitude: 3.3 V p/p per m/s nominal (1 V p/p per ft/s)  
 Source Impedance: 8  $\Omega$

### Standards and Approvals (515 only):

- FM Class I, II, III/Div./groups A-G

### General (2536 Only)

Flow Rate Range: 0.1 to 6 m/s (0.3 to 20 ft./s)  
 Pipe Size Range: DN15 to DN1000 (0.5 to 36 in.)  
 Cable Length: 76 m (25 ft.) standard/305 m (1,000 ft.) maximum  
 Signal:  
 Frequency: 49 Hz per m/s nominal (15 Hz per ft/s nominal)  
 Supply voltage: 3.5 to 24 VDC regulated  
 Supply current: <1.5 mA @ 3.3 to 6 VDC  
 <20 mA @ 6 to 24 VDC  
 Output Type: Open collector transistor, sinking  
 Output Current: 10 mA max.

## Ordering Information

### 515/8510-XX (Sinusoidal)

Mfr. Part No.	Code	Pipe Sizes	Body	Rotor/Pin
<b>Remote</b>				
P51530-H0	198 801 659	0.5 to 4 in.	Polypro	Blk PVDF/Hastelloy-C
P51530-P0	198 801 620	0.5 to 4 in.	Polypro	Blk PVDF/Titanium
P51530-P1	198 801 621	5 to 8 in.	Polypro	Blk PVDF/Titanium
P51530-P2	198 801 622	10 to 36 in.	Polypro	Blk PVDF/Titanium
<b>Remote Wet-Tap</b>				
P51530-P3	198 840 310	0.5 to 4 in.	Polypro	Blk PVDF/Titanium
P51530-P4	198 840 311	5 to 8 in.	Polypro	Blk PVDF/Titanium
P51530-P5	198 840 312	10 to 36 in.	Polypro	Blk PVDF/Titanium
<b>Remote</b>				
P51530-S0	198 801 661	0.5 to 4 in.	Polypro	Blk PVDF/Natural PVDF
P51530-T0	198 801 663	0.5 to 4 in.	Natural PVDF	Natural PVDF
P51530-T1	198 801 664	5 to 8 in.	Natural PVDF	Natural PVDF
P51530-V0	198 801 623	0.5 to 4 in.	Natural PVDF	Nat. PVDF/Hastelloy-C
P51530-V1	198 801 624	5 to 8 in.	Natural PVDF	Nat. PVDF/Hastelloy-C
P51530-V2	198 801 625	10 to 36 in.	Natural PVDF	Nat. PVDF/Hastelloy-C
<b>Integral</b>				
3-8510-P0	198 864 504	0.5 to 4 in.	Polypro	Blk PVDF/Titanium
3-8510-P1	198 864 505	5 to 8 in.	Polypro	Blk PVDF/Titanium
3-8510-T0	159 000 622	0.5 to 4 in.	Natural PVDF	Natural PVDF
3-8510-V0	198 864 506	0.5 to 4 in.	Natural PVDF	Nat. PVDF/Hastelloy-C

### 2536/8512-XX (Open-Collector)

<b>Remote</b>				
3-2536-P0	198 840 143	0.5 to 4 in.	Polypro	Blk PVDF/Titanium
3-2536-P1	198 840 144	5 to 8 in.	Polypro	Blk PVDF/Titanium
3-2536-P2	198 840 145	10 to 36 in.	Polypro	Blk PVDF/Titanium
3-2536-T0	198 840 149	0.5 to 4 in.	Natural PVDF	Natural PVDF
3-2536-V0	198 840 146	0.5 to 4 in.	Natural PVDF	Nat. PVDF/Hastelloy-C
3-2536-V1	198 840 147	5 to 8 in.	Natural PVDF	Nat. PVDF/Hastelloy-C
<b>Remote Wet-Tap</b>				
3-2536-P3	159 000 758	0.5 to 4 in.	Polypro	Blk PVDF/Titanium
3-2536-P4	159 000 759	5 to 8 in.	Polypro	Blk PVDF/Titanium
3-2536-P5	159 000 760	10 to 36 in.	Polypro	Blk PVDF/Titanium
<b>Integral</b>				
3-8512-P0	198 864 513	0.5 to 4 in.	Polypro	Blk PVDF/Titanium
3-8512-P1	198 864 514	5 to 8 in.	Polypro	Blk PVDF/Titanium
3-8512-T0	198 864 518	0.5 to 4 in.	Natural PVDF	Natural PVDF
3-8512-V0	198 864 516	0.5 to 4 in.	Natural PVDF	Nat. PVDF/Hastelloy-C

### Wet-Tap Sensor and Valve Assembly (Fitting Separate)

<b>Remote Wet-Tap</b>				
3519/515-P3	159 000 819	0.5 to 4 in.	Polypro	Blk PVDF/Titanium
3519/515-P4	159 000 820	5 to 8 in.	Polypro	Blk PVDF/Titanium
3519/515-P5	159 000 821	10 to 36 in.	Polypro	Blk PVDF/Titanium
3519/2536-P3	159 000 822	0.5 to 4 in.	Polypro	Blk PVDF/Titanium
3519/2536-P4	159 000 823	5 to 8 in.	Polypro	Blk PVDF/Titanium
3519/2536-P5	159 000 824	10 to 36 in.	Polypro	Blk PVDF/Titanium

## Accessories

Mfr. Part No.	Code	Description
<b>Rotors 515/8510-XX</b>		
M1538-2	198 801 181	Rotor, PVDF Black
P51547-3	159 000 474	Rotor, PVDF Natural
M1538-4	198 820 018	Rotor, Tefzel®
P51550-3	198 820 043	Rotor and Pin, PVDF Natural
3-0515.322-1	198 820 059	Sleeved Rotor, PVDF Black
3-0515.322-2	198 820 060	Sleeved Rotor, PVDF Natural
3-0515.322-3	198 820 017	Sleeved Rotor, Tefzel®

## Accessories (continued)

Mfr. Part No.	Code	Description
<b>Rotors 2536/8512-XX</b>		
3-2536.320-1	198 820 052	Rotor, PVDF Black
3-2536.320-2	159 000 272	Rotor, PVDF Natural
3-2536.320-3	159 000 273	Rotor, Tefzel®
3-2536.321	198 820 054	Rotor and Pin, PVDF Natural
3-2536.322-1	198 820 056	Sleeved Rotor, PVDF Black
3-2536.322-2	198 820 057	Sleeved Rotor, PVDF Natural
3-2536.322-3	198 820 058	Sleeved Rotor, Tefzel®
<b>Rotor Pins</b>		
M1546-1	198 801 182	Pin, Titanium
M1546-2	198 801 183	Pin, Hastelloy-C
M1546-3	198 820 014	Pin, Tantalum
M1546-4	198 820 015	Pin, Stainless Steel
P51545	198 820 016	Pin, Ceramic
<b>O-Rings</b>		
1220-0021	198 801 186	O-Ring, FPM-Viton®
1224-0021	198 820 006	O-Ring, EPDM
1228-0021	198 820 007	O-Ring, FPM-Kalrez®
<b>Miscellaneous</b>		
P31536	198 840 201	Sensor Plug, Polypro
P31536-1	198 840 202	Sensor Plug, PVDF Metric
P31536-2	159 000 649	Sensor Plug, PVDF
P31542	198 801 630	Sensor Cap, Red (for use w/515)
P31542-3	159 000 464	Sensor Cap, Blue (for use w/2536)
P31934	159 000 466	Conduit Cap
P51589	159 000 476	Conduit Adapter Kit
5523-0222	159 000 392	Cable (per foot), 2 cond. w/shield, 22 AWG
3-8051	159 000 187	Transmitter Integral Adapter

## Engineering Specifications for both 515 and 2536 Flow Sensors

- The flow sensor shall use a four-blade, open-cell rotor design using insertion paddlewheel technology.
- Linearity of the output signal with respect to flow rate shall be  $\pm 1\%$  of full range.
- Measurement repeatability of the output signal with respect to flow rate shall be  $\pm 0.5\%$  of full range.
- The sensor body shall be made of injection-molded polypropylene (PP) that shall accommodate up to 12.5 bar @ 20°C (180 psi @ 68°F) and 1.7 bar @ 90°C (25 psi @ 194°F). As an alternative, the sensor shall be made of injection-molded polyvinylidene fluoride (PVDF) that shall accommodate up to 14 bar @ 20°C (200 psi @ 68°F) and 1.7 bar @ 100°C (25 psi @ 212°F).
- The sensor shall attach to a pipe via a variety of insertion-style installation fittings supplied by the flow sensor manufacturer. Attachment shall use a 1-1/4 X 11-1/2 NPSM threaded cap. Sealing shall be accomplished with a double O-ring seal. O-rings shall be made of FPM-Viton®, FPM-Kalrez® or EPDM.
- The sensor shall be equipped with 0.5 in. female conduit connection.

## Engineering Specifications for +GF+ SIGNET 515 Rotor-X Flow Sensor

- The sensor shall require no electrical power.
- The sensor shall provide an output signal of 3.3 V p-p per m/s nominal (1 V p-p per ft/s) at a frequency of 19.7 Hz per m/s nominal (6 Hz per ft/s) from 0.3 to 6 m/s (1 to 20 ft/s).
- Output shall be via a twisted pair, foil-shielded cable with drain wire. Supplied cable shall be at least 7.6 m (25 ft) long, with a maximum allowable length of 60 m (200 ft).
- The operating range of the sensor shall accommodate nominal flow rates from 0.3 to 6 m/s (1 to 20 ft/s).
- The sensor shall meet appropriate CE standards and FM standards for Classes 1, 11 and 111, Division I/Groups A-G.

## Engineering Specifications for +GF+ SIGNET 2536 Low Flow Sensor

- The sensor shall operate with a power input of 3.3 to 6VDC @ <1.5 mA or from 6 to 24 VDC @ <20 mA.
- The sensor output shall provide an open-collector pulse at a frequency of 49.2 Hz per m/s nominal (15 Hz per ft/s).
- Output shall be via a twisted pair, foil-shielded cable with drain wire. Supplied cable shall be at least 7.6 m (25 ft) long, with a maximum allowable length of 305 m (1000 ft).
- The operating range of the sensor shall accommodate nominal flow rates from 0.1 to 6 m/s (0.3 to 20 ft/s).
- The sensor shall meet appropriate CE standards.

Viton®, Tefzel® and Kalrez® are registered trademarks of DuPont Dow Elastomers.

www.gfsignet.com

13

## APPENDIX H

# Noshok Pressure Transducer Datasheet

Pressure

## Voltage Output Pressure Transducers



### FEATURES

- Accuracy up to  $\pm 0.25\%$  Full Scale (Best Fit Straight Line)
- Welded stainless steel pressure chamber
- Advanced diffused semi-conductor and sputtered thin film sensor for maximum stability
- Compact size
- High alternating load resistance
- High overpressure protection
- CE compliant to suppress RFI, EMI and ESD
- Compatible with NOSHOK Smart System Indicators

### APPLICATIONS

- Hydraulic and pneumatic systems
- Injection molding machines
- Railroad engine controls
- HVAC systems
- Stamping and forming presses
- Refrigeration controls
- Industrial machinery and machine tools
- Pumps and compressors

## SERIES 200

### HIGH PERFORMANCE VOLTAGE OUTPUT PRESSURE TRANSDUCERS

NOSHOK 200 Series Voltage Output Pressure Transducers are designed to provide a previously unequalled level of performance, utilizing diffused semiconductor and sputtered thin film strain gage technology. 200 Series transducers are highly repeatable, shock resistant and are extremely stable over long periods of time. CE compliance which includes substantial levels of RFI, EMI and ESD noise protection combined with reverse polarity and over-voltage protection hardens the product so it performs well in the most demanding applications.

Advanced manufacturing techniques combined with technologically advanced standard features allow NOSHOK to offer a level of performance previously found only on transducers costing hundreds of dollars more. Final calibration tests performed on all NOSHOK transmitters prior to shipment ensures 100% "out of the box" reliability

### SPECIFICATIONS

<b>Output signals</b>	0 Vdc to 5 Vdc, 3-wire; 0 Vdc to 10 Vdc, 3-wire; 1 Vdc to 5 Vdc, 3-wire; 1 Vdc to 6 Vdc, 3-wire; 1 Vdc to 11 Vdc, 3-wire;
<b>Pressure ranges</b>	Standard gauge ranges from vacuum to 15000 psi; Standard absolute ranges from 15 psia to 300 psia
<b>Proof Pressure</b>	3 times Full Scale for ranges 0 psi to 5 psi through 0 psi to 200 psi 1.75 times Full Scale for ranges 0 psi to 300 psi through 0 psi to 10000 psi 1.5 times Full Scale for 0 psi to 15000 psi range
<b>Burst Pressure</b>	3.8 times Full Scale for ranges 0 psi to 5 psi through 0 psi to 200 psi 4 times Full Scale for ranges 0 psi to 300 psi through 0 psi to 10000 psi 3 times Full Scale for 0 psi to 15000 psi range
<b>Accuracy</b>	$\pm 0.5\%$ Full Scale (Best Fit Straight Line); $\pm 0.25\%$ optional (Includes the combined effects of linearity, hysteresis and repeatability)
<b>Repeatability</b>	$\leq \pm 0.05\%$ Full Scale
<b>Hysteresis</b>	$\leq \pm 0.1\%$ Full Scale
<b>Stability</b>	$\leq \pm 0.2\%$ Full Scale per year, non-accumulating
<b>Response time</b>	$\leq 1$ ms (between 10% and 90% Full Scale)
<b>Power supply</b>	10 Vdc to 30 Vdc, 14 Vdc to 30 Vdc for 1 Vdc to 11 Vdc and 0 Vdc to 10 Vdc unregulated
<b>Load limitations</b>	$\geq 5000$ for 0 Vdc to 5 Vdc, 1 Vdc to 5 Vdc, and 1 Vdc to 6 Vdc outputs; $\geq 10000$ for 0 Vdc to 10 Vdc and 1 Vdc to 11 Vdc outputs. Current consumption 8 mA
<b>Wetted materials</b>	316 stainless steel for vacuum through 300 psi; 17-4PH stainless steel sensing diaphragm and 316 stainless steel pressure connection for higher ranges
<b>Housing material</b>	316 stainless steel
<b>Adjustment</b>	$\pm 10\%$ Full Scale for zero and span
<b>Pressure cycle limit</b>	150 Hz
<b>Durability</b>	$> 100,000,000$ Full Scale cycles
<b>Temperature ranges</b>	Compensated 32 °F to 176 °F (0 °C to 80 °C) Effect $\pm 0.017\%$ Full Scale/°F for zero and span Ambient -40 °F to 185 °F (-40 °C to 85 °C) Media -22 °F to 212 °F (-30 °C to 100 °C) Storage -40 °F to 212 °F (-40 °C to 100 °C)
<b>Environmental rating</b>	IP65, NEMA 4X according to EN 60529/IEC 529
<b>Electromagnetic rating</b>	CE compliant to EMC norm EN61326: 1997/A1: 1998 RFI, EMI and ESD protection
<b>Electrical protection</b>	Reverse polarity, over-voltage and short circuit protection
<b>Shock</b>	1000 g's per IEC 770
<b>Vibration</b>	30 g's per IEC 770
<b>Weight</b>	Approximately 3.5 oz.

ORDERING INFORMATION																									
<b>SERIES 200</b>																									
<b>PRESSURE RANGES</b>	-30 inHg to 0 psig <b>30V</b>	-30 inHg to 300 psig <b>30/15</b>	0 psig to 5 psig <b>30/30</b>	0 psig to 10 psig <b>30/60</b>	0 psig to 15 psig <b>30/100</b>	0 psig to 30 psig <b>30/150</b>	0 psig to 60 psig <b>30/200</b>	0 psig to 100 psig <b>300</b>	0 psig to 150 psig <b>1500</b>	0 psig to 2000 psig <b>2000</b>	0 psig to 3000 psig <b>3000</b>	0 psig to 5000 psig <b>5000</b>	0 psig to 6000 psig <b>6000</b>	0 psig to 7500 psig <b>7500</b>	0 psig to 10000 psig <b>10000</b>	0 psig to 15000 psig <b>15000</b>	0 psia to 15 psia <b>15A</b>	0 psia to 30 psia <b>30A</b>	0 psia to 60 psia <b>60A</b>	0 psia to 100 psia <b>100A</b>	0 psia to 150 psia <b>150A</b>	0 psia to 200 psia <b>200A</b>	0 psia to 300 psia <b>300A</b>		
	psig = Gauge Pressure		psia = Absolute Pressure		Other ranges available on special request																				
<b>ACCURACY</b>	1 ±0.5 % Full Scale (Best Fit Straight Line)										2 ±0.25 % Full Scale (Best Fit Straight Line)														
<b>OUTPUT SIGNALS</b>	2 0 Vdc to 5 Vdc, 3-wire			3 1 Vdc to 5 Vdc, 3-wire			4 1 Vdc to 6 Vdc, 3-wire			5 0 Vdc to 10 Vdc, 3-wire			6 1 Vdc to 11 Vdc, 3-wire												
<b>PROCESS CONNECTIONS</b>	1 1/8" NPT male		2 1/4" NPT male		3 7/16" -20 UNF #4 SAE J-514 male				4 1/8" NPT female				9 7/16" -20 UNF #4 SAE J-514 female				10 1/4" BSP male								
<b>ELECTRICAL CONNECTIONS</b>	1 36" cable (connected to option 7)			2 4-pin bendix			3 6-pin bendix			36 Integral cable 36"				6 1/2" NPT conduit (with 36" cable)				7 Mini-Hirschmann (DIN EN 175301-803 Form C)				25 M12 x 1 4-pin			
<b>OPTIONS</b>	ORF Threaded Orifice																								

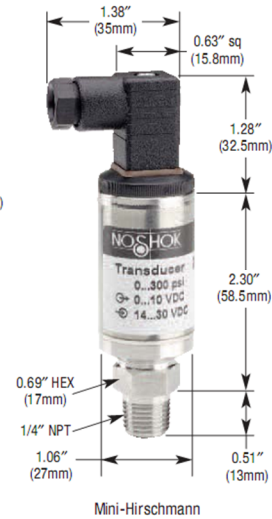
Please consult your local NOSHOK Distributor or NOSHOK, Inc. for availability and delivery information.

EXAMPLE

Series .....200  
 Pressure Range .....0 psig to 500 psig  
 Accuracy .....±0.50 % Full Scale  
 Output Signal .....0 Vdc to 5 Vdc  
 Process Connection .....1/4" NPT Male  
 Electrical Connection .....Mini-Hirschmann  
 Option .....Orifice

200 - 500 - 1 - 2 - 2 - 7 - ORF

Outline Dimensions



WIRING

Wire	Bendix 4-pin or 6-pin	Mini-Hirschmann	Cable	M12 x 1
+ Supply	pin A	pin 1	Red	pin 1
Common	pin B	pin 2	Black	pin 3
+ Output	pin C	pin 3	White	pin 4

\*Note: mate supplied separately or customer supplied

APPENDIX I

**Andur RT 9002 AP Curable Polyurethane Datasheet**

**Andur RT 9002 AP**

**DESCRIPTION**

Andur RT 9002 AP is a low viscosity liquid prepolymer which can be processed and cured at room temperature with Curene 107 to yield an elastomer with a hardness of 88 to 92 Shore A. This system has a extended potlife of about 25 minutes that can be adjusted using oleic acid catalyst.

Andur RT 9002 AP is recommended where room temperature processing and curing is desired with minimal elastomer shrinkage.

COMPONENT PROPERTIES	Andur RT 9002 AP (Prepolymer)	Curene 107 (Curative)
% NCO	5.9-6.3	n.a.
Viscosity @25°C, cps	2470	690
Specific Gravity @ 20°C	1.02	1.21

Storage stability is excellent for both components in the absence of moisture at ambient temperature.

**ELASTOMER PROPERTIES**

Hardness, Shore A.....	88-92
Tensile, psi .....	2100
Modulus, 100% psi.....	790
Modulus, 300% psi.....	1200
Elongation, % .....	600
Die C Tear, pli.....	240
Split Tear, pli .....	105
Bashore Rebound, %.....	48

**PROCESSING CHARACTERISTICS FOR ANDUR RT 9002 AP**

Processing Temperature, °F: .....	50 to 140
Mixing Ratio: .....	100:14.8 (wt ratio) 100:12.2 (vol. ratio)
Pot Life @ Room Temp., minutes.....	25*
Elastomer Demold Time @ Room Temp., hours.....	6**

\* Pot Life can be decreased by adding the oleic acid catalyst (see below)

\*\* Demold time can be shortened considerably by adding oleic acid catalyst or casting into preheated molds. However, curing at higher temperatures will increase the elastomer shrinkage.

### Oleic Acid Catalyst:

The recommended volume of oleic acid catalyst required per 100 gm of system (Andur RT 9002 AP + Curene 107) to achieve an 8 minute pot life as a function of the Andur RT 9002 AP temperature is given in the table below:

Andur RT 9002 AP Temperature	Oleic acid/100 gm System
50 F	2.8 cc
55 F	2.6 cc
60 F	2.4 cc
65 F	2.1 cc
70 F	1.9 cc
75 F	1.7 cc
80 F	1.5 cc
85 F	1.3 cc
90 F	1.1 cc
95 F	0.9 cc
100 F	0.7 cc

For best results, one should store the Andur RT 9002 AP and Curene 107 in the same area as the material is applied so that the processing and curing temperature are the same. The oleic acid concentration can be adjusted to increase or decrease the potlife as desired.

#### **PACKING AND SHIPPING INFORMATION**

<b>Andur 9002 AP:</b>	<u>Containers</u>	<u>Net LBS.</u>
	5-gallon Pail	42
	55-gallon Drum	460

DOT Description: Toxic Liquid, Organic, N.O.S. (Isocyanate)

<b>Curene 107:</b>	<u>Containers</u>	<u>Net LBS.</u>
	1-gallon Can	9
	5-gallon Pail	50
	55-gallon Drum	500

DOT Description: Not regulated

<b>Oleic Acid:</b>	<u>Containers</u>	<u>Net LBS.</u>
	1-gallon Can	8
	5-gallon Pail	42

DOT Description: Not regulated

DOT Description: Not regulated

**SAFETY AND HANDLING PRECAUTIONS**

Andur RT 9002 AP contains free isocyanate monomer, in particular, toluene diisocyanate (TDI). The following handling precautions should be taken.

HARMFUL IF INHALED. CAUSES BURNS. MAY CAUSE SKIN OR RESPIRATORY REACTION. Do not breathe vapor. Do not get in eyes, on skin, on clothing. Keep container closed. Use with adequate ventilation. Wash thoroughly after handling.

FIRST AID: In case of contact immediately flush eyes or skin with plenty of water for at least 15 minutes while removing contaminated clothing and shoes. Call a physician immediately. If Andur 9002-AP is inhaled, remove the victim to fresh air. If not breathing, give artificial respiration; if breathing is difficult, give oxygen. CALL A PHYSICIAN IMMEDIATELY.

**TEST METHODS**

Hardness .....	ASTM D2240
Tensile, Elongation, Modulus.....	ASTM D412
Die C Tear .....	ASTM D1004
Split Tear .....	ASTM D1938
Bashore Rebound.....	ASTM D2632



APPENDIX J

**Material Data of Tubing Tested but Not Used as  $\alpha$ -prototype**



Type	Weld-Spatter-Resistant Choose-a-Color Polyurethane Tubing
Plastic	Polyurethane
Polyurethane Material	Generic Formulation
Material	Ether-Based Polyurethane
Shape	Single Line
System of Measurement	Inch
Reinforcement	Unreinforced
Opaque	Green
Color	Opaque Green
Maximum Pressure Range, psi	100-250
Low Temperature Range	-99° to -1° F
High Temperature Range	+101° to +200° F
Operating Temperature Range	-40° to +180° F
Performance Characteristics	Abrasion-Resistant and Flame-Resistant/Flame-Retardant
Durometer Range	71A-95A/22D-45D (Firm)
Durometer (Firm)	95A
Durometer	95A (Firm)
For Use With	Water
Fittings Used	Compression and Instant
Specifications Met	Underwriters Laboratories (UL)
UL Specification	UL 94V2



Type	Durable Black Neoprene Rubber Tubing
Material	Neoprene
Shape	Single Line
Outside Dia.	1/2" (.5")
Inside Dia.	1/4" (.25")
Wall Thickness	1/8" (.125")
Available Lengths	10, 25, 50, and 100 feet
Reinforcement	Unreinforced
Color	Opaque Black
Operating Temperature Range	-20° to +212° F
Bend Radius	Not Rated
Durometer	82A (Firm)
Tensile Strength	1,286 psi
For Use With	Air, Diluted Acids, Ethylene Glycol, Water
Sterilize With	Steam (autoclave)
Specifications Met	American Society for Testing and Materials (ASTM)
ASTM Specification	ASTM D2000 2BC, ASTM D2000 810, ASTM D2000 A14, ASTM D2000 C12, ASTM D2000 E034, ASTM E162
Compatible Fittings	Barbed, Compression
Chemical Compatibility Link	<a href="#">5102KAC</a>



Type	Oil-Resistant Black Buna-N Rubber Tubing
Material	Buna-N (Nitrile)
Shape	Single Line
Outside Dia.	7/16" (.4375")
Inside Dia.	1/4" (.25")
Wall Thickness	3/32" (.0937")
Available Lengths	10, 25, and 50 feet
Reinforcement	Unreinforced
Color	Opaque Black
Operating Temperature Range	-20° to +212° F
Bend Radius	Not Rated
Durometer	60A (Soft)
Tensile Strength	1,500 psi
For Use With	Air, Deionized Water, Ethylene Glycol, Oil, Solvents, Water
Sterilize With	Steam (autoclave)
Specifications Met	American Society for Testing and Materials (ASTM)
ASTM Specification	ASTM D2000 BG 615
Compatible Fittings	Barbed, Compression
Chemical Compatibility Link	<a href="#">52395KAC</a>

## APPENDIX K

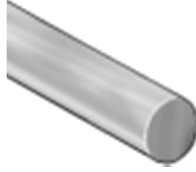
### Material Data of Latex Tubing Used as $\alpha$ -prototype



Type	Super Soft Latex Rubber Tubing
Rubber	Latex
Material	Latex
Shape	Single Line
System of Measurement	Inch
Reinforcement	Unreinforced
Semi-Clear	Amber
Color	Semi-Clear Amber
Maximum Pressure Range, psi	Under 100
Low Temperature Range	0° to +100° F
High Temperature Range	+101° to +200° F
Operating Temperature Range	0° to +158° F
Performance Characteristics	Abrasion-Resistant
Durometer Range	30A-50A (Very Soft)
Durometer (Very Soft)	35A
Durometer	35A (Very Soft)
For Use With	Air and Ethylene Glycol and Water
Fittings Used	Barbed
Specifications Met	Federal Specifications (FED) and Military Specifications (MIL)
MIL Specification	MIL-T-36966/A-A-53848
Federal Specification	FED A-A-52047C

## APPENDIX L

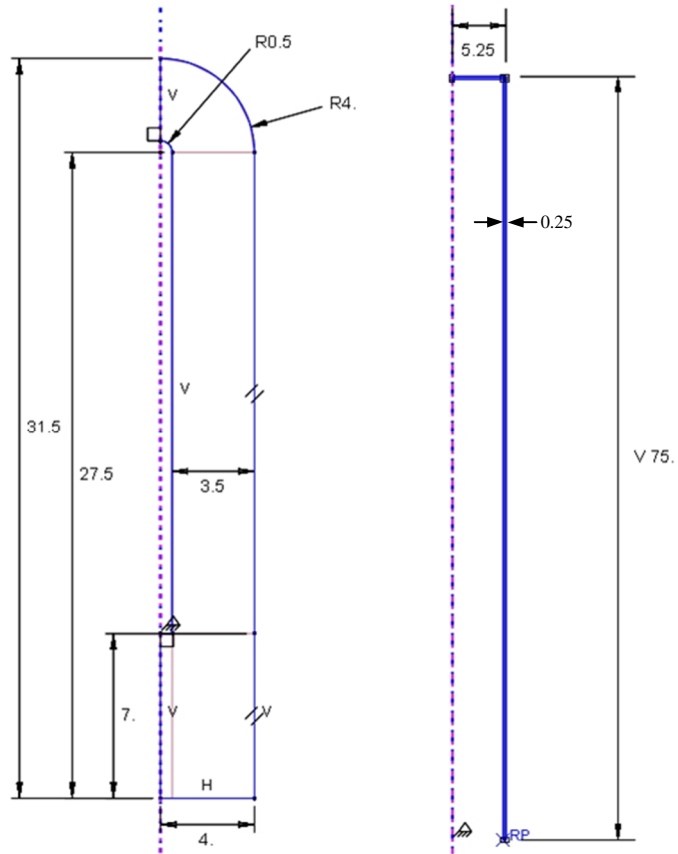
### Material Data of Polyurethane Cord Used for $\beta$ -prototype



Material Type	Polyurethane
Shape	Rods, Cords, and Discs
Backing	No Backing
Length	6"
Length Tolerance	$\pm 1/4$ "
Diameter	1/4"
Diameter Tolerance	+0.020", -0.010"
Durometer	Medium Hard
Durometer Rating	60A
Durometer Hardness Tolerance	$\pm 5$
Temperature Range	-20° to +185° F
Tensile Strength	4000 psi
Color	Amber
Finish	Smooth
Tolerance	Standard
Specifications Met	Not Rated
Properties	Oil Resistant, Abrasion Resistant, Tear Resistant, Impact Resistant, Weather Resistant, Chemical Resistant, Electrical Resistant

APPENDIX M

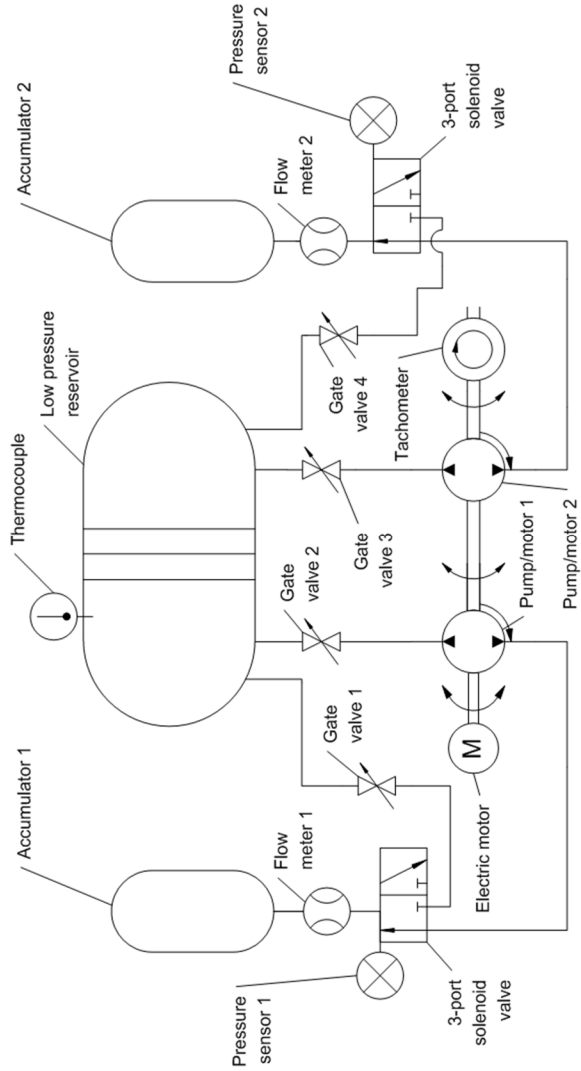
**Bladder (Left) and Shroud (Right) Dimensions in Abaqus Model**



note: all dimensions in inches and drawings are not to scale

# APPENDIX N

## Conceptual Schematic of Bosch-Rexroth Full-scale Experimental Setup



## REFERENCES

- [1] Ibid., Highway Statistics (Washington, DC: Annual issues), table VM-1, available at [www.fhwa.dot.gov/policy/ohpi](http://www.fhwa.dot.gov/policy/ohpi) as of Mar. 23, 2009.
- [2] Riley, Robert Q. Alternative Cars in the 21<sup>st</sup> Century: A New Personal Transportation Paradigm. 2<sup>nd</sup> ed. Pennsylvania: SAE International, 2004, p. 281.
- [3] Hydraulic Launch Assist<sup>TM</sup>: Refuse Truck. Eden Prairie, MN: Eaton Corporation, 2008.
- [4] Krivts, Igor, and German Krejnin, *Pneumatic Actuating Systems for Automatic Equipment: Structure and Design*, Boca Raton: CRC Press, 2006. Print.
- [5] Pourmovahed, A., Baum, S.A., Fronczak, F.J., and Beachley, N.H., 1988. "Experimental Evaluation of Hydraulic Accumulator Efficiency With and Without Elastomeric Foam". *Journal of Propulsion and Power*, 4(2), March-April, p. 188.
- [6] Pourmovahed, A., 1988. "Energy Storage Capacity of Gas-Charged Hydraulic Accumulators". AIAA Thermophysics, Plasmadynamics and Lasers Conference, June 27-29, San Antonio, Texas. pp. 10.
- [7] Roylance, David. "Stress-Strain Curves." Mechanics of Materials Modules. MIT Open Courseware, 1999. Web. 22 Nov. 2010.
- [8] Granta Design Limited. "CES Selector Version 4.8.0." Build 2008. PC.
- [9] Çengel, Yunus, and John Cimbala. *Fluid Mechanics: Fundamentals and Applications*. New York: McGraw-Hill, 2006. Print.
- [10] Dhruva, Vikram (SIMULIA LATAM & Academics). Telephone interview. 30 Jun. 2009.
- [11] Miller, Kurt. "Testing Elastomers for Hyperelastic Material Models in Finite Element Analysis." *Axel Physical Testing Services*. Axel Products, Inc. 2004. Web. 22 Oct. 2009.
- [12] Altidis, Paris and Borg Warner. "Analyzing Hyperelastic Materials w/ Some Practical Considerations." *Impact Engineering Solutions*. Midwest ANSYS Users Group. 18 May 2005. Web/MS PowerPoint presentation. Nov. 2009.
- [13] Datta, Sudhin (Exxon Chemical Company). Telephone interview. 21 Oct. 2010.
- [14] Ashby, M.F., 1992. *Materials Selection in Mechanical Design*, Pergamon, Oxford.



- [15] Dick, John, ed. *Rubber Technology: Compounding and Testing for Performance, 2nd Edition*. Cincinnati: Hanser Publication. 2009. Print.